Single and Dual DC Buses Nanogrids with Decentralized Control

Ahmad Malkawi

A Thesis

In the Department

of

Electrical and Computer Engineering

Presented in Partial Fulfillment of the Requirements

For the Degree of

Doctor of Philosophy (Electrical and Computer Engineering) at

Concordia University

Montréal, Québec, Canada

October 2018

CONCORDIA UNIVERSITY

School of Graduate Studies

This is to certify that the thesis prepared

By: Ahmad Malkawi

Entitled: Single and Dual DC Buses Nanogrids with Decentralized Control

and submitted in partial fulfillment of the requirements for the degree of

Doctor Of Philosophy (Electrical and Computer Engineering)

complies with the regulations of the University and meets the accepted standards with respect to originality and quality.

Signed by the final examining committee:

_____ Chair

Dr. Andrea Schiffauerova

_____ External Examiner

Dr. Mamdou Lamine Doumbia

_____ External to Program

Dr. Marius Paraschivoiu

_____ Examiner

Dr. Shahin Hashtrudi Zad

_____ Examiner

Dr. Akshay Kumar Rathore

_____ Thesis Supervisor

Dr. Luiz A.C. Lopes

Approved by _____

Dr. Mustafa Mehmet Ali, Graduate Program Director

December 10, 2018 _____

Dr. Amir Asif, Dean

Gina Cody School of Engineering and Computer Science

ABSTRACT

Single and Dual DC Buses Nanogrids with Decentralized Control

Ahmad Malkawi, Ph.D.

Concordia University, 2018

The existing power system is based on a centralized approach. Large power plants produce AC electricity that is transmitted over long distances for distribution to the consumers. To meet a higher load demand, the entire system has to be upgraded, which is costly and acquiring rights of way can take decades. Another approach, called distributed generation, is the deployment of smaller generation units closer to the users. This can be based on renewable energy sources (RESs) that mitigate the environmental impact of power generation. However, the stochastic nature of RESs can lead to power quality issues in the distribution system. This can be addressed with the addition of energy storage units and controlling the system as a cluster or a microgrid.

This concept can be extended for small buildings and residences, called nanogrids, offering a means for the realization of net-zero energy homes (NZEHs). These can be AC or DC, but the latter looks more promising since most RESs suitable for NZEHs provide a DC output and DC-DC interfaces tend to present a higher efficiency than their DC-AC counterparts. DC nanogrids also favor the integration of electric vehicles (EVs) and are compatible with modern, electronically controlled, appliances. To date, there are no standards concerning the number of buses and voltage levels of DC nanogrids. The control structure of DC micro and nanogrids, can be based on a hierarchical approach where the primary control level relies on locally measured quantities. This allows a decentralized operation of interfaces using the DC bus voltage as a communication means and V vs. I curves, with specific parameters, for coordination of operation, a method known as DC bus signaling (DBS).

There are several aspects of DC nanogrids for NZEHs that deserve further investigation and are addressed in this thesis. These include a means for a smooth transition of the modes of operation of RESs, such as photovoltaic (PV), which employ V vs. I curves with three regions.

This can minimize the DC bus voltage variations as the system adjusts to variations in load demand and power generation due to varying solar irradiances. The use of supercapacitors (SCs) along with batteries in hybrid energy storage systems (HESSs) can mitigate the impact of high and fast current variations on the losses and lifetime of the battery units. However, by controlling the HESS as a single unit, one forfeits the potential contribution of the SC and its high power capabilities to dynamically improve voltage regulation in a DC nanogrid. This can be achieved by controlling the SC and battery independently without sacrificing the support the battery receives from the SC. Finally, although dual DC bus nanogrids have been advocated by industry associations, they are conceived to have power sources and storage units only in the high voltage (HV) bus. The low voltage (LV) bus is fed through a unidirectional converter, making it vulnerable to a fault in a single element. This thesis proposes the deployment of generation and storage in both buses, with a bidirectional interface for optimizing power balance in both buses. The techniques proposed in this thesis are verified by means of simulation or experimental results.

AKNOWLEDGEMENT

First, I would like to thank Allah Almighty for giving me the strength and the ability to conduct and finish this piece of research. My deep thanks go to Him for all the blessings he has given me even for this opportunity to thank Him.

My deep gratitude goes to my professor Luiz Lopes, whom without his guidance, instructions, support, enlightenment, patience, and being there when help is most needed, this research would not be completed. I am highly thankful for my college, Khaled Elamari, for his encouragement during the program journey.

I would like to acknowledge the University of Jordan for their financial support. I would like to acknowledge Yarmouk University and Concordia University for the strong knowledge I gained from them. I would like to acknowledge and thank my biggest source of encouragement, my family back home. My mom, father and mother-in-low, without your continuous prayers, encouragement, and unconditional love, I would not be able to continue my Ph.D. journey. I pray that Allah blesses you with a long and a happy life and pray that he gives me the strength and wealth to return some your favors and compensate you for the years I lived far from you. To my darling wife, who have stood by my side during this journey, who bore the long hours I spent working in the lab far from her, for her tender-love, I am deeply thankful to you, and I ask Allah to give me the strength and time to make it up to you. To my brothers and sister and my family for their support. It is my pleasure to acknowledge my PEER group, thanks for such nice research group.

DEDICATION

To my parents, wife and mother-in-low,

Amenh Alkilany,

Mohammad Malkawi,

Roa'a Malkawi,

Enshrah Alrusan,

Without whom none of my success would be possible

TABLE OF CONTENTS

LIST OF FIGURES

LIST OF TABLE

NOMENCLATURE

RES: **Renewable Energy Source.**

PV: **Photovoltaic.**

HV: **High voltage.**

LV: **Low voltage.**

MPPT: **Maximum power point tracking.**

SoC: **State-of-Charge.**

DER: **Distributed Energy Resources.**

DSM: **Demand Side Mangement.**

DBS: **DC Bus Signaling.**

CV: **Constant Volatge.**

CPS: **Constant Power Source.**

CCM: **Continuous Conduction Mode.**

SAS: **Solar Array Simulator.**

HESS: **Hybrid Energy Storage System.**

SC: **Supercapacitor.**

EMS: **Energy Management Strategy.**

LPF: **Low Pass Filter.**

HPF: **High Pass Filter.**

DAB: **Dual active bridge.**

SPS: **Single-Phase-Shift.**

CHAPTER ONE: INTRODUCTION

1.1 Introduction

The existing electric power system is based on electricity being generated in large power plants and transmitted over long distances to supply the consumer loads. Some of its limitations to meet the increasing energy demands are obtaining the rights-of-way, the high-energy costs to build new large power plants, and the high cost of long distance transmission lines. Deployment of smaller or modular units, ideally based on renewable energy sources (RESs), close to the consumers at the distribution level look like a promising solution. Moreover, this can mitigate the environmental pollution and the shortage of fossil fuel energy. However, the stochastic characteristic of renewables and resulting variable power generation can lead to power quality issues in the distribution system. One way around this is to associate them with energy storage units and controllable loads [1]. On the other hand, with so many new elements in the power system, it will become very complex and difficult to coordinate and control power flow and enforce power quality with conventional electromechanical (on-off) devices. Smart grid technologies, that are based on power electronics converter and sophisticated information and communication technology, can deal with these issues by controlling certain segments of the power system as a cluster [2, 3]. This is essentially the concept of "microgrids" which can be applied to distribution feeders and neighborhoods with "small" power plants, of a few 100's of kW [4]. The microgrids concept should also enable the distributed energy resources (that include power sources, energy storage units and controllable loads) to operate in islanding (stand-alone) mode in the case of a utility power grid failure [3-5]. In the case of a DC microgrid, such as a photovoltaic (PV) powered neighborhood, connected to an AC utility grid, a bi-directional DC-AC converter is required. This grid tie or interface converter can also be used as energy control center [5]. This concept can be extended for smaller systems/clusters, of 10's of kW, such as a residence, what becomes a nanogrid. In fact, the future smart residences/homes are envisioned to be net-zero energy homes. That is, the total amount of energy consumed by them, on an annual basis, is nearly equal to the amount of energy they produced [6]. To be able to operate autonomously, at least for some time, they should present not only generation as well as storage units and controllable loads, which with

a suitable control structure, can be seen as a nanogrid. Nanogrids can be based on AC or DC distribution [5, 7].

In order to connect RESs, plug-in hybrid electric vehicles and storage units to an AC nanogrid, power electronics converters are used. For the PV and wind turbines, unidirectional power electronic converters can be used. In the case of PV, the required DC-AC converter usually consists of two stages: A step-up (boost) DC-DC converter and a single or three-phase DC-AC converter. This provides a "buffer zone" between the energy of the DC source and the AC loads and internal distribution system [5]. Two-stage power electronics converters, but now bidirectional, can be used to connect the storage units to the AC nanogrid grid [8]. In the AC nanogrid, the DC-AC converters of the DERs are responsible for voltage and frequency regulation of the AC bus, in islanding (stand-alone) mode and grid connecting mode [9, 10]. Figure 1. 1 shows an AC nanogrid [5]. For the distributed energy sources, energy storage system and load in the nanogrid, the DC bus is the simplest interconnection bus [5, 11].When compared to the AC distribution, the DC distribution does not require frequency or phase control/synchronization. In addition, this distribution has higher efficiency and higher reliability [5, 11-14]. Furthermore, DC has lower distribution losses, lower cost of conductors for the same power and does not use bulky transformers leading to cost and volume reduction [5, 11, 15]. Besides that, the nanogrid is dynamically decoupled from the grid by a power electronics converter. Thus, the future residential electrical system could very well be based on DC distribution [5].

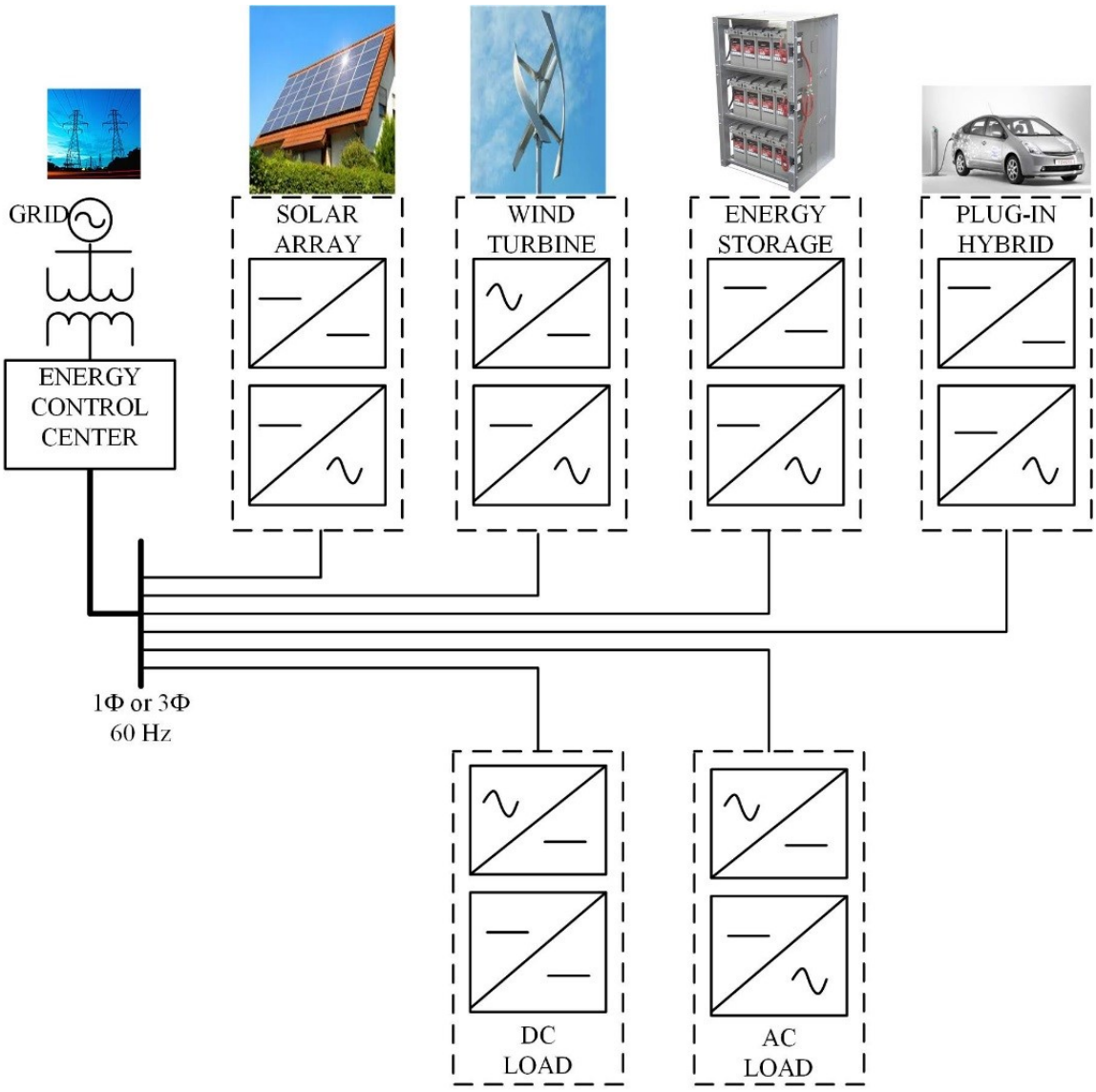

Figure 1. 1 : AC nanogrid

In fact, a DC nanogrid can have fewer power converters than an AC, by eliminating the front-end rectifier and the power factor correction circuit (PFC) present in most contemporary AC appliances. The DC voltage of the nanogrid would be applied directly to the intermediate DC bus of these "electronic loads." Thus, it can provide a higher overall energy efficiency, from local sources to local loads, compared to the AC nanogrids [5]. Moreover, due to the use of power converters of DC voltage transformations into different levels for different applications and due to the development of the power electronics technology the number of DC loads could increase and AC loads could decrease [16-18]. The DC distribution system is already applied in automotive, marine, and manufacturing industrial at the distribution level. Also, DC power systems are

employed in the international space station, spacecraft, aircraft, computers, and servers in data centers [19-24]. Moreover, using power electronics converters that are controllable and can provide current limiting, reduces the need for electromechanical protection devices. Besides, at the failure mode, a serial semiconductor switch opens in a completely breakerless nanogrid [5]. Figure 1. 2 [5] shows a DC nanogrid for a future home consisting of RESs (solar power and wind turbine), plug-in hybrid electric vehicle, storage system, controllable loads (AC loads and DC loads) and utility grid connection through a power electronics converter. As in the AC nanogrid, a DC nanogrid can operate in a stand-alone mode when the utility grid falls into abnormal or fault conditions [5, 7, 25].

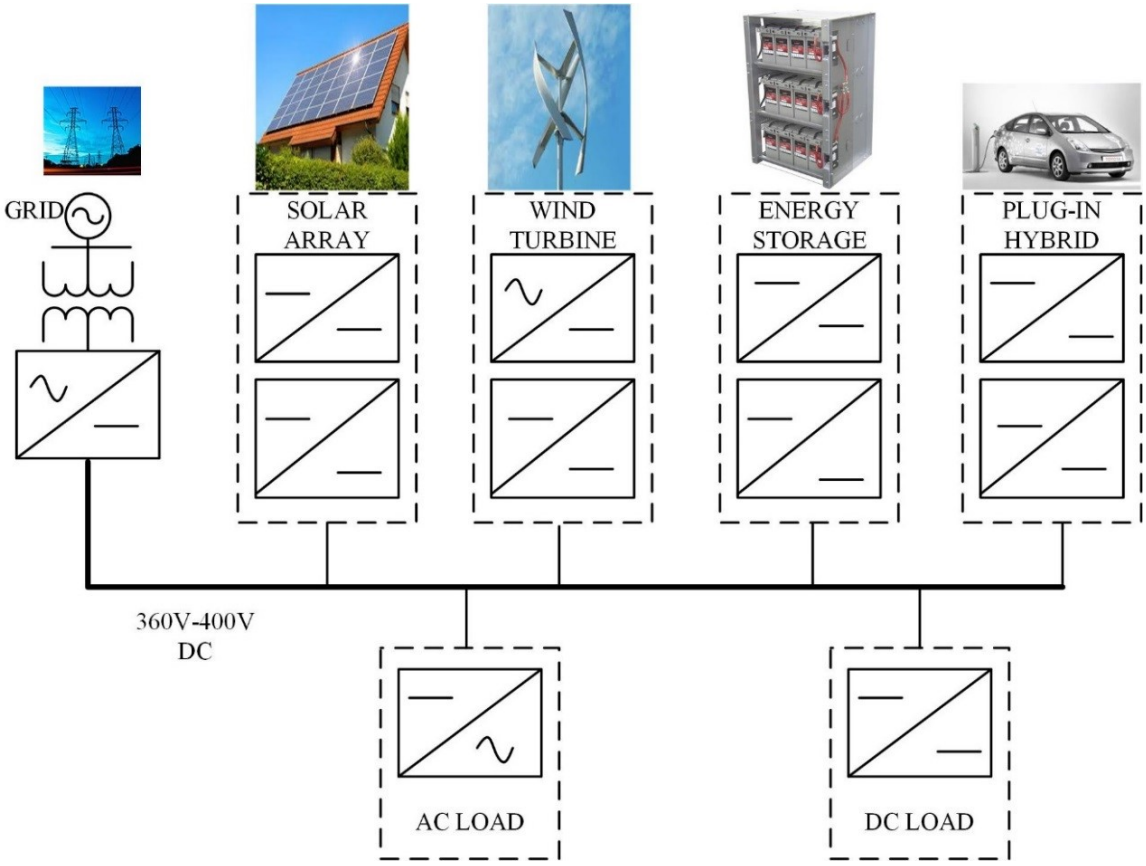

Figure 1. 2: DC nanogrid

The conventional method to control power and current sharing in the nanogrid is to develop a centralized controller which should be aware of each component of the system [26]. This controller has a very high cost communication infrastructure and complex supervisory control

structure. At the end, the central control and the communication link have a high impact on the system reliability [26-28]. In order to control the nanogrid in a de-centralized way with a good degree of autonomy, a hierarchical structure is used [5, 23]. In general, the hierarchical control consists of three levels of control as shown in Figure 1. 3 [23]. The primary level is a local controller for nanogrid resources and controllable loads. It is responsible for controlling the DC bus voltage based on droop control strategy [29, 30]. This control strategy contributes to the power and current sharing by using a virtual feedback impedance or resistor directly to change the output resistance of the converter (1.1). Moreover, the DC bus voltage level carries information about "load/demand level" a higher load level implies a lower DC bus voltage [31]. This control strategy is widely used in the parallel operation of DC-DC, AC-DC and DC-AC converters [32-34]. The droop control is also used to allow multiple sources to operate in parallel [5]. The second level for the hierarchical controller is to ensure that the electrical levels in the system are within the required values. Finally, the tertiary control level is the distribution management system, which controls the power flow in the DC nanogrid, that is to facilitate the economical operation of the system [23, 35]. A distributed control strategy by using DC bus signaling (DBS), which includes droop control, is usually employed to control a nanogrid [36]. In the DC bus signaling concept, each distributed energy resource has a threshold voltage to operate, where the current injected by the power electronics interface is zero. The DC bus signaling is used to minimize the economic cost of the overall system by setting the low cost RESs with the first priority [37]. To avoid the converters from operating at high current with low voltage, a small voltage bandwidth of approximately 5% of the nominal voltage is used [17]. A supervisory controller of the nanogrid can direct power flow and manage energy in the system based on V vs. I curves for each component, which is essentially DC bus signaling [5].

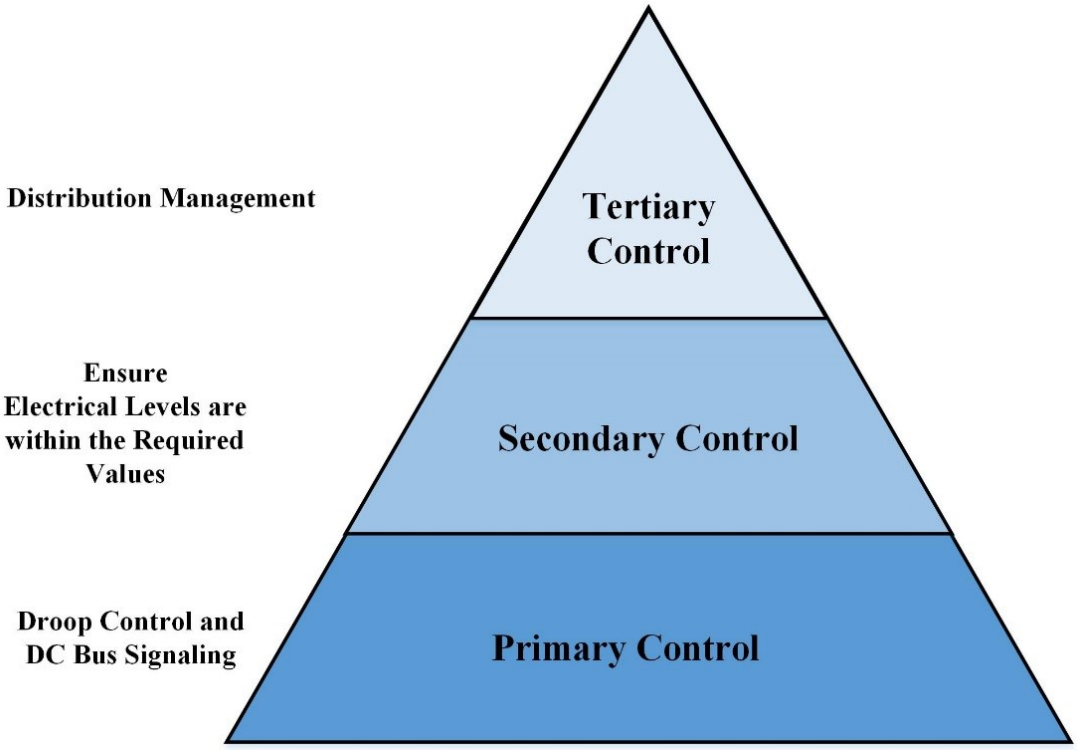

Figure 1. 3: Hierarchical control of three levels.

One of the main segments of the V vs. I curves used in most DERs is the droop curve, which can be described by:

$$V_{DC} = V_{NL} - I_{DC}R_d \tag{1.1}$$

Where;

V_{NL} : is the threshold voltage.

I_{DC} : is the injected current by the power electronics interface.

R_d : is the droop constant and given by:

$$R_d = \frac{\Delta V_{DC}}{\Delta I_{DC}} \tag{1.2}$$

Therefore, the amount of current injected by a DER with droop control will depend on the DC nanogrid voltage (V_{DC}). As the latter decreases, due to a high load level, the DERs will inject more current and power to meet the increased load demand.

The V vs. I curves of RESs, such as solar photovoltaic (PV), usually consist of a droop, a maximum power point tracking (MPPT) and a current limit segment. The primary control logic of

the interface should allow a smooth transition from one segment to another. This is relatively simple to accomplish with 2-stage DC-DC converters with an intermediate energy storage element [1, 19]. The first stage runs a MPPT algorithm while the second controls the power injected into the grid as a function of the DC grid voltage. Conventional search MPPT methods, such as perturb and observe (P&O), can be used since the intermediate energy storage element provides a good degree of decoupling between the continuously varied PV power and the power injected into the DC grid. However, when a single-stage converter is used, the power drawn from the PV panel corresponds to that injected into the DC grid, what should impose constraints on the type of MPPT algorithm to be used. A supervisory control is used for a seamless transition in [38, 39], which needs a communication link between the DERs that is not available in the de-centralized control.

In [20], a scheme for multiple single-stage PV interfaces operating with DBS and presenting smooth switching between constant voltage (CV) mode, not droop, and MPPT is presented. Each unit presents parallel CV and MPPT loops. The impact of DC bus voltage variations on the output signal of the CV loop PI controller is clear, but there is no discussion on the MPPT logic and how it should affect the output signal of the MPPT loop PI controller. Besides, the important current limit mode, and transition, is not discussed. A similar approach is used in [21], where the search-type P&O MPPT method is employed. The performance of the scheme is verified by means of simulation only and it is hard to estimate the speed of response of the system since the waveforms cover a time range of several seconds. The relevance of smooth transitions between droop and MPPT was also discussed in [17], but experimental results were conducted with a constant power source (CPS) emulating the PV interface. The option of running the MPPT logic periodically, say every 1s, and then comparing the magnitudes of the modulating signals from parallel loops is not considered in this discussion since it should lead to a slower dynamic response. This thesis presents a novel control algorithm in which a non-search-type MPPT algorithm and that does not rely on measurements of the solar irradiation is used while allowing a smooth transition between modes of operation.

The second main DERs in micro and nanogrids are the energy storage systems (ESSs). The most commonly used energy storage elements in ESSs are batteries due to high energy densities. On the other hand, in general, batteries present relatively low power densities, making it difficult for them to compensate for large and sudden power unbalances. This condition can lead to

increased power losses and high operating temperatures, which can significantly decreases the lifetime of the battery. Keeping the battery operating as close as possible to the ideal condition respecting the recommended SoC ranges, charging and discharging rates, temperature, cell-charge equalization is very important according to [40, 41]. Hybrid energy storage systems (HESSs), with battery and supercapacitor (SC), have been proposed to strike a balance between the complementary characteristic of these two energy storage means [42, 43]. The SC can compensates transient power fluctuations while the battery supplies the average and slow varying power demand [42-44].

The literature reports several approaches for controlling the power sharing between battery and SC in applications with HESSs. A two level electrical storage system is presented in [45] to deal with the power fluctuation of RESs. The stress on the battery can be mitigated by a control algorithm that extracts the maximum power from the RESs and uses the SC to deal with the high frequency components of the RES' power fluctuation [46]. A model predictive control system for a HESS is proposed in [47] where a model of the battery and SC is used to generate the gating signals of the DC-DC converters (interfaces) with the high frequency power supplied by the SC. A supervisory energy management strategy (EMS) based on neural networks, which is rather complicated, is proposed in [48]. It has been shown in [49] that a dynamic EMS in a RES integrated with a HESS can provide effective active DC link voltage regulation and reduced current stress on the battery [49]. All these algorithms are based on centralized control employing a communication link between the DERs. However, if communication fails, the system is disabled. Thus, centralized control schemes tend to present lower reliability [26-28]. Since battery and SC in a HESS are usually co-located and the main task of the SC is to prevent the fast varying current components from circulating through the battery, a simple scheme with frequency component separation, based on a low pass filter (LPF) or a high pass filter (HPF) is usually employed [50]. The high frequency and fast varying current components to be supplied by the HESS are processed by the high power density SC while the average and slow varying components are dealt with by the battery. One issue with this approach is that it tends to forfeit the potential contribution of the SC and its high power capabilities to dynamically improve power quality in a DC nanogrid.

The DBS and droop control are based on locally measured variables, such as DC bus voltage, and provide an effective means for setting power sharing among parallel units in steady-

state conditions. This is achieved by defining two parameters: The droop ($\Delta V/\Delta I$) slope (factor) and the threshold (no-load) voltage. The first is usually defined based on the power ratings of the DERs and remains constant. The larger units have smaller droop slopes to take larger shares of the power/current required for balancing supply and demand, mitigating DC bus voltage variations (ΔV). The threshold voltage is used for energy management and can be updated by a supervisory controller employing low bandwidth communication, but is not essential for system operation. Disregarding the latter, for high reliability, and assuming that the SC and battery are not co-located, the SC unit should present a droop factor lower than that of the battery's to be able to contribute more to dynamic voltage regulation. However, additional means are required to accommodate its low energy capacity constraint. For that, a HPF with a properly selected cut-off frequency is proposed in this Thesis.

One key aspect that remains unclear is the voltage level that should be adopted. According to the IEC, Extra Low Voltage (ELV) DC presents a magnitude of less than 120 V and lower risk of electrical shock. However, for supplying kW loads, relatively high currents are required, leading to high distribution losses and/or conductors. The 48V DC is a standard telecom voltage level [5, 51, 52]. The following, higher voltage, category is the Low Voltage (LV), with magnitudes between 120 V and 1500V. Higher voltages lead to lower currents, for a given power demand, but this might complicate the design of the DC protection system as well as require the use of power interfaces with large voltage gains. The 380V DC level matches with the industry-standard intermediate DC voltage [5, 53]. One option that has been considered and proposed by industry associations is the use of two voltage levels (buses). The Emerge Alliance [54, 55] advocates the use of a 24 V, mostly to comply with current LED technology for lighting, and a 380 V for other loads. However, in order to be able to supply "other small loads", the use of a 48 V, which is also being considered for mild-hybrid vehicles, will be selected.

It should be noted that in the Emerge Alliance scheme, power sources and storage units are connected to the 380 V bus and a step-down unidirectional DC-DC converter is used to supply the 24 V lighting bus. One issue of concern is the reliability of the 24 V, which will be de-energized if either the 24V bus interface fails or the 380V bus is not operational. The dual DC bus nanogrid considered in this research work presents power sources and energy storage units in both DC buses. A bidirectional "interlink" converter/interface is employed to allow power flow from one bus to

the other, and indirectly, from the 48V bus to the AC utility grid, assuming that a 380V DC to AC grid interface is present and operational.

A simplified Dual DC buses nanogrid is shown in Figure 1. 4. There one can see that the RESs (solar energy) and electrical storage systems (batteries) are connected to both DC buses. The first can employ a unidirectional converter but the second requires a bidirectional one. The utility grid is connected to the HV DC bus via a bidirectional DC-AC converter. A bidirectional inter-link converter allows the power flow between the two DC Buses.

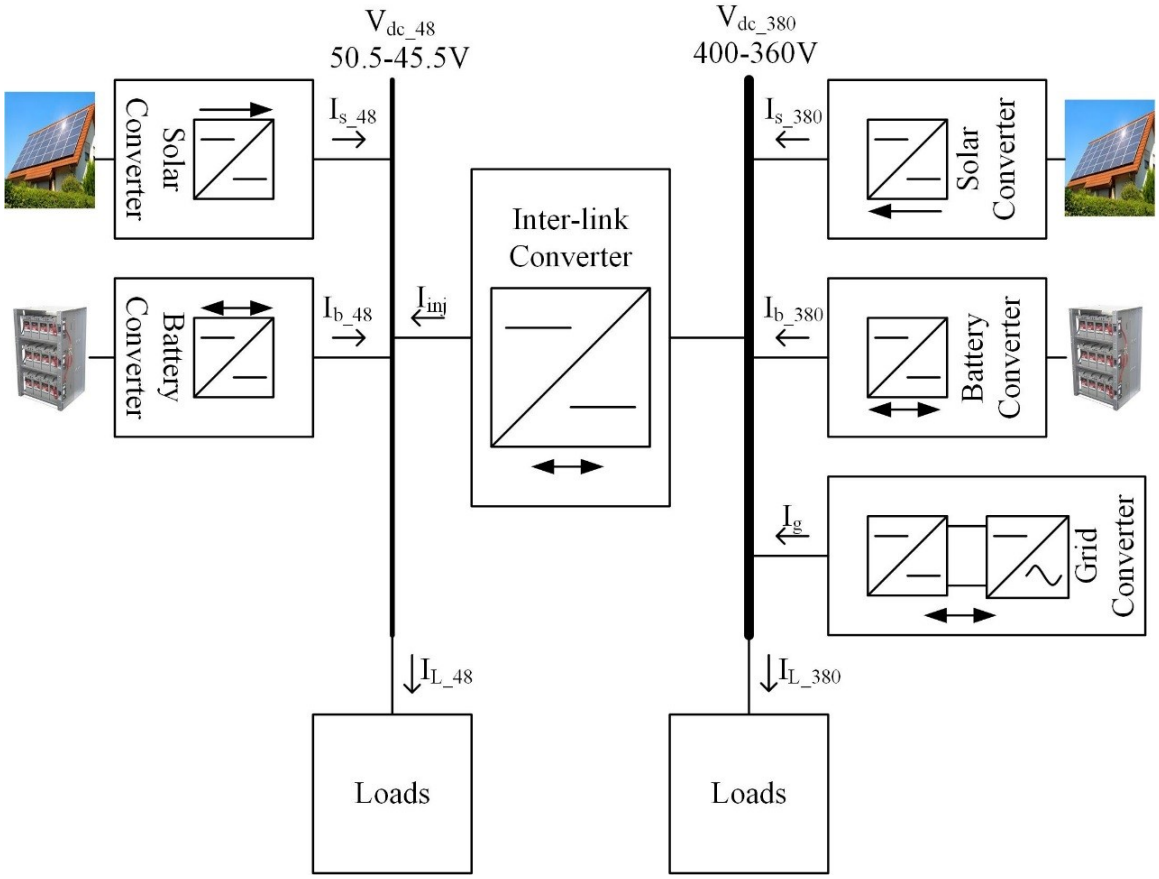

Figure 1. 4 : Dual DC nanogrid.

1.2 Dual DC Buses Nanogrid

In the simplified Dual DC shown in Figure 1. 4. The utility grid is connected to the HV DC bus via a bi-directional DC-AC converter. A bidirectional inter-link converter allows the power flow between the 2 DC Buses. In this configuration, power can also flow from the LV DC bus to the AC utility grid and back, through the interlink DC-DC converter and the DC-AC converter.

In the dual DC buses nanogrid, the DERs of the HV DC bus and LV DC bus could be controlled to optimize the operation of each bus, or of the overall system, based on the nanogrid conditions. That is, on the availability of RESs power, SoC of storage units and load demand in both buses. While the operation of a single DC bus nanogrid has already being considered in the development of the first generation of DC nanogrids, the coordinated operation of a nanogrid with 2 DC buses is still a challenge.

1.2.1 The High Voltage (HV) 380V DC Bus

As a conventional single-bus DC nanogrid, the HV DC bus can be controlled in a de-centralized way with a hierarchical structure based on droop control and DC bus signaling [5, 23, 36]. In such a case, the power electronic interfaces of all DERs present a V vs. I curve that dictates how much power it injects or absorbs according to the voltage of the DC bus. In the case of the HV DC bus, it has a nominal voltage of 380V, but the actual voltage is allowed to vary, typically, between 360V and 400V.

Figure 1. 5 shows the V vs. I curves of the usual components found in a DC nanogrid [5]. The grid DC-AC converter is discussed first. When the DC bus voltage is between 390V and 370V, the converter operates in droop mode with droop constant (slope) R_{dg}. Otherwise, it operates in current limiting mode, with the DC-AC converter absorbing rated current for $V_{DC} > 390$ V and supplying for $V_{DC} < 370$ V. Its threshold, or no-load, voltage is the rated voltage of the DC bus: 380V. That is to say that at this voltage, the current flowing through the converter is zero. The values of the threshold voltage and the DC bus voltage determine the power flow direction. When the DC bus voltages is higher than 380V but lower than 390V, power flows from the DC nanogrid into the AC utility grid ($I_g < 0$A). Conversely, for DC bus voltages is lower than 380V but higher than 370V, power flows to the DC nanogrid from the AC utility grid ($I_g > 0$A). The threshold voltage is the main control parameter of this DC-AC converter, which can be adjusted by the secondary control level.

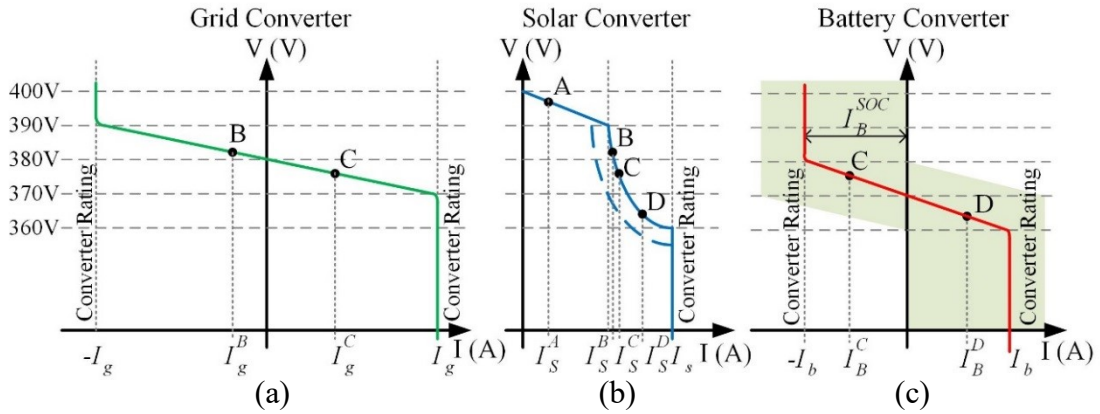

Figure 1. 5 : High voltage DC bus sources V-I curves.

In the case of the RESs, the threshold voltage is 400V, higher than the grid converter threshold voltage. In the concept of DC bus signaling, this gives the RESs, if available and producing power, the highest priority to feed the loads. As illustrated in Figure 1. 5, the solar converter typically operates in three regions: droop, constant power, and constant current. The solar converter operates with droop constant R_{ds} with a DC bus voltage between 400V and 390V, when the converter starts to operates in the maximum power point tracking (MPPT) mode. When the DC bus voltage further drops to 360V, the solar converter operates at the current limiting mode. The dashed line shows that the solar converter is reprogramed to operate in MPPT mode with DC bus voltage higher than 390V based, when the solar irradiance (W/m^2) decreases from the rated value or the PV panel temperature increases [5].

For the electrical storage system, a bidirectional power electronic converter must be used. It operates in the droop mode, with droop constant R_{db} when the DC bus voltage is between 380V and 360V. Otherwise, it operates in the current limiting mode, absorbing rated current for V_{DC} > 380 V and supplying for V_{DC} < 360 V. The storage system usually has the third priority, after the RESs and the utility grid to feed the load. It has a threshold voltage of 370V, lower than the other system interfaces. This prevents the electrical storage system from discharging through the utility grid. On the other hand, the electrical storage system is discharged at DC bus voltages less than 370V. As for the grid interface, the actual value of the threshold voltage of the storage unit can be adjusted, for power and energy management, based on the instantaneous and historical price of energy, that could be drawn from or supplied to the utility grid. Long and/or short-term histories of the local renewable energy generation and the nanogrid load profiles play a role in reprograming the threshold voltage. In addition, the history of the state of charge (SoC) should be taken into

account. To achieve optimal threshold voltage preprogrammed, *optimal energy utilization algorithm* is used [5]. To implement this algorithm, historical data about the system is needed. The maximum current of charging and discharging is based on the battery manufacturer and power converter ratings. In some cases, when the SoC drops below 20%, the control will stop the discharging operation mode. On the other hand, the battery will not be charged when it has a SoC greater than 90% [56]. The current limits could be a function of the state of charge (SoC) [5, 17-19]. This produces the shaded area in the V-I curve in shown in Figure 1. 5.

From Figure 1. 5 and there are many possible operation points, A, B, C and D based on the DC bus voltage. At point A, the DC bus voltage is higher than 390V. The solar converter operates with droop constant R_{ds} while the utility grid converter and the electrical storage system could not manage the surplus power. That could be when the storage system has a SoC and the utility grid is disconnected maybe for fault condition. Then assuming all the three units are enabled at the operation points B, C and D. When the DC bus voltage is between 390V and 380V (point B), the utility grid converter regulates the DC bus voltage by feeding the surplus power to the grid with droop constant R_{dg}. The solar converter operates at MPPT while the electrical storage system is charged with constant current. Both of the utility grid converter and the electrical storage system are responsible for regulating the DC bus voltage with droop constants R_{dg} and R_{db} respectively, when the DC bus voltage between 380V and 370V at point C. The utility grid supplies power with the solar converter and the electrical storage system is charged. When the DC bus voltage is between 370V and 360V (point D), the electrical storage system regulates the DC bus voltage with droop constant R_{db} while the utility grid is supplying power with the solar converter by with a constant current. At point B, C, and D the solar converter operates at MPPT.

When there is no connection between the high voltage DC bus and the low voltage DC bus (there is no inter-link converter) the load current is the summation of the distributed resources currents (1.3).

$$I_{Load} = I_S + I_g + I_b \tag{1.3}$$

1.2.2 The Low Voltage (LV) 48V DC Bus

In order to connect the two DC buses, a suitable control strategy and power management should be employed for the inter-link converter. Two control strategies for the inter-link converter

in a dual DC bus nanogrid, average droop control and constant voltage ratio were presented in [57]. The first determines the power flow between the two buses based on the average value obtained from droop curves of the LV and HV sides. On the other hand, the second employs a PI controller to keep the per-unit voltage ratio constant between the two buses, without a V vs. I curve. Those control strategies can be used for a dual DC bus nanogrid with similar participations of RESs and storage units but it should not be use when the Dual DC nanogrid has a connection with the AC utility grid.

The inter-link converter control strategy can be based on droop control and DC bus signaling. The inter-link converter should be able to supply the surplus power of the 48V DC bus to the 380V DC bus when the 380V DC bus has the ability to absorb this excess power, at high load condition or in the grid-connected mode. On the other hand, the 380V DC bus supplies power to the 48V DC bus, at power shortage condition on the 48V, without discharging the 380V batteries. The inter-link converter will connect the utility grid connected to the 380V DC bus to the 48V DC bus. The droop control V-I curve and DC bus signaling based on the 48V DC bus will prevent the 48V bus batteries from discharging through 380V DC bus with a suitable DC bus signaling arrangement for the resources. In the proposed low voltage DC bus, the 48V nominal voltage has a voltage bandwidth of 0.05*48=2.4≈2.5V. The inter-link converter has the second priority to feed the load and it has a power flow from LV DC bus to HV DC bus has and reverse direction. Therefore, it has a threshold voltage of 48V with a droop bandwidth of 2.5V for a 49.25-46.75V operation band. The RESs converters are unidirectional with a droop operation band of 50.5-49.25V with threshold voltage 50.5V. The electrical storage systems have a bidirectional converter with a droop operation band of 48-45.5V with threshold voltage 46.75V.

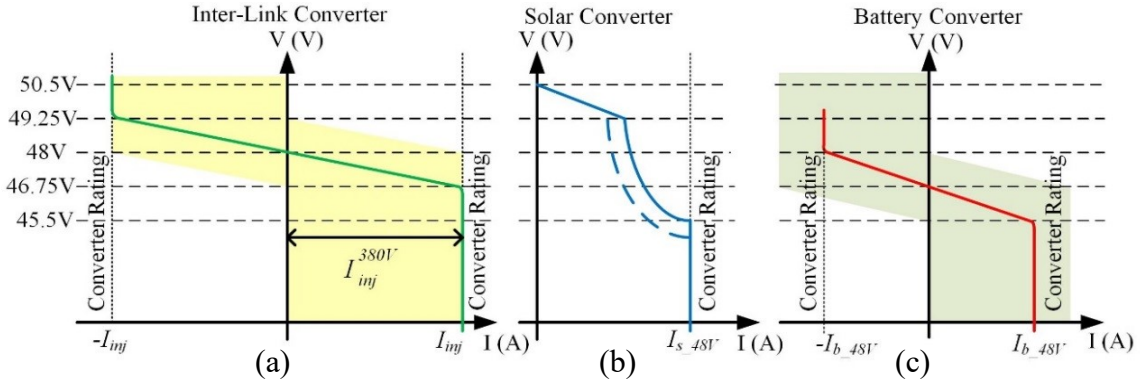

Figure 1. 6: Low voltage 48V DC bus V-I characteristics.

Figure 1. 6 shows the low voltage DC bus V-I characteristics. The voltage parameters of the V-I curve for the 1-stage solar converter are the same as those shown in Figure 1. 6. Regarding the current levels, considering a 2 kW solar panel, the following values have been used: 40.6 A when the DC bus voltage is at 49.25 V, where the maximum power region starts for rated solar irradiance. As a result, in the low power injection mode with a DC bus voltage between 50.5 V and 49.25 V at rated power, the PV converter operates with a droop constant of 0.0308Ω through (1.2) with a maximum current about 40.6 A at 49.25V DC bus voltage. The converter starts to operate in the MPPT region with rated solar irradiance, when the DC grid voltage falls below 49.25 V. In this region, the injected current increases, keeping the injected power constant, as the DC bus voltage decreases, until it reaches 43.96 A or 45.5V, that is the rated converter current. With a DC bus voltage lower than 45.5V, at the rated solar irradiance, the solar converter operates as a current source with 43.96A at current limiting mode.

The battery converter operates with droop control and current limiting in charging or discharging modes. The bidirectional DC-DC converter is a buck-boost (class C DC-DC) converter controlled with the V-I characteristic shown in Figure 1. 6. For power management, the converter operates with a droop constant of 0.0284Ω from (1.2) for a DC bus voltage between 48 V and 45.5 V and a current limit of 43.96 A. When the DC bus voltage is higher than 46.75 V, the converter operates to charge the batteries. The batteries will share the load demand with the PV and the inter-link converter when the DC bus voltage is less than 46.75 V. As the DC bus voltage decreases to 45.5 V, the converter operates as a current source with 43.96 A in the current limiting mode. In this work for simplification, the converter limit does not vary with the batteries SoC.

The inter-link converter manages and controls the power flow between the 48V DC bus and the 380V DC bus in the dual DC bus nanogrid shown in Figure 1. 4. Previously, the 380V DC bus operated in stand-alone or grid connected mode with V-I curves based on droop control and DC signaling as in Figure 1. 5. Based on that, Figure 1. 6 shows the V-I curve of the 48V DC bus to operate in standalone or in inter-link with the 380V DC bus. From the V-I curves shown in Figure 1. 6, the surplus current in the 48V DC bus (when the DC bus voltage is higher than 48V, light load), power will flow to the 380V DC bus as given by a droop characteristic R_{dint}. This surplus power will feed the 380V DC bus loads or will be supplied to the utility grid, based on the 380V DC bus conditions and its V-I curves shown in Figure 1. 5. At high load condition on the

48V DC bus (DC bus voltage less than 48V), the 380V DC bus will share load power with the 48V DC bus with the droop characteristic R_{dint}. This power comes from the 380V DC bus RESs or from the utility grid based on the 380V DC bus conditions and its V-I curves in Figure 1. 5. From the V-I curves in Figure 1. 6, the 48V DC bus batteries will not be discharged into the 380V DC bus. The 48V DC bus is discharged with DC bus voltages less than 46.75V and at this DC bus voltage the power flows from the 380V DC bus to the 48V DC bus, according to the inter-link converter V-I characteristic. To avoid power flow from the 48V DC bus to the 380V DC bus at light load condition, or when the utility grid cannot absorb the excess power, the inter-link converter (current) limits should be reprogrammed. They are changed in this converter based on the HV DC bus voltage, as in Figure 1. 7. In addition, Figure 1. 7 shows that the inter-link converter (current) limits are reprogrammed to prevent the 380V DC bus batteries from discharging into 48V DC bus. By preventing power flow to the 48V DC bus when the 380V DC bus is less than 370V at this voltage the 380V DC bus batteries start to discharge.

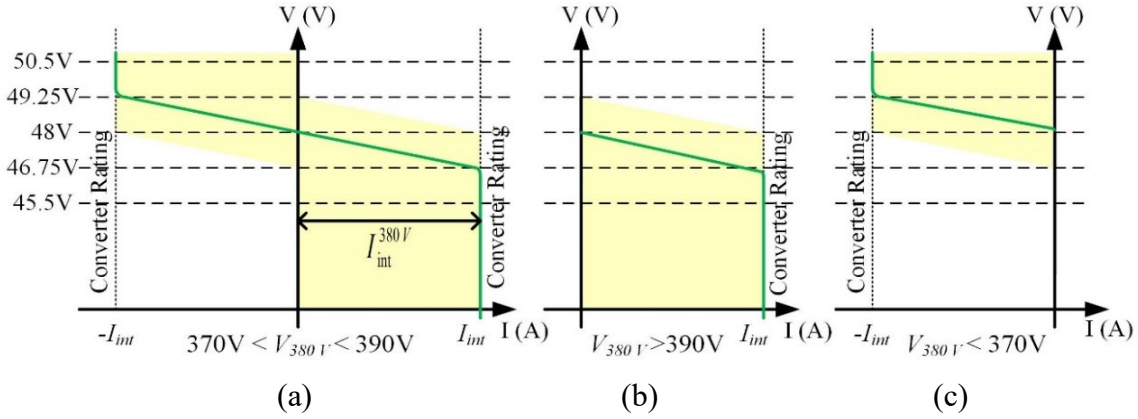

Figure 1. 7 : Inter-link converter current limit reprogramed with 380V DC bus.

1.3 Objective

The main focus of this research work in on DC nanogrids for small buildings and net-zero energy homes (NZEHs). Several aspects need further investigation in order to make the system more performing and economically viable. In this context, the main objectives of this thesis are:

- Develop a new control strategy for RESs operating with DC bus signaling (DBS). RESs usually present a V vs. I curve with three modes of operation, dictated by the availability of renewable energy and DC bus voltage. As these change, the power injected in the DC nanogrid can vary suddenly leading to voltage variations in the DC bus and low power

quality. This issue can be mitigated with a control scheme that provides smooth transitions between modes of operation.

- Maximize the positive impact of supercapacitors in DC nanogrids operating with DBS. Storage energy systems based on batteries are considered the weak link, in terms of cost and life span, in micro and nanogrids. Hybrid energy storage systems (HESSs) with supercapacitors have been used for mitigating this problem. However, the current control strategies for HESSs forfeits the potential of the supercapacitors to also improve the dynamic response of the DC bus voltage. This can be achieved by controlling the supercapacitor independently while still making sure the batteries are not subject to large and fast current variations.
- Control strategy based on DBS for a bi-directional inter-link converter. Most of the dual DC buses nanogrids described in the literature employ sources and storage units only in the high voltage bus and a unidirectional interlink converter. With storage and sources installed in both buses, a bi-directional interlink converter with a suitable DBS based or compatible control strategy is required. It should be simple, allowing the interlink converter to assist with power balancing in both buses without leading to unfavorable operating conditions for the storage units.

1.4 List of Publication

- Ahmad Malkawi and Luiz A. C. Lopes, "Control of the Power Electronics Interface of a PV Sources in a Smart Residential DC Nanogrid", IEEE CCECE in *Power and Energy Circuits and Systems,* pp. 678-681, 2016. **Published**. Conference paper.

- Ahmad Malkawi and Luiz A. C. Lopes, "A Novel Seamless Control Algorithm for a Single-Stage Photovoltaic Interface Employing DC Bus Signaling", International Journal of Electrical Power and Energy Systems. **Under review**. Journal paper.

- Ahmad Malkawi and Luiz A. C. Lopes, "Improved Dynamic Voltage Regulation in a Droop Controlled DC Nanogrid Employing Independently Controlled Battery and Supercapacitor Units", Applied Sciences. 2018 Sep 1;8(9):1525.**Published**. Journal paper.

- Sabah Siad, Ahmad Malkawi, Lilia Galai Dol, Gilney Damm, and Luiz A. C. Lopes, " Nonlinear control of a DC Microgrid for the integration of distributed generation based on different time scales", International Journal of Electrical Power and Energy Systems. **Under review**. Journal paper.

1.5 Thesis Outline

This thesis is based on manuscript thesis where each chapter, after the introduction, is entirely a manuscript published, submitted or under preparation.

Chapter Two discusses the control strategy of RESs in three modes of operation: droop, maximum power, and current limiting. This control strategy presents a seamless transition between the three modes of operation.

Chapter Three presents an improved control strategy for the Supercapacitor interface in the DC nanogrid that improves the DC bus voltage dynamics, while preventing the current in the battery from presenting fast variations and high frequency components.

Chapter Four discusses modeling and control loop design of an inter-link converter based on a dual active bridge (DAB) isolated DC-DC converter with droop control and DC bus signaling.

Chapter Five presents a simulation results for a full dual DC bus nanogrid.

Chapter Six presents the conclusion and future works.

CHAPTER TWO: CONTROL OF THE SOLAR CONVERTER

2.1 Introduction

DC is an interesting alternative to AC distribution in residential and office nanogrids that employ Renewable Energy Sources (RESs) and electrical storage units because most of them present DC characteristics. Besides, many of the modern AC electronic loads are "DC compatible" having an AC-DC converter to create an intermediate DC bus. DC distribution does not require frequency and phase control, as AC distribution, what facilitates the control strategies of distributed energy resources (DERs). In addition, the power electronic interfaces tend to present lower cost and volume while a higher efficiency and reliability [5, 11-14].

The conventional methods to control power and current in a DC nanogrid are based on a centralized controller, which requires information from each component of the system [26]. It employs a communication network and a complex supervisory control structure. If communication fails, the system is disabled, thus resulting in a system with relatively low reliability [26-28]. Alternatively, the nanogrid can be controlled with a hierarchical structure in a de-centralized way, where the DER interfaces operate with a good degree of autonomy [5, 23, 58, 59]. In general, the hierarchical control consists of three levels. The primary controller for DERs and loads capable of demand side management (DSM) is based on locally measured quantities. These define the power injected/absorbed into/from the DC bus based on DC bus signaling (DBS) [29, 30, 58, 59]. In such a case, the magnitude of the DC bus voltage, which carries information about the system's load level, is allowed to vary within a narrow range. Higher load levels and/or low injected power by renewable energy sources (RESs) imply a lower DC bus voltage [31]. In DBS, the power injected/absorbed by each interface depends on its V vs. I (or V vs. P) curve and locally measured quantities. By defining the shapes and values of the V vs. I curves, one can define how each interface will react to varying load and power generation conditions.

The secondary level of the hierarchical control is to ensure that the electrical levels in the system are within the acceptable value. Finally, the tertiary control level manages the power flow in the DC nanogrid, for a more economical operation of the system [23, 35]. The parameters of the V vs. I curve can be modified by the secondary and tertiary control levels using a low bandwidth

communication channel. A distributed control strategy based on DBS is usually used to control a nanogrid [36, 58, 59]. A supervisory control is used for a seamless transition in [38, 39], which needs a communication link between the DERs that is not available in the de-centralized control.

The V vs. I curves of RESs, such as solar photovoltaic (PV), usually consist of a droop, a maximum power point tracking (MPPT) and a current limit segment. The primary control logic of the interface should allow a smooth transition from one segment to another. This is relatively simple to accomplish with 2-stage DC-DC converters with an intermediate energy storage element [1, 19]. The first stage runs a MPPT algorithm while the second controls the power injected into the grid as a function of the DC grid voltage. Conventional search MPPT methods, such as perturb and observe (P&O), can be used since the intermediate energy storage element provides a good degree of decoupling between the continuously varied PV power and the power injected into the DC grid. However, when a single-stage converter is used, the power drawn from the PV panel corresponds to that injected into the DC grid, what should impose constraints on the type of MPPT algorithm to be used.

In [20], a scheme for multiple single-stage PV interfaces operating with DBS and presenting smooth switching between constant voltage (CV) mode, not droop, and MPPT is presented. Each unit presents parallel CV and MPPT loops. The impact of DC bus voltage variations on the output signal of the CV loop PI controller is clear, but there is no discussion on the MPPT logic and how it should affect the output signal of the MPPT loop PI controller. Besides, the important current limit mode, and transition, is not discussed. A similar approach is used in [21], where the search-type P&O MPPT method is employed. The performance of the scheme is verified by means of simulation only and it is hard to estimate the speed of response of the system since the waveforms cover a time range of several seconds. The relevance of smooth transitions between droop and MPPT was also discussed in [17], but experimental results were conducted with a constant power source (CPS) emulating the PV interface. The option of running the MPPT logic periodically, say every 1s, and then comparing the magnitudes of the modulating signals from parallel loops is not considered in this discussion since it should lead to a slower dynamic response.

2.2 The V vs. I curves of DERs in a DC Nanogrid

The DC nanogrid considered in this work is a unipolar single-bus system as shown in Figure 2. 1. It consists, without loss of generality, of a RES, a storage unit and a variable load. The impedances between DERs and load(s) are assumed to be negligible. The nanogrid is controlled in a de-centralized way with a hierarchical structure based on DBS. In such a case, the current injected by a DER (I_{DC}) varies with the locally measured grid voltage (V_{DC}) according to a particular V vs. I curve. This usually consists of various segments including droop, maximum power point tracking (MPPT) and current limiting.

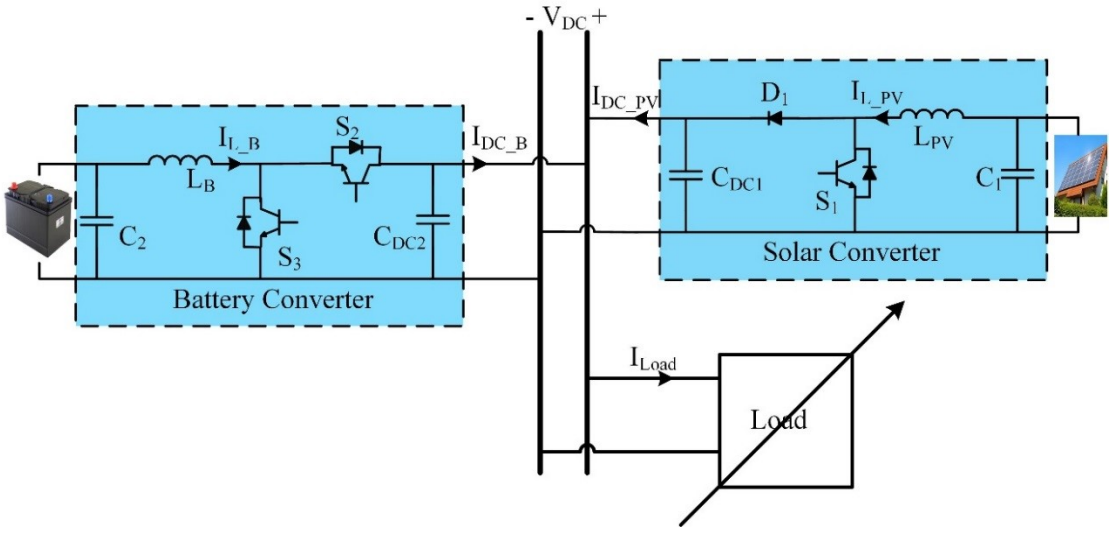

Figure 2. 1 : Unipolar DC nanogrid with one RES (PV), one storage unit and a variable load.

For droop control, the injected current is given by:

$$I_{DC} = (V_{NL}\text{-}V_{DC})\frac{1}{R_d} \tag{2.1}$$

Where V_{NL} is the threshold or no-load voltage and the slope of the V vs. I curve is:

$$R_d = \frac{\Delta V_{DC}}{\Delta I_{DC}} \tag{2.2}$$

RESs such as solar PV are expected to operate with MPPT in cases of high power demand by the load or when one can charge the storage unit(s). Finally, there should be a current limit mode to prevent the converter from injecting/absorbing more power than either the source or storage means allow as well as for the converter to protect itself against over-currents.

Figure 2. 2 shows the sketch of two typical V vs. I curves for the storage unit (droop and current limit) and the RES (droop, MPPT and current limit). The voltage levels are defined in a per unit (pu) basis. The DC nanogrid operates with a voltage regulation of about ± 5%, giving an operating DC bus voltage range between 1.05 and 0.95 pu. The threshold voltage for the droop segment of the RES is set at the maximum DC nanogrid voltage, thus, V_{NL_S} = 1.05 pu. The RES operates in droop mode, increasing the injected current as V_{DC} decreases, up to the point where it reaches its maximum power capacity. Then, its V vs. I curve changes to an MPPT mode, where the injected current increases less than in the droop region, for a given decrease in the DC bus voltage. In the case shown in Figure 2. 2, and considering rated solar irradiance, the solar converter changes to the MPPT mode when the DC bus voltage drops to 1.025 pu. When the DC bus voltage further drops to 0.95 pu, and for rated solar irradiance, the solar converter operates in the current limit mode. For lower solar irradiances, transition from droop to MPPT mode occurs at a higher value of V_{DC} while the MPPT to current limit occurs for a lower value of V_{DC} as shown by the dashed line in Figure 2. 2.

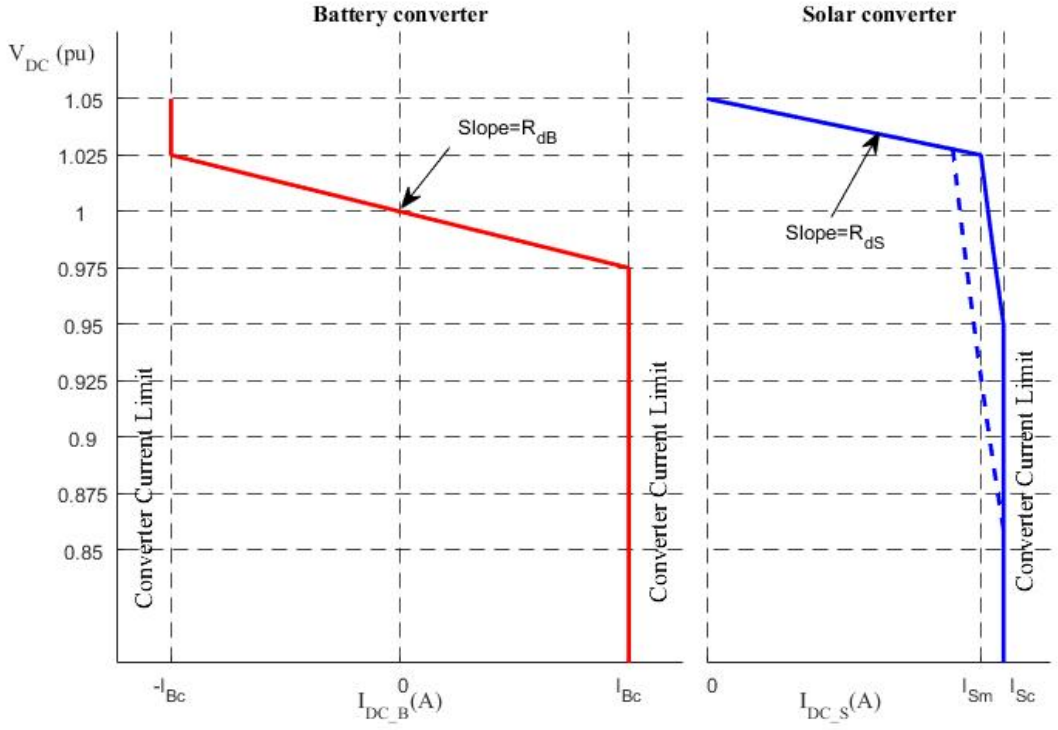

Figure 2. 2 : Storage unit and solar (PV) V vs. I curves.

As for the storage converter, its threshold voltage (V_{NL_B}) can be selected as 1 pu, the rated voltage of the DC nanogrid. The storage means is charged ($I_{DC\_B} < 0$) when $V_{DC} > V_{NL\_B}$ and is discharged, into the DC nanogrid, otherwise. It operates in the droop region for a DC bus voltage between 1.025 and 0.975 pu. By making the rated power of the storage system equal to the rated power of the RES, the former will be able to draw rated PV power at the no-load condition. In such a case, the droop factor of the storage system (R_{dB}) will be the same as that of the RES (R_{dS}). However, the RES and the storage unit will not operate together in the droop mode since their droop regions are defined for different DC bus voltage ranges. For voltages above 1.025 pu, the storage converter absorbs its rated current (I_{Bc}) and for voltages below 0.975 pu, it injects rated current, provided that its state-of-charge (SoC) is within acceptable values. If not, the injected/absorbed current should be decreased.

Neglecting the voltage drops between the DER interfaces and the equivalent system load, the DC bus voltage (V_{DC}) of a nanogrid operating with DBS and multiple DERs can be determined from:

$$I_{Load} = \sum_{i=1}^{n} I_{DC\_i} \tag{2.3}$$

Where I_{DC_i} are computed according to the V vs. I curves of the n DERs. With the value of V_{DC}, one can then calculate the individual contributions of the DERs from their V vs. I curves.

2.3 Control Scheme for the RES and Storage Units

The conventional interface topologies for DC power sources and storage units usually employed in DC nanogrids are shown in Figure 2. 1. The actual power source and storage units are located in the low voltage (LV) side of the power interface along with a boost inductor. The converters usually operate in continuous conduction mode (CCM) and low current ripple. Conversely, the high voltage (HV) side current, that is injected into the DC nanogrid, tends to be pulsed, thus requiring a larger HV side filter capacitor ($C_{DC1} > C_1$.).

Although the V vs. I curves of the RES and storage units have been defined for the DC nanogrid voltage (HV side) and injected current in the HV side, it is more convenient to control the average (DC) value of the boost inductor current, in the LV side, which presents a small ripple. In order to convert the reference current value in the HV side, obtained from the V vs. I curve, into

one for the boost inductor, one can use the power balance equation with a typical converter efficiency (η):

$$I_L V_{in} \eta = I_{DC} V_{DC} \tag{2.4}$$

For the design of the controller of the inductor current loop, a transfer function for boost type DC-DC converters is needed. This has been presented in the literature [43, 60] in term of the ratio between the inductor current $\tilde{i}_L(s)$ and the duty ratio $\tilde{d}(s)$ and is given by:

$$G = \frac{\tilde{i}_L(s)}{\tilde{d}(s)} = \frac{CV_{DC}s + 2I_{DC}}{LCs^2 + \frac{L}{R}s + (1-D)^2} \tag{2.5}$$

Where C is the HV side capacitor, L is the inductance, D is the average duty cycle and R is the equivalent load resistance.

In such a case, an appropriately designed PI controller should suffice to provide zero error in steady-state with a good dynamic response. The details and design procedure for the converter and control loops are presented in Section 2.4. The schematic diagram of the current control loop of the RES and storage units are shown in Figure 2. 3 with S_2, S_3 and S_4 are the gating signals of the switches. They are similar but the value of the reference inductor current (I_{Lr}) will change with the type of V vs. I curve of the interfaces. An approach to determine this value, while transitioning from one mode to the next, as a result of DC nanogrid voltage and solar irradiation variations, is discussed in the following Sub-Sections.

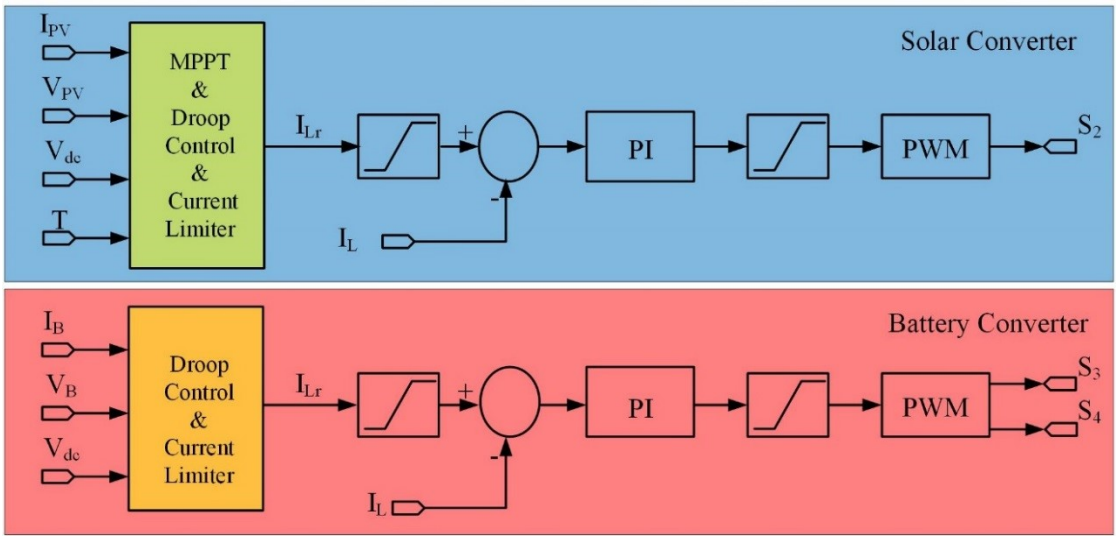

Figure 2. 3 : Control schemes of the solar and battery converters.

2.4 Control Scheme for the RES

As mentioned in Section 2.2, the RES interface will be controlled with a V vs. I curve that includes a droop, an MPPT and a current limit mode. This Section describes the MPPT algorithm considered in this work and then an approach for determining the reference inductor current in the three modes, as the solar irradiance and the DC nanogrid voltage vary.

2.4.1 The Maximum Power Point Tracking (MPPT) Algorithm

The MPPT algorithm used in this work is based on the assumption of linearity between the PV current at the maximum power point (MPP) and the maximum power, for all solar irradiance levels (2.6). The proportionality coefficient (K_p), as shown in (2.7), varies with the PV panel temperature (T) but can be adjusted using the hill-climbing method. Theoretical and experimental verification of this relation have been presented in [61, 62]. The actual power drawn from the PV panel at any given time is given by (2.8).

$$P_m(n)=K_p I_{PV}(n) \tag{2.6}$$

$$K_P = K_{Po} + \alpha T \tag{2.7}$$

$$P(n)=V_{PV}(n) I_{PV}(n) \tag{2.8}$$

Figure 2. 4 shows the P vs. I_{PV} curve of the solar panel for rated solar irradiance (2.8), in red, and the P_m vs. I_{PV} curve (2.6), in green. The latter depicts the values of I_{PV} required to operate at the Maximum Power Point (MPP) for all solar irradiance levels. For rated solar irradiance, I_{PV} at the MPP (I_{PV_MP}) corresponds to the point of intersection of these two curves. As the solar irradiance decreases, the point of intersection will occur at lower values of I_{PV}. By comparing these two curves, one can identify two regions. In Region I, for a given value of I_{PV}, P is larger than P_m. This occurs for I_{PV} smaller than I_{PV_MP}. In Region II, P is smaller than P_m, what occurs for I_{PV} larger than I_{PV_MP}. At Region I, the inductor current should be increased to drive the operating point towards the MPP. This is done using (2.9) and is shown in Figure 2. 4 for a few consecutive iterations. Conversely, in Region II, the inductor current should be decreased. This can be done according to (2.10), where K_{sc} is usually selected as the ratio between the current at the MPP and the short-circuit current of the PV panel at rated solar irradiance [61, 62]. If the difference between

P and P_m is less than a small value, one can keep the value of I_L constant, thus avoiding continuous variations around the MPP.

$$I_{Lm}=P(n)/K_p \tag{2.9}$$

$$I_{Lm} = K_{sc}I_{PV}(n) \tag{2.10}$$

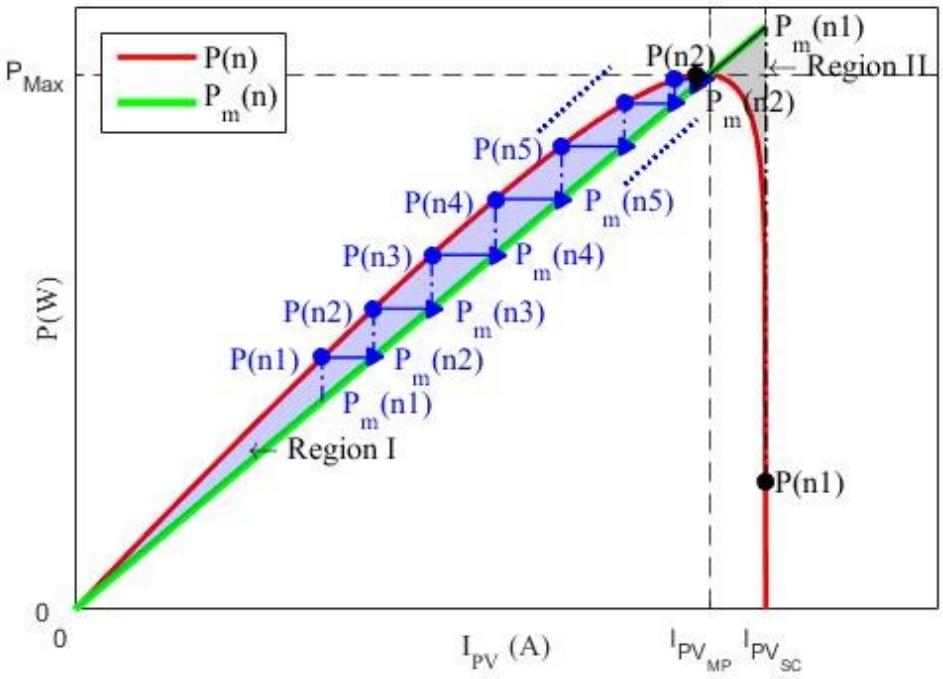

Figure 2. 4 : PV P vs. I curve.

2.4.2 Transitioning from one Mode of Operation to Another

As shown in the previous Sub-Section, the inductor reference current for operation in the MPPT mode is computed based on the PV panel conditions only. It is assumed that the DC nanogrid voltage (V_{DC}) entices the solar interface to operate in this mode. However, as V_{DC} varies, the solar converter might need to change to either droop or current limit mode. There, the value of the injected current is dictated by the V vs. I curve of the interface. The reference inductor current for operation in those modes can be calculated by reflecting those HV side currents to the LV side using (2.4). One challenge is to determine which reference current to use as the values of the solar irradiance and V_{DC} vary. Figure 2. 5 shows the V vs. I curve of the solar converter from Figure 2. 2 with some additional information. In solid lines, the reference currents that should be selected as the value of V_{DC} varies. The dashed lines show candidate values of currents which were not

selected in those V_{DC} segments. As an example, considering a V_{DC} slightly lower than V_{NL}, the value of I_{DC} in the droop mode (I_{DCd}), calculated from (2.1) and shown as a solid line, is lower than the values one would get for the MPPT (I_{DCm}) and current limit (I_{DCc}) modes, in dashed lines. While the value of I_{DCc} is known, that of I_{DCm}, which is expected to vary with the solar irradiance, is not. Besides, the value of V_{DC} at the transition from the droop to the MPPT mode changes with the solar irradiance, which is unknown, increasing as the solar irradiance decreases.

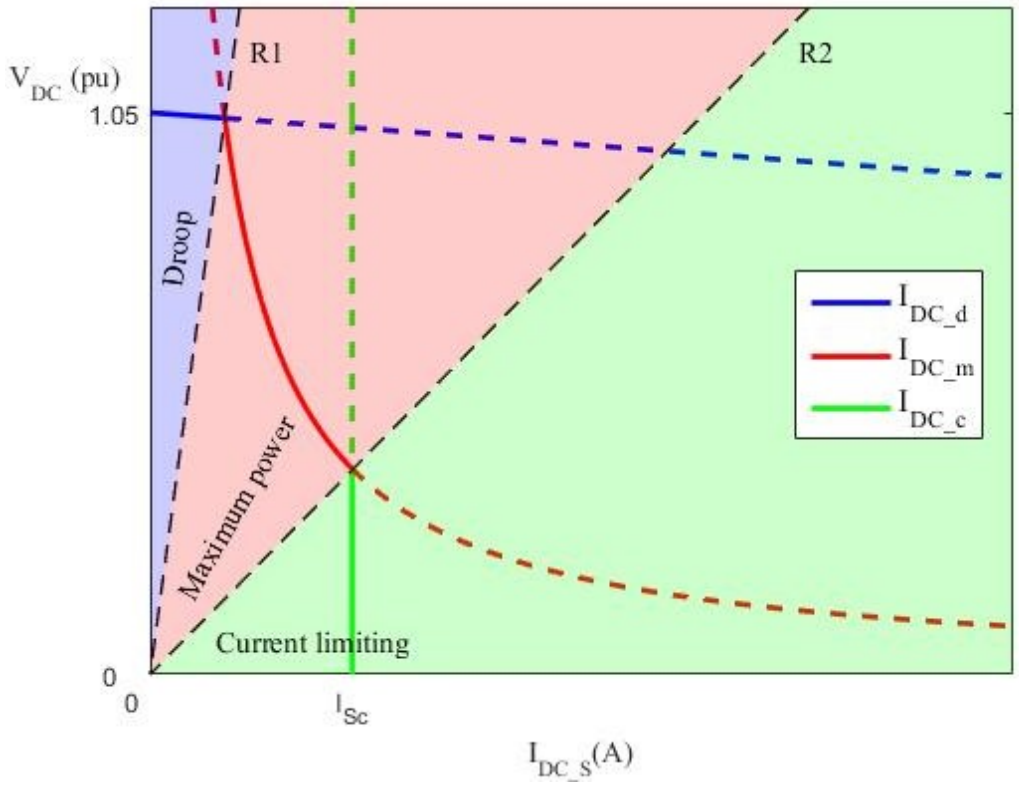

Figure 2. 5 : Solar V vs. I curve in droop, MPPT and current limit modes.

An algorithm to select the reference inductor current for the solar converter operating in droop, MPPT and current limit, for varying solar irradiance and DC grid voltages is proposed in this chapter. It is shown in the flowchart of Figure 2. 6.

The first step is to sense the values of the DC grid voltage (V_{DC}) and the PV current and voltage (I_{PV} and V_{PV}). Operation of the PV panel with $I_{PV} > I_{PV\_MP}$ is not desirable because of the resulting low value of V_{PV} and potentially exceeding the voltage gain limits of the boost converter. Therefore, the algorithm first verifies whether the system operates in Region II, where $P < P_m$. In such a case, the reference inductor current (I_{Lr}) should be reduced until operation is shifted to Region I. That is where the system is expected to operate for all three modes.

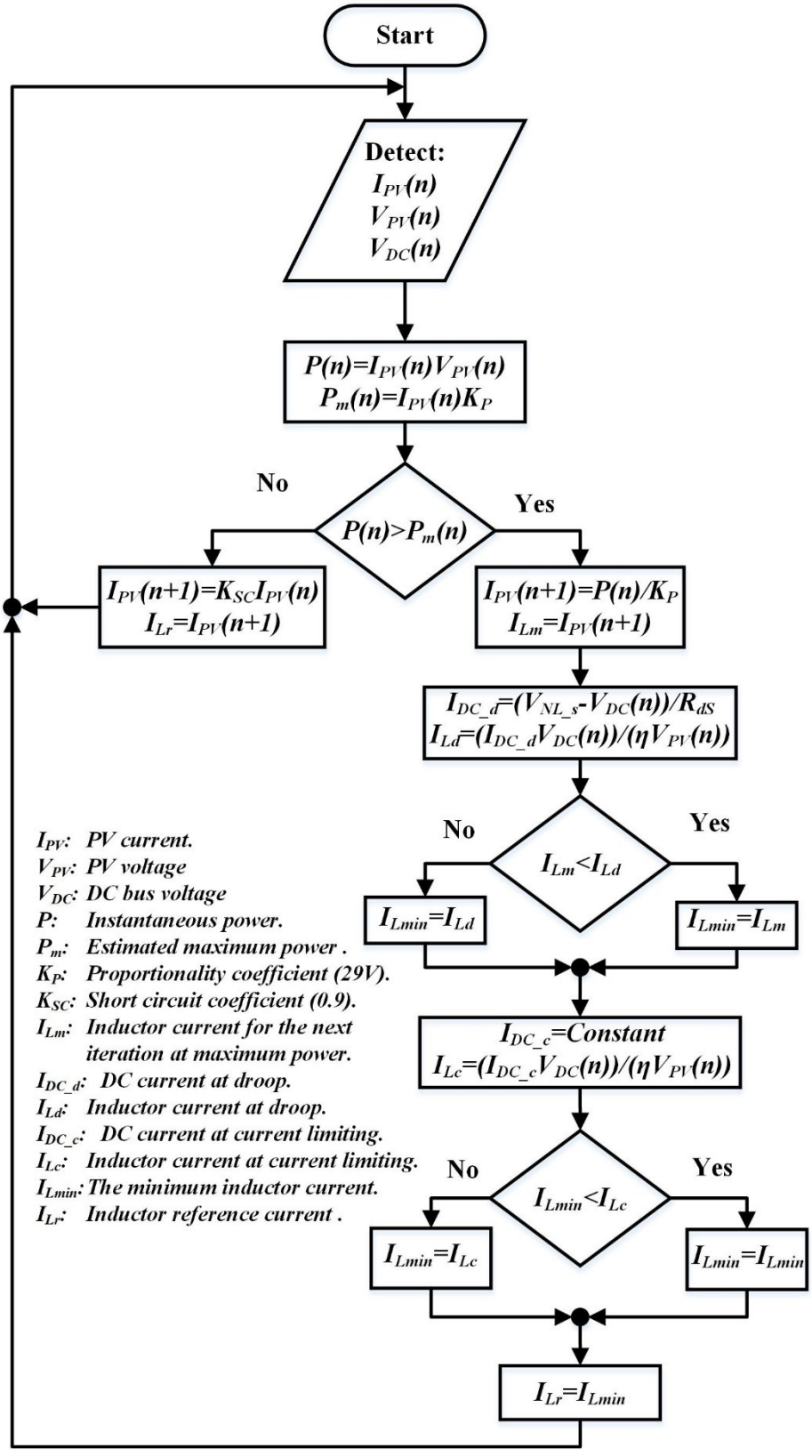

Figure 2. 6 : Proposed algorithm to calculate the reference current for the PV converter with smooth transition between modes of operation.

When $P > P_m$, the algorithm computes a candidate value for the next cycle of the reference inductor current according to the MPPT algorithm (I_{Lm}), which is a higher value than the actual I_{PV} according to (2.9). I_{Lm} is then compared to the candidate value from the droop mode (I_{Ld}). This is a function of V_{DC} and is computed from I_{DC} using the droop equation (2.1) reflected to the PV/LV side of the boost converter (2.4). The lowest of the two values is called I_{Lmin} and is selected for a final comparison with the current limit value, reflected to the PV/LV side of the boost converter (I_{Lc}). This is important since, as shown in Figure 2. 5, the value of I_{DC} in the current limit mode can become lower than those from the droop and MPPT modes, dashed lines, for low values of V_{DC}.

To illustrate the proposed algorithm, let us consider the case of a *high* V_{DC} and solar irradiance, where the solar converter is expected to operate in the droop mode. In this case, one should have a *low* I_{Ld} similar to I_{PV}. This value is also considered for the MPPT logic. In Region I ($I_{PV} < I_{PV\_MP}$), the MPPT algorithm would compute $I_{Lm} > I_{PV}$ and $> I_{Ld}$, what would keep operation in the droop mode. It should be noted that the value of I_{PV_MP} for that solar irradiance level is unknown and irrelevant. On the other hand, as the solar irradiance decreases and I_{PV_MP} becomes lower than I_{PV} and I_{Ld}, the value of I_{Lmin}, changes to I_{Lm}, and the converter starts to operate in the MPPT mode, seamlessly.

2.5 Control Scheme for the Storage Unit

As mentioned in Section 2.2, a storage unit usually operates in two modes: Droop and current limit. However, its state-of-charge (SoC) must be kept within certain limits and plays a role in the current values of its V vs. I curve as discussed below.

2.5.1 Transition from one Mode of Operation to Another

The control algorithm of the battery converter is similar to that of the solar converter. It does not have an MPPT mode, but depending on the state-of-charge (SoC) of the battery, the converter should prevent its further discharge or charge. In the proposed algorithm, first one computes the value of the inductor reference current according to the droop curve (I_{Ld}) based on the values of the grid voltage (V_{DC}) and the battery voltage (V_{Bat}). If I_{Ld} is positive, one checks whether the SoC is smaller than, say 20%, when the reference current (I_{Lr}) should be equal to zero to prevent any further battery discharge. Otherwise, I_{Lr} should be the smallest between I_{Ld} and the reference inductor current based on the current limit (I_{Lc}), as for the solar converter. On the other

hand, when I_{Ld} is negative and the SoC is high, say 95%, I_{Lr} should be equal to zero to prevent any further battery charge. Otherwise, I_{Lr} should be the largest between I_{Ld} and I_{Lc}, both negative values. The flowchart of the control algorithm for the battery converter is shown in Figure 2. 7.

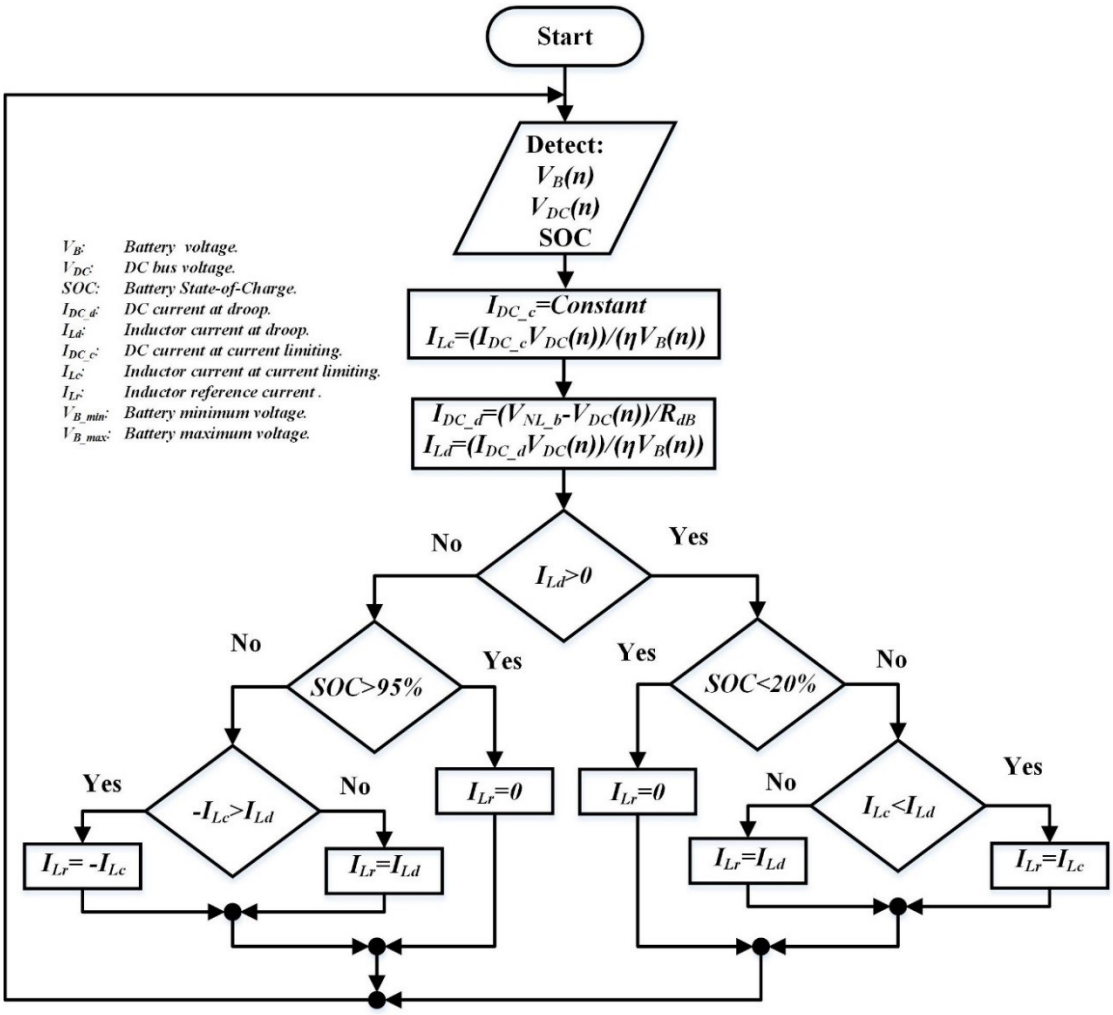

Figure 2. 7 : Algorithm to calculate the reference current for the battery converter considering the SoC.

2.6 Experimental Set-up

The DC nanogrid shown in Figure 2. 1 was built in the laboratory for verifying the performance of the proposed control strategies. Its rated voltage is 48 V, and the DC bus voltage should be kept between 45.5 V and 50.5 V in the normal operation range (~ +/- 5%). A Solar Array Simulator (SAS) from Agilent (E4350B) was used as the PV source, which at rated solar irradiance has a maximum power of 213 W at 7.35 A and 29 V. Thus, the value of K_p was selected as 29 and

the temperature effects were neglected in the experimental results with the SAS. The storage unit is based on a 165 F Maxwell supercapacitor.

A three-phase Semikron inverter was employed to realize the power electronic interfaces, with one leg of the three-phase inverter used for each DER. The 1500 µF capacitor at the DC bus of the inverter corresponds to the main filter at the DC bus of the nanogrid. The converters will be switching at 20 kHz. An LC filter (100 µH and 470 µF) is connected between two phases of the three-phase inverter and the storage and the source elements, to create the classical Class C DC-DC converter. The overall power electronics interface is illustrated in Figure 2. 8.

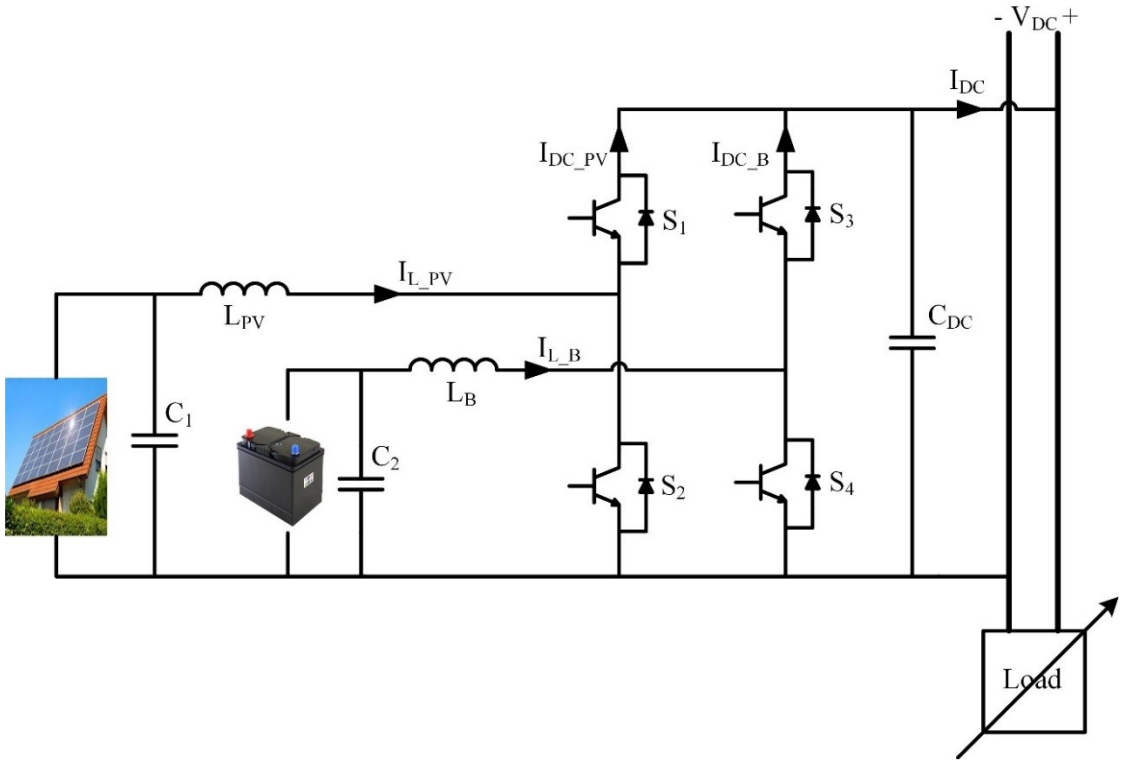

Figure 2. 8 : Experimental power electronics interface.

The control schemes of the RES and storage unit are implemented in a single dSPACE DS-1103. Concerning the parameters of the V vs. I curves, the no-load voltages of the solar and storage converters are V_{NL_S} = 50.5 V and V_{NL_B} = 48 V, respectively. For the definition of the main current values (I_{Sm} and I_{Sc}), it is assumed that the converter is ideal and the impact of its losses on the V vs. I curve of the solar converter can be represented by a decrease in the solar irradiance, and power produce by the solar panel. At rated solar irradiance, an ideal solar converter should inject rated PV power (213 W) at V_{DC} = 49.2 V (~1.025 pu) and I_{Sm} = 4.32 A. From there, one can compute

the droop slope as R_{ds} = 0.289 Ω. The current limit mode will be activated for rated solar irradiance when the converter injects rated power for V_{DC} = 45.5 V (~0.95 pu), that is I_{Sc} = 4.68 A. As for the storage unit, its rated current is such that it can absorb all PV power for rated solar irradiance in case of no-load. Therefore, $I_{Bc} = I_{Sm}$ = 4.32 A and R_{dB} = 0.289 Ω.

The current control loop of both DERs employ a PI type-III compensator. They were designed for the same plant with a transfer function shown in (4) and for a crossover frequency of f_x = 2 kHz (10% of the switching frequency) and phase margin of PM = 80º. The key system parameters for the ideal power electronics interface are taken as: V_{DC} = 48 V, I_{DC} = 4.44 A, R = 10.8 Ω, L = 100 µH, C = 1500 µF, and D = 0.4. Where R is selected for the maximum load that could be supplied by the solar converter and D is the duty cycle for operation with MPPT at rated solar irradiance (V_{PV} = 29 V) and a DC nanogrid voltage of V_{DC} = 48 V. The resulting PI controller parameters are K_{PI} = 0.0114, τ = 171 µs and T_P = 37 µs. The minimum time-step that could be used in dSPACE was 20 µs.

2.7 Experimental Tests and Results

The main objective of the experimental tests is to verify whether the proposed techniques are effective in terms of changing the mode of operation of the DER power interfaces in a seamless and smooth fashion. Two configurations will be tested: The solar converter operating by itself and then along with the storage unit. The mode of operation of the DER(s) of the nanogrid shall change as a result of load as well as solar irradiance variations. The resistive load bank used in this experiment consists of 8 parallel switchable resistors of 40 Ω.

2.7.1 Solar Converter Operating in Stand-alone

The solar converter is controlled with the V vs. I curve depicted in Figure 2. 2, using the control algorithm described in Section 2.4 and the power interface and PI controller discussed in Section 2.5. The first experiment concerns the behavior of the system for the solar converter operating with rated solar irradiance. The power demanded by the load is increased by switching in equal resistors rated at 40 Ω. The following waveforms are presented in Figure 2. 9- Figure 2. 11, for various load variations: The DC nanogrid voltage (V_{DC}), the current of the PV panel (I_{L_PV}), the load current (I_{DC} in Figure 2. 7) and other waveforms that show the action of the proposed control algorithm.

In Figure 2. 9, the load changed from R_1 = 39.53 Ω to R_2 = 19.5 Ω. The steady-state values of V_{DC} for both loads, 50.13 V and 49.77 V, correspond to the droop region. However, during transient conditions, V_{DC} decreased below 49.2 V, which concerns the MPPT region. The dynamic response of the system is relatively slow because the value of the injected current cannot increase much as V_{DC} decreases in the MPPT mode. The execution of the proposed control algorithm can be verified in the bottom screen of Figure 2. 9. Initially $I_{Ld} < I_{Lm}$ but as V_{DC} decreases, I_{Ld} increases, exceeding the value of I_{Lm}. This sets a *control flag* to "high" what indicates operation in the MPPT mode. This can be confirmed by observing the values of I_{Lm} and I_{L_PV}. As V_{DC} bounces back above 49.2 V, I_{Ld} becomes smaller than I_{Lm} and the system returns to the droop mode as indicated by the "low" *control flag*.

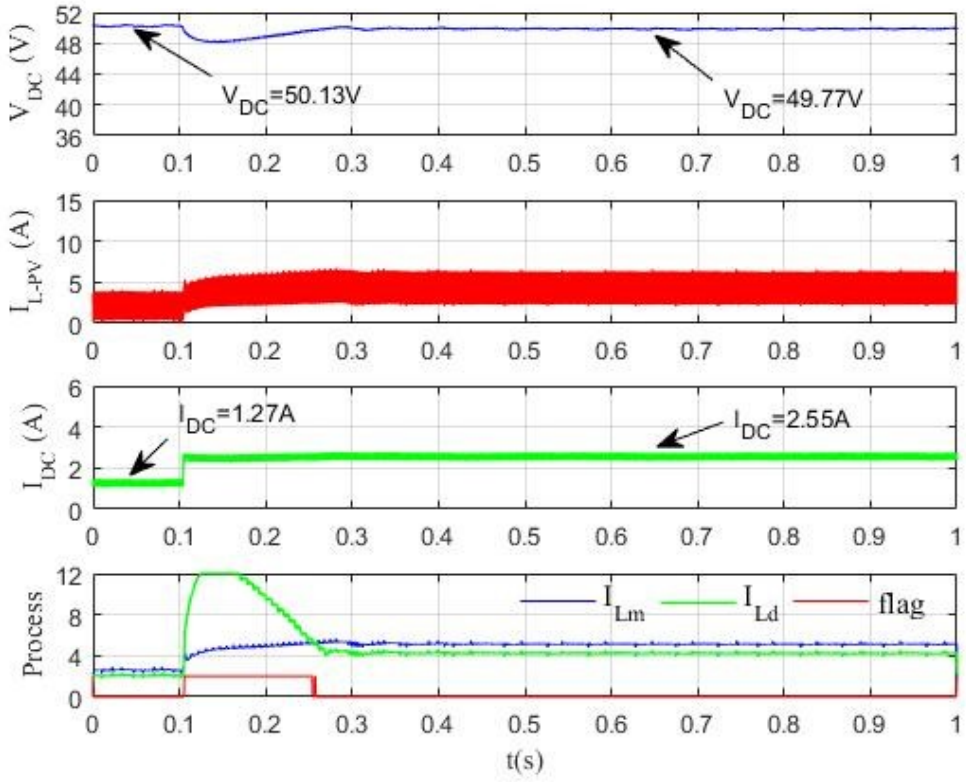

Figure 2. 9 : DC bus voltage, load current, solar inductor current and the process currents at load variation for solar converter operates in standalone mode with operation in droop mode in both region.

In Figure 2. 10, the load changed from R_1 = 13 Ω to R_2 = 9.8 Ω. The steady-state values of V_{DC} for both loads, 49.4 V and 43.2 V, correspond to the droop and MPPT modes, respectively. This can be asserted by observing the value of the *control flag* and by comparing the values of I_{Ld}

and I_{Lm}. The final value of I_{DC} is 4.39 A, which is higher than I_{Sm} (4.32 A), defined as the minimum current for the MPPT mode at rated solar irradiance. The value of V_{DC} is lower than that for the ideal curve for rated solar irradiance shown in Figure 2. 2. This can be justified by modeling the converter losses as a decrease of the solar irradiance, represented by the dashed curve in Figure 2. 2. Lastly, in Figure 2. 11, the load changed from R_1 = 9.8 Ω to R_2 = 7.8 Ω. The steady-state values of V_{DC} for both loads, 43.2 V and 37.8 V, correspond to the MPPT and current limit modes, respectively. It should be noted that these values are lower than those expected from the ideal condition operation, similarly to what happened for the previous case. The injected current value at the current limit mode is 4.72, very close to I_{Sc} (4.68 A). The mode of operation is confirmed based on the value of the *control flag* and by comparing the values of I_{Lm} and I_{Lc}. As expected, the value of V_{DC} varies more for smaller I_{DC} variations in the MPPT and current limit modes.

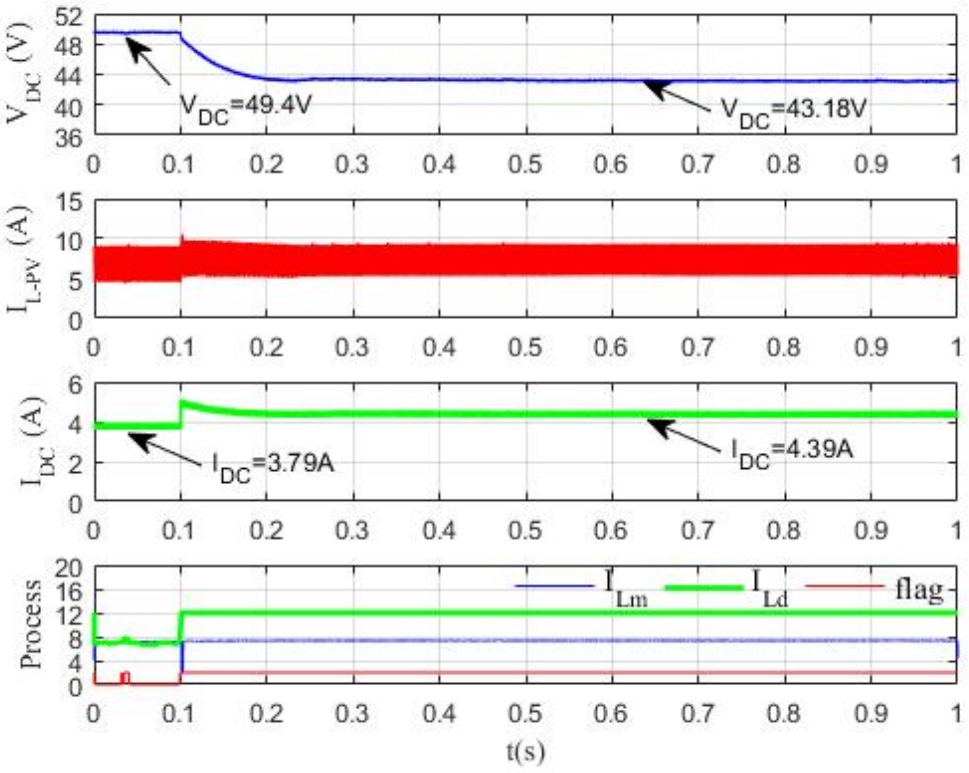

Figure 2. 10 : DC bus voltage, load current, solar inductor current and the process currents at load variation for solar converter operates in standalone mode with operation changed from droop mode to maximum power mode.

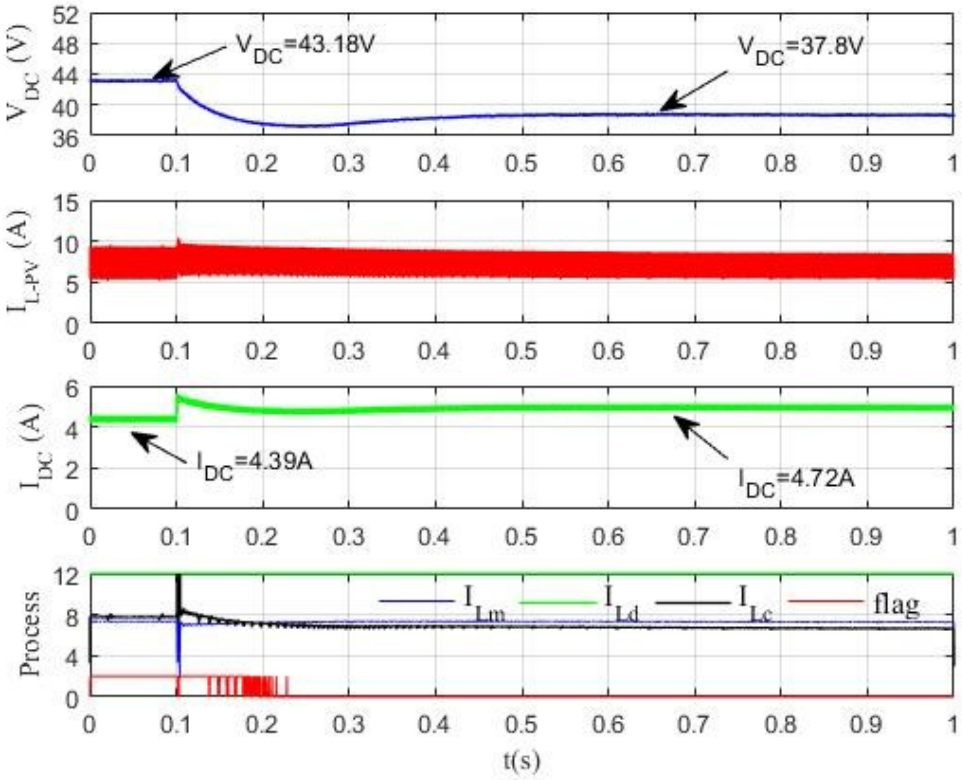

Figure 2. 11 : DC bus voltage, load current, solar inductor current and the process currents at load variation for solar converter operates in standalone mode with operation changed from maximum power mode to current limiting mode.

Next, the performance of the system for the variation of the solar irradiance with a constant load was verified. This is shown in Figure 2. 12. First, for a load of R = 13 Ω and rated solar irradiance (P_{PV_M} = 213 W), V_{DC} = 49.4 V, above V_{DC} = 49.2 V (1.025 pu), which was defined as the lowest DC bus voltage in the droop mode for rated solar irradiance and ideal power converter. Then, the solar irradiance is decreased to 90% (P_{PV_M} = 192 W) resulting in V_{DC} = 47.7 V, above V_{DC} = 45.5 V (0.95 pu), which was defined as the lowest voltage in the MPPT mode. Again, the change in mode of operation can be observed from the value of the *control flag*.

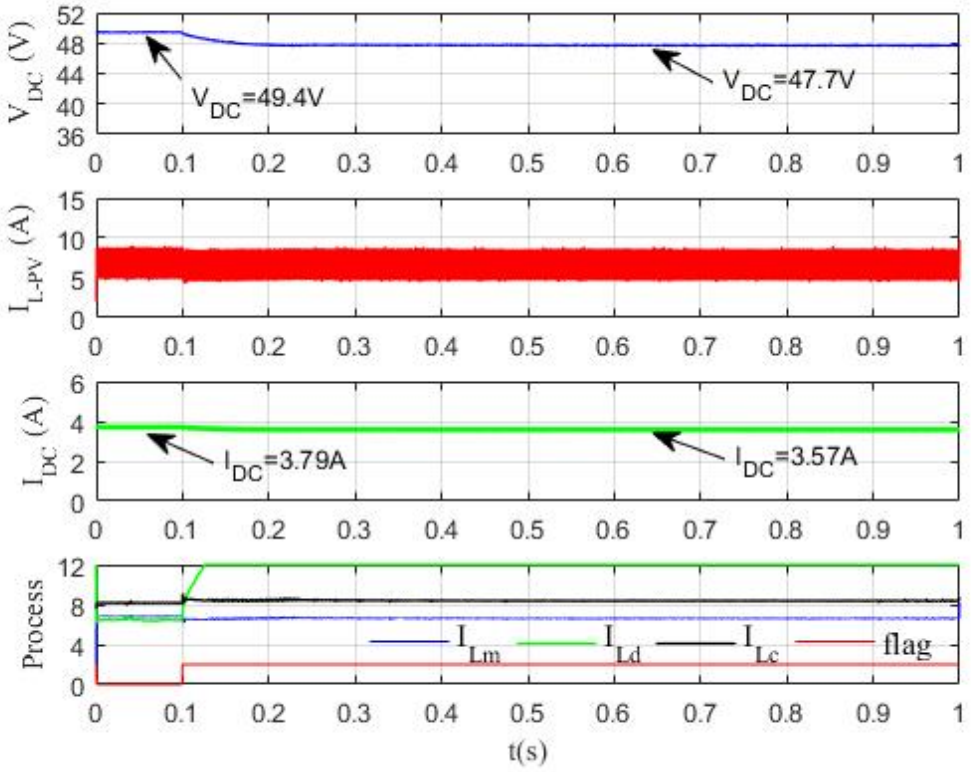

Figure 2. 12 : DC bus voltage, load current, solar inductor current and the process currents at Solar irradiance variation for solar converter operates in standalone mode with operation changed from droop mode to maximum power mode.

Finally, in Figure 2. 13, the case of solar irradiance variation for the converter operating in the MPPT mode is considered. For that, a load of R = 9.8 Ω is used, while the solar irradiance changes from 100% to 90%. The values of V_{DC} decrease from 43.2 V to 41 V. These are lower than V_{DC} = 45.5 V (~0.95 pu), which was defined for rated solar irradiance and ideal converter. If a higher DC bus voltage is required for lower solar irradiances, than the values of I_{Sm} and I_{Sc} should be re-defined accordingly. Regarding the mode of operation, one can see in the screen at the bottom, that the value of I_{Lm} is the smallest of all, keeping the *control flag* at high, as expected for continuous operation in the MPPT mode. The case of a transition from the MPPT mode to the current limit mode due to a solar irradiance variation is not possible.

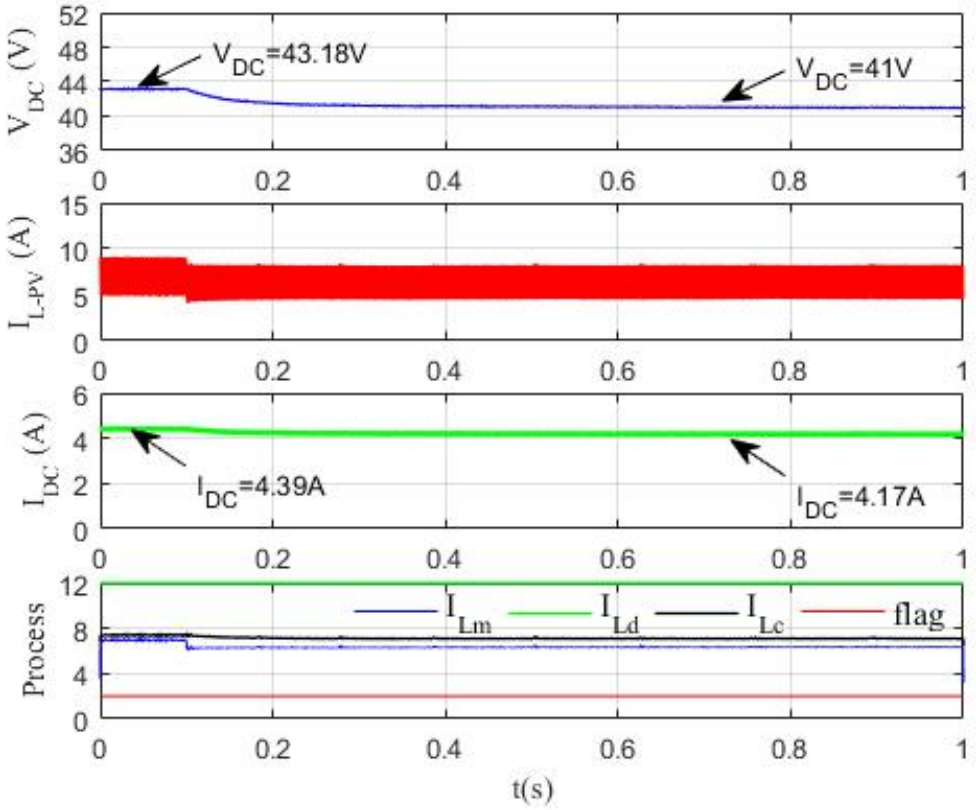

Figure 2. 13 : DC bus voltage, load current, solar inductor current and the process currents at Solar irradiance variation for solar converter operates in standalone mode with operation in maximum power mode in both region.

2.7.2 Solar and Storage Converters Operating Together

In the second set of experiments, the solar and the storage converters operate together. With the parameters defined in the previous Sections with rated solar irradiance, the solar converter should operate in the MPPT mode, from no-load to full DC nanogrid load (~2 P_{PV_M} = 426 W). The storage converter should operate in the droop mode, absorbing power under light-load conditions, ($V_{DC} > V_{NL\_B}$ = 48V) and supplying otherwise. As a result, the DC bus voltage should vary between 49.2 V (1.025 pu) and 46.8 V (0.0975 pu).

Figure 2. 14 shows, on the top, the V vs. I curve of the DC nanogrid, for varying load impedances, which is obtained with the V vs. I curves of the solar and storage converters, in the bottom. The markers on the plots depict the experimental operating conditions for the following DC nanogrid loads (in Ω): ∞, 39.5, 19.5, 13, 9.8, 7.8, 6.6, 5.6 and 4.9. For the lowest load impedance, the solar converter operates in MPPT and the storage unit in current limit mode.

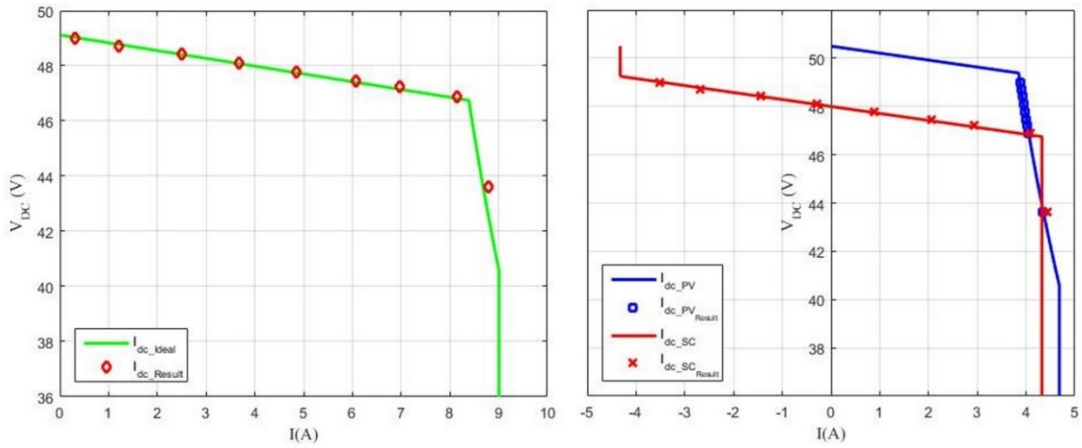

(a) (b)

Figure 2. 14 : Solar and battery operating together: a) Measured DC bus voltage and load current, b) Measured DC bus voltage and estimated DC current component from solar and battery.

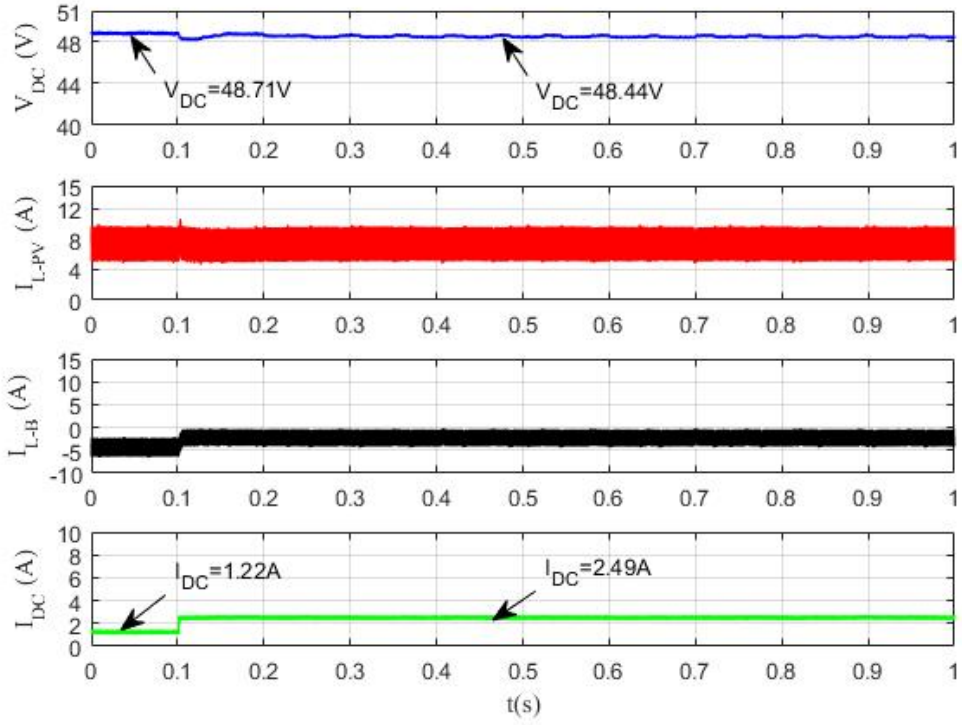

Figure 2. 15 : DC bus voltage, load current, solar inductor current and battery inductor current at load variation for solar and battery operate together with the PV operating in MP mode and battery charging with droop mode.

The dynamic response of the DC nanogrid operating with DBS and the proposed control algorithms for the solar and the storage units are also shown. In Figure 2. 15, on can see DC nanogrid voltage (V_{DC}), the current of the PV panel (I_{L_PV}), storage unit (I_{L_B}), load current (I_{DC}) for rated solar irradiance (P_{PV_M} = 213 W) and "light loads." At t = 0.1s, the load resistance changes

from R_1 = 39.5 Ω to R_2 = 19.5 Ω and the DC bus voltage decreases from 48.7 V to 48.4 V. The solar converter operates in MPPT, with minimum current variation. Conversely, the amount of power absorbed by the storage converter decreases, as expected. Figure 2. 16 shows the transient response of the system under a "heavy load" condition. At t = 0.1s, the load resistance changes from R_1 = 5.6 Ω to R_2 = 4.9 Ω and the DC bus voltage decreases from 46.9 V to 43.6 V. The solar converter still operates in MPPT with a current that does not change much. Conversely, the storage unit changes from droop to current limit mode, where it cannot help with voltage regulation. As a result, the DC bus voltage drops below 46.8 V (0.975 pu) and the transient response of the system is slower than before.

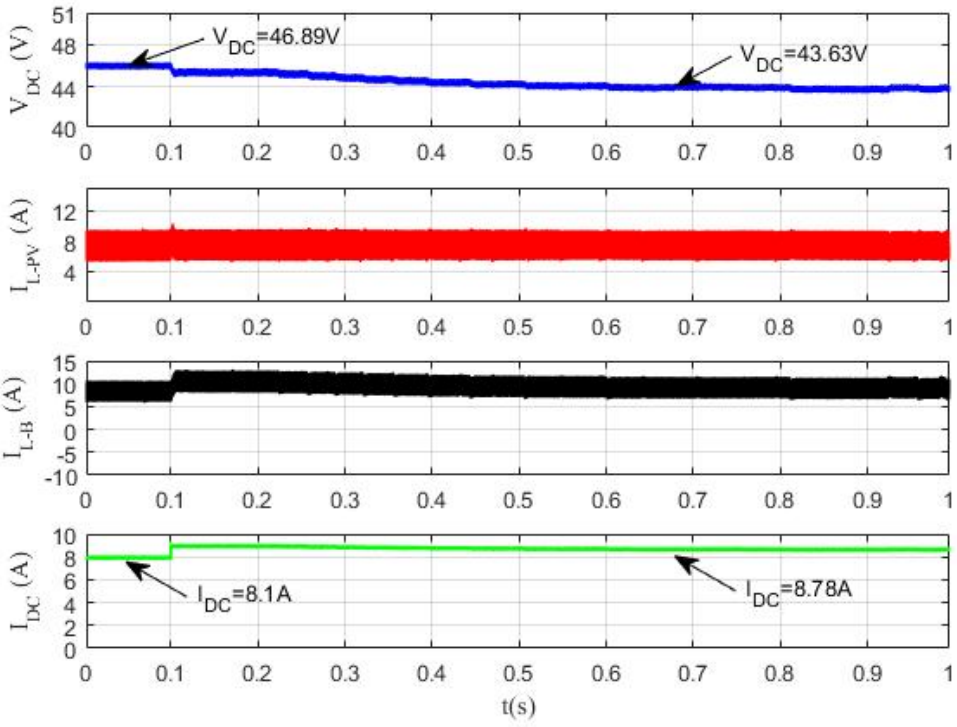

Figure 2. 16 : DC bus voltage, load current, solar inductor current and battery inductor current at load variation for solar and battery operate together with the PV operating in MP mode and battery operating mode change from discharging with droop mode to current limiting mode.

2.8 Conclusions

This chapter has presented a novel control algorithm for a single-stage photovoltaic (PV) interface of a DC micro or nanogrid that employs DC bus signaling (DBS). Its key feature is a seamless transition between DBS control modes that are based on source side parameters, such as maximum power point tracking (MPPT) and DC grid side parameters, e.g., droop. In such a case,

search type MPPT algorithms are hard to use due to the absence of an energy storage element, usually found in the intermediate DC bus of two-stage interfaces. Thus a suitable non-search MPPT scheme is used and a logic for selecting which reference signal should be used for determining the mode of operation (droop, MPPT and current limit) is proposed. The performance of the algorithm is verified experimentally for an autonomous DC nanogrid. First, tests with a "PV only" system are conducted, resulting in smooth transitions and DC bus voltage variations. Load variations with the PV interface operating in the MPPT mode are relatively slow due to the inherent power limitation of the PV. The algorithm is also tested in a "PV plus storage" system with the PV operating in the MPPT mode. There, the storage unit provides a faster dynamic response until load increases drive it to operation in the current limit mode.

CHAPTER THREE: CONTROL OF STORAGE UNIT

3.1 Introduction

Due to environmental issues and the shortage of fossil fuel, the participation of renewable energy sources (RESs) in the power system is expected and desired to increase. Since these are suitable for decentralized deployment, the power distribution system of the future could be designed and operated considering a hierarchical configuration consisting of micro and nanogrids. In fact, homes and neighborhoods can become net-zero energy nano and microgrids [1]. That is to say that the total amount of energy used by a home and/or neighborhood, on an annual basis, is nearly equal to the amount of energy produced by RESs [6]. Assuming that micro and nanogrids are expected to be able to operate autonomously, the most significant challenge is power availability, because the power generated by the RESs is variable and depends on environmental conditions. In such a case, the nano and microgrids should be supported by properly sized and controlled energy storage systems (ESSs). Besides, the system should be able to balance supply and demand obtaining high levels of power quality in both steady-state and transient conditions.

The most commonly used energy storage elements in ESSs are batteries due to high energy densities. On the other hand, in general, batteries present relatively low power densities, making it difficult for them to compensate for large and sudden power unbalances. This condition can lead to increased power losses and high operating temperatures, which can significantly decreases the lifetime of the battery. Keeping the battery operating as close as possible to the ideal condition respecting the recommended SoC ranges, charging and discharging rates, temperature, cell-charge equalization is very important according to [40, 41]. Hybrid energy storage systems (HESSs), with battery and supercapacitor (SC), have been proposed to strike a balance between the complementary characteristic of these two energy storage means [42, 43]. The SC can compensate transient power fluctuations while the battery supplies the average and slow varying power demand [42-44].

The literature reports several approaches for controlling the power sharing between battery and SC in applications with HESSs. A two level electrical storage system is presented in [45] to deal with the power fluctuation of RESs. The stress on the battery can be mitigated by a control

algorithm that extracts the maximum power from the RESs and uses the SC to deal with the high frequency components of the RES' power fluctuation [46]. A model predictive control system for a HESS is proposed in [47] where a model of the battery and SC is used to generate the gating signals of the DC-DC converters (interfaces) with the high frequency power supplied by the SC. A supervisory energy management strategy (EMS) based on neural networks, which is rather complicated, is proposed in [48]. It has been shown in [49] that a dynamic EMS in a RES integrated with a HESS can provide effective active DC link voltage regulation and reduced current stress on the battery [49]. All these algorithms are based on centralized control employing a communication link between the DERs. However, if communication fails, the system is disabled. Thus, centralized control schemes tend to present lower reliability [26-28]. Since battery and SC in a HESS are usually co-located and the main task of the SC is to prevent the fast varying current components from circulating through the battery, a simple scheme with frequency component separation, based on a low pass filter (LPF) or a high pass filter (HPF) is usually employed [50]. The high frequency and fast varying current components to be supplied by the HESS are processed by the high power density SC while the average and slow varying components are dealt with by the battery. One issue with this approach is that it tends to forfeit the potential contribution of the SC and its high power capabilities to dynamically improve power quality in a DC nanogrid.

DC bus signaling (DBS) and droop control are frequently employed in DC nano and microgrids with various DERs operating in a decentralized way [49]. They are based on locally measured variables, such as DC bus voltage, and provide an effective means for setting power sharing among parallel units in steady-state conditions. This is achieved by defining two parameters: The droop ($\Delta V/\Delta I$) slope (factor) and the threshold (no-load) voltage. The first is usually defined based on the power ratings of the DERs and remains constant. The larger units have smaller droop slopes to take larger shares of the power/current required for balancing supply and demand, mitigating DC bus voltage variations (ΔV). The threshold voltage is used for energy management and can be updated by a supervisory controller employing low bandwidth communication, but is not essential for system operation. Disregarding the latter, for high reliability, and assuming that he SC and battery are not co-located, the SC unit should present a droop factor lower than that of the battery's to be able to contribute more to dynamic voltage regulation. However, additional means are required to accommodate its low energy capacity constraint. For that, a HPF with a properly selected cut-off frequency is proposed in this work.

Simulation and experimental results are presented to show that this approach can provide an improvement in the dynamic regulation of the DC nanogrid voltage as well as mitigate the fast current components in the battery unit.

3.2 Power Control and Current Sharing of DERs

The DC nanogrid considered in this chapter consists of a RES, battery and SC storage units and a variable load as shown in Figure 3. 1. The RES employs a uni-directional boost converter while the storage units require a bi-directional one, typically a class C DC-DC converter. The battery and SC can be controlled as a single HESS, in which case they should be co-located, or independently what is suitable for distributed energy storage units, as proposed in this work. The single-bus DC nanogrid is controlled in a decentralized way with a hierarchical structure based on DBS and droop control. However, no communication means for energy management is considered in this work. DBS uses the DC bus voltage itself as the communication link to coordinate the operation of DERs in a decentralized way. With droop control, the current (power) injected by each DER in the nanogrid depends on its threshold voltage (V_{NL}), where the injected current is zero, and its droop slope (factor) R_d as shown in (3.1). The latter determines how the injected current varies as a function of grid voltage variations.

$$I_{DC} = (V_{NL} - V_{DC})\frac{1}{R_d} \tag{3.1}$$

Where;

$$R_d = \frac{\Delta V_{DC}}{\Delta I_{DC}} \tag{3.2}$$

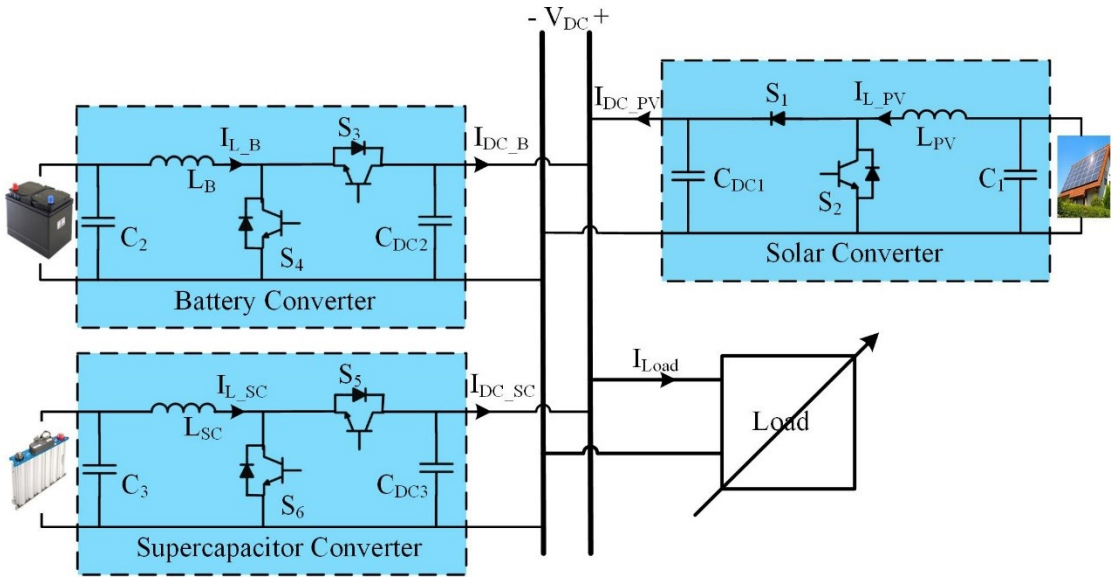

Figure 3. 1**:** Autonomous DC nanogrid considered in this study.

In the hierarchical structure, DBS is the primary control level of the nanogrid. The DC nanogrid considered in this chapter has a nominal voltage of 1pu. It was conceived to operate with a voltage regulation of about ± 5%, giving an operating DC bus voltage between 0.95pu and 1.05pu. In the case of the RESs, the threshold voltage is often taken as V_{NL_PV} = 1.05pu, higher than the threshold voltage of the energy storage unit or HESS, V_{NL_ST} = 1pu. In the concept of DBS, this gives the RESs, if available and producing power, the highest priority to feed the loads. As shown in Figure 3. 2, by the blue curve, the solar converter operates in three regions: droop, constant power, and constant current-limited with unidirectional power flow. When the DC bus voltage is between 1.05pu and 1.025pu, the solar converter operates with droop factor R_{dPV}. Therefore, the solar generates the maximum power at V_{DC} = 1.025pu and starts to operate at maximum power point tracking (MPPT) with the rated solar irradiance. When the PV has a maximum power less than the rated power, due to a lower solar irradiance, the solar converter should start to operate at MPPT before the DC bus voltage drops below 1.025pu, what can be done by "reprogramming" the V-I curve of the solar converter, as shown in the dashed line in Figure 3. 2. For instance, the solar converter should start to operate at MPPT with a DC bus voltage of 1.029pu with a maximum power of 90% from the rated power. When the DC bus voltage drops below 0.95pu for rated solar irradiance, the solar converter starts to operate in the constant current-limited mode.

The V-I curve of the energy storage unit or HESS is the red curve in Figure 3. 2, presenting only droop and current limiting modes. When the DC bus voltage is between 1.025pu and 0.975pu, the storage converter operates with droop factor R_{dST}. Otherwise, it operates with a constant (rated) negative current at a DC bus voltage higher than 1.025pu and constant positive current at a DC bus voltage lower than 0.975pu. The storage unit charges when the DC bus voltage is higher than 1pu, as indicated by a "negative injected current." Conversely, it discharges at DC bus voltages less than 1pu.

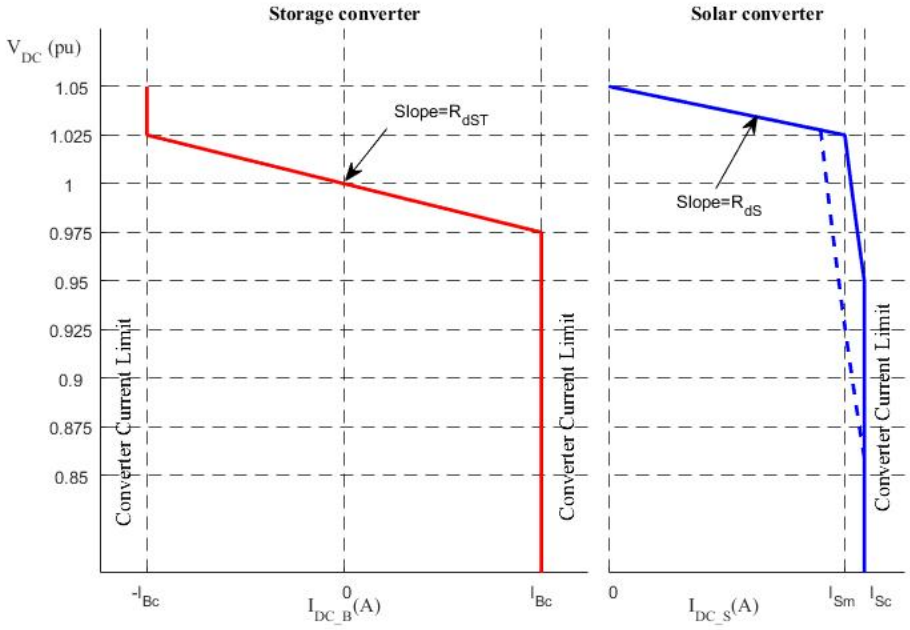

Figure 3. 2: V-I curves of the storage and solar (RES) converters.

3.3 Conventional and Proposed Control Schemes of the Battery-SC HESS

The conventional approach, shown in Figure 3. 3, the battery and SC are co-located and controlled as a HESS to realize a given V-I curve or droop characteristic. The supercapacitor operates in parallel with the battery to provide short bursts of power that eliminate the high-frequency component in the transient battery response, so the battery has a smooth transition. In this approach, the battery inductor current separated by LPF into low-frequency component generates the battery inductor reference current, and a high-frequency component generates the supercapacitor inductor reference current. In DC nanogrid with droop control, the DC bus voltage is sensed, and an outer voltage loop with a proportional (P) controller, that corresponds to the droop action, produces a reference current to be realized by the battery and the SC converters. The

slow and fast changing components of the reference current are split, by means of either a high-pass filter (HPF) or a low-pass filter (LPF). The slow ones are used as reference for the inner battery current control loop while the fast are used for the inner SC current control loop [42, 43, 63]. The bandwidth of the outer voltage loop is typically 10% of the inner current loops. It is very effective in preventing fast varying currents from flowing through the battery. The control scheme of the SC also includes a voltage loop to keep the voltage of the SC within a desired range, typically 50% to 100% of its rated value. By setting the reference voltage at 79% of the rated value, the SC has a state-of-charge with equal energy capacity to supply and absorb power before reaching the limit voltage values. Its bandwidth is typically 10% of that of the voltage (droop) loop of the HESS. Splitting the total current ($I_{L\_Storage}$) supplied by HESS into average components that is the battery reference current and the transient power component is the SC reference current helps in improving the operation of the battery and it does not give the DC bus voltage dynamics improvement. Moreover, a common voltage loop is used to generate the total current ($I_{L\_Storage}$) supplied by HESS, which means a communication between the battery and SC converters and that is not sufficient to be used in nanogrid controlled in decentralized control with droop control and DC bus signaling.

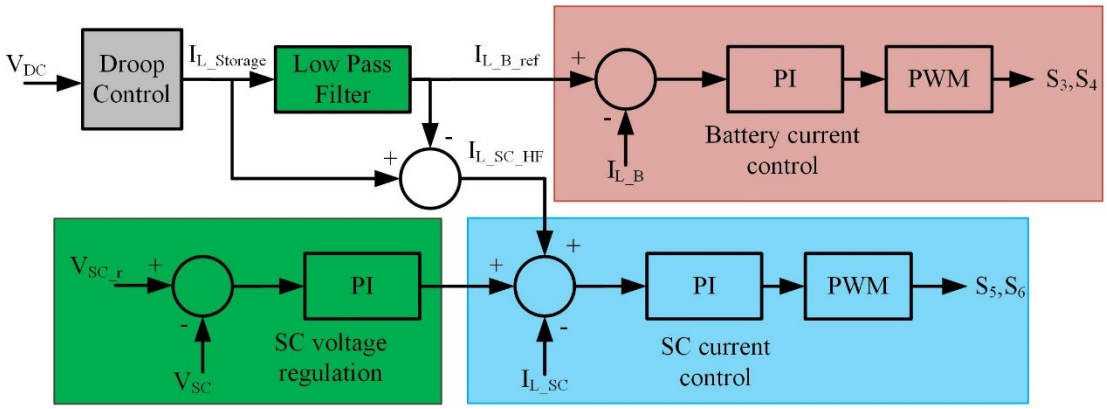

Figure 3. 3: Schematic diagram of the conventional control scheme of the co-located battery-SC HESS.

In the proposed approach shown in Figure 3. 4, the SC interface is controlled independently from the battery one, which will allow it to provide additional service to the DC nanogrid. This is achieved by selecting a droop factor for the SC interface much smaller than the battery's, what is equivalent to a higher gain for its outer DC bus voltage loop. As a result, it will provide a much larger current reference for a given DC bus voltage variation, what should improve the dynamic voltage regulation. Recall that the SC is inherently capable of providing/absorbing high bursts of

power. However, due to its low energy density, the duration of the power bursts should be limited, what can be done by introducing a HPF with suitable time constant in the input of its inner current loop. On the other hand, there is no need for a LPF in the input of the inner current loop of the battery interface, assuming that the SC interface will prevent sharp variations in the DC bus voltage and consequently sharp variations in the reference current of the battery interface.

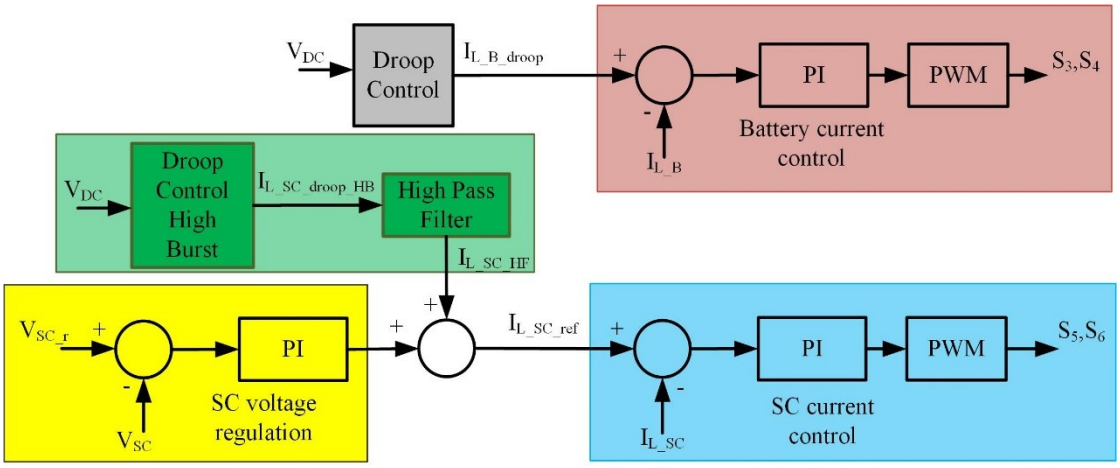

Figure 3. 4: Proposed battery-SC control diagram.

3.3.1 Design Approach for the Proposed SC Control Scheme

The proposed control scheme has two parameters for design: The droop factor (R_{dSC1}) and the time constant (τ_F) of the HPF. The first has a major impact on the peak value of the injected current, due to a sudden DC bus voltage variation, while both affect the duration of the high burst of power. Based on (3.2), the droop factor R_{dSC1} defines how much current is injected/absorbed into/from the DC grid as a function of a voltage difference (V_{NL} and V_{DC}). If the SC unit is to provide meaningful current bursts for assisting with dynamic voltage regulation, its droop factor should be much smaller, say 2% to 10%, than that of the battery converter. On the other hand, it is desirable that this current burst lasts just long enough to mitigate the DC bus voltage variations so as not to drain/supply much energy from/to the SC unit. This can be accomplished with the appropriate choice of the time constant (τ_F) of the HPF.

In order to select these parameters, a dynamic model of the system, including the small-signal model of the SC interface (class C DC-DC converter) as shown in Figure 3. 5, is considered. Assuming that the solar converter operates in the MPPT mode, it is modeled by a virtually constant current source. The battery converter operates with droop control and can be represented by a

Thévenin model with a voltage source equal to the threshold voltage and a resistor equal to the droop factor (R_{dB}) of the battery converter [64]. DC bus voltage variations shall occur mostly due to load variations.

Figure 3. 5 shows the small-signal model of the system, based on [43, 60]. It includes the inner boost inductor current (I_L) control loop with a PI-type controller and the duty-cycle to inductor current transfer function ($Gdi(s)$) of the converter. The outer (droop) voltage control loop is based on a droop factor (R_{dSC1}), that concerns the DC bus voltage (V_{dc}) and the reference injected current (I_{dc}). The slow SC voltage control loop is neglected in this analysis. A first-order high-pass filter (HPF) with time constant τ_F is used in this work, where

$$\tau_F = \frac{1}{2\pi f_c} \tag{3.3}$$

The power converter is assumed to be ideal and a gain factor (1-D) is employed to refer quantities from the DC bus to the SC side of the power converter, and vice-versa. A time constant for the DC nanogrid side (τ_S) is defined from the droop factor of the battery converter (R_{dB}), which is much lower than the equivalent load resistance (R_L), and the output capacitance of the SC interface (C_{DC3}). Thus,

$$\tau_S = C_{DC3} R_{dB} \tag{3.4}$$

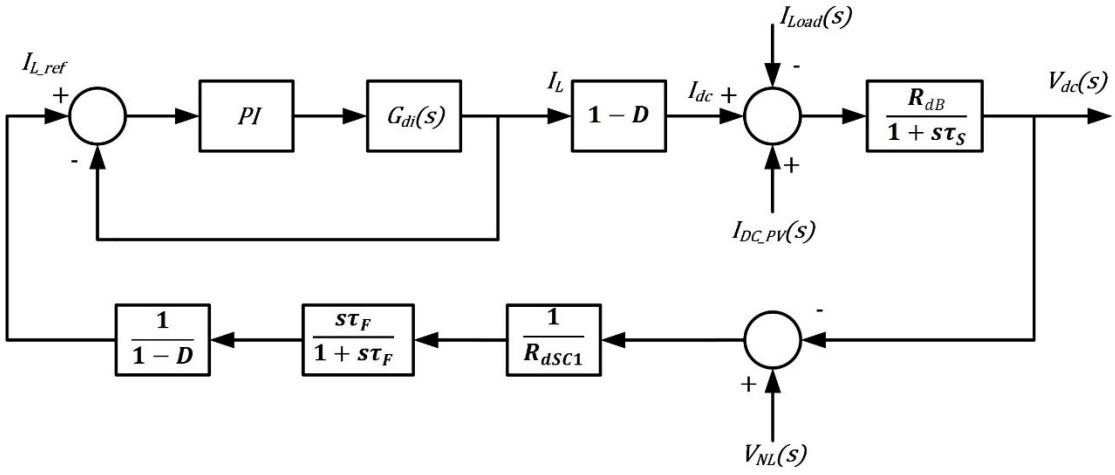

Figure 3. 5: Small-signal model for the analysis of the proposed SC control scheme.

Since the outer voltage (droop) loop has a much lower bandwidth than the inner current loop, the latter, which presents a zero error in steady-state due to the PI controller, can be simplified to a unity gain. Then, one can assume that there will be no variations in V_{NL_SC} and that load and

PV current variations can be combined in a single element (I_Δ). Finally, the block diagram describing the dynamics of the system can be further simplified as shown in Figure 3. 6.

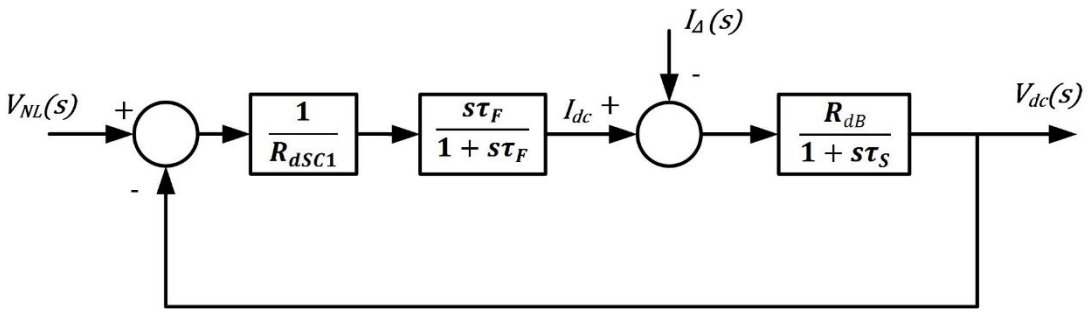

Figure 3. 6: Simplified small-signal model for the analysis of the proposed SC control scheme.

The system's transfer function (G_T) is given by:

$$G_T(s) = \frac{V_{dc}(s)}{I_\Delta(s)} = \frac{kG(s)}{1 + kG(s)H(s)} \tag{3.5}$$

where;

$$G(s)H(s) = \frac{s\tau_F R_{dB}}{(1 + s\tau_F)(1 + s\tau_S)} \tag{3.6}$$

and

$$k = \frac{1}{R_{dSC1}} \tag{3.7}$$

The characteristic equation of the system is:

$$\Delta = s^2 + s\frac{(\tau_F R_{dB} + \tau_S R_{dSC1} + \tau_F R_{dSC1})}{(\tau_F \tau_S R_{dSC1})} + \frac{1}{(\tau_F \tau_S)} \tag{3.8}$$

It can be represented in terms of the damping ratio (ζ) and the natural frequency (ω_n) as:

$$\Delta = s^2 + 2\zeta\omega_n s + \omega_n^2 \tag{3.9}$$

where;

$$\omega_n = \frac{1}{\sqrt{\tau_F \tau_S}} \tag{3.10}$$

and

$$\zeta = \frac{1}{2}\frac{(\tau_F(R_{dB} + R_{dSC1}) + \tau_S R_{dSC1})}{R_{dSC1}\sqrt{\tau_F \tau_S}} \tag{3.11}$$

The impact of the value of the droop factor (R_{dSC1}) and time constant (τ_F) of the HPF on the dynamic response of the system can be observed by means of the root locus method. The latter determines the location of one of the open loop roots while the former affects the position of the closed loop roots. Figure 3. 7 shows the root locus of the system for R_{dB} = 0.289Ω and C_{DC3} = 1500 μF. For the analysis, the cut-off frequency of the HPF is taken as 43.5 Hz. Since transfer function *GH*, (3.6), has two negative real poles and one zero at the origin, the system is stable at any gain *k*. As *k* increases (R_{dSC1} decreases), one closed loop real root moves towards the infinity and the other, dominant, towards the vertical axis. For a high enough *k*, one can neglect the non-dominant root.

As mentioned before, small values for R_{dSC1}, from 2% to 10% of R_{dB}, should lead to a large enough burst of current to assist with dynamic DC bus voltage regulation what should also prevent the battery from supplying fast changing currents. Once the value of R_{dSC1} is selected, one can compute τ_F based on the desired duration of the high burst of power (T_s). For a system (G_T) with a dominant real root, one can say that $T_s = 3\tau$, where τ is the time constant of the dominant root. For a system with a neglectable root, $\zeta \gg 1$ and

$$\tau = \frac{1}{(\zeta - \sqrt{\zeta^2 - 1})\omega_n} \tag{3.12}$$

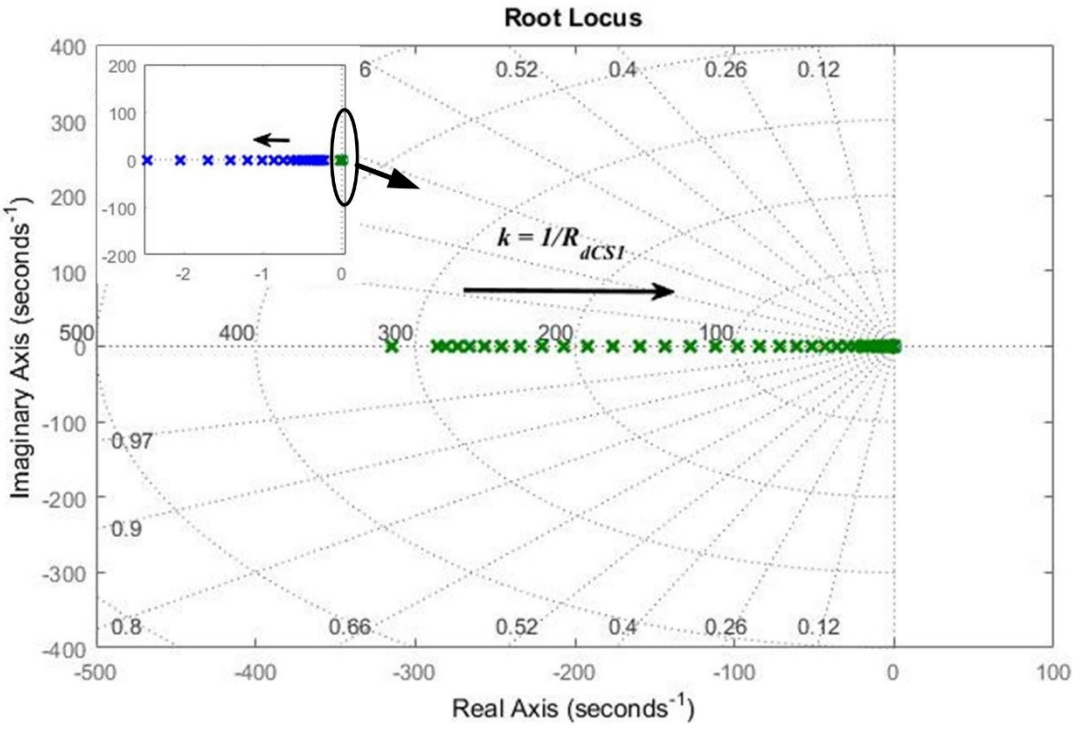

Figure 3. 7: Root locus for varying the value of R_{dSC1} with $\tau_F = 3.18\,ms$.

Then, for a specific desired time constant τ, one can solve (3.12) with ω_n from (3.10) and ζ from (3.11) to find τ_F. A closed form equation for τ_F is not straightforward. Alternatively, one can obtain the value of τ_F from a plot. Figure 3. 8 shows the value of 1/ τ as a function of τ_F for different values of R_{dSC1}/ R_{dB} and for a system with C_{DC3} = 1500μF. As an example of usage of this approach, for R_{dSC1} = 0.05R_{dB}, a HPF with $\tau_F = 3.7$ms gives the settling time T_s = 0.22s. For R_{dSC1} = 0.1R_{dB}, and the same HPF ($\tau_F = 3.7$ms), the settling time becomes T_s = 0.12s. Alternatively, the original settling time (0.22s) can be achieved with R_{dSC1} = 0.1R_{dB} and a HPF with a time constant of $\tau_F = 6.9$ms. It should be noted that as one decreases R_{dSC1}, to have a higher burst of current and a smoother DC bus voltage variation following a sudden power unbalance in the DC nanogrid, a smaller time constant (τ_F) of HPF is needed for a given settling time. In addition, Figure 3. 8 also shows the impact of τ_F on the damping ratio ζ and the natural frequency ω_n.

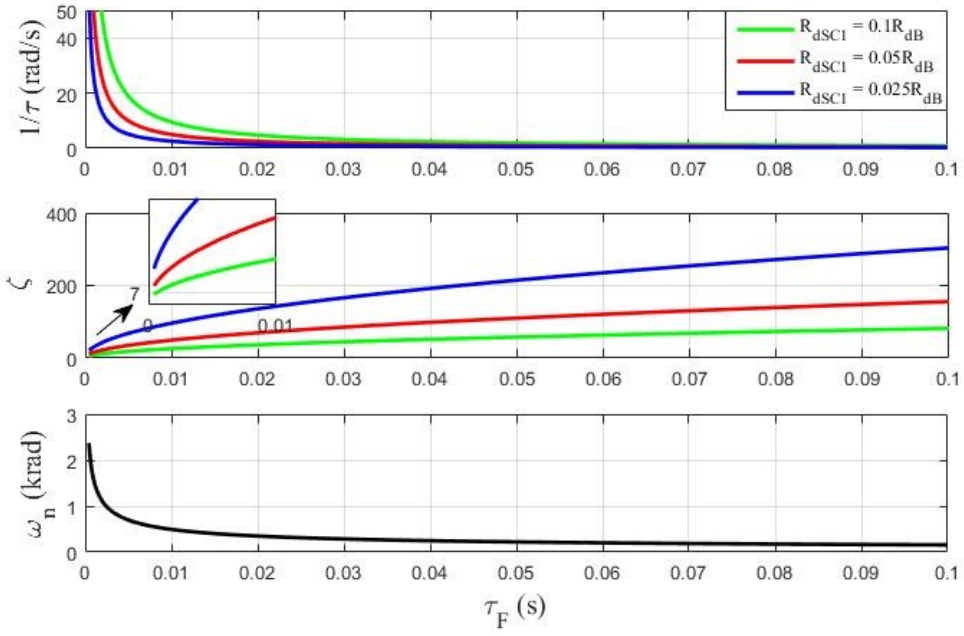

Figure 3. 8: The relationship between 1/ τ and τ_F for different droop factors of the SC unit (R_{dSC1}).

3.4 Case Study

As a case study in this chapter, a 48V DC nanogrid consisting of a PV-based RES, a battery unit, a SC unit and a variable load is considered. The PV panel provides a maximum power of 213W with 7.35A and 29V at rated solar irradiance. Due to converter losses, it is considered that the maximum (rated) injected power by the PV unit is 200W. In order to comply with the voltage levels presented in Section 3.2, the DC bus voltage should vary between 49.2V and 45.6V in the MPPT region, where the solar converter would inject 4.1A and 4.4A, respectively.

In the performance investigation to be conducted in the following Sections, the conventional control scheme for the HESS will be compared to the proposed one, which can also be used for non-co-located battery and SC units. The droop factor of the HESS (R_{d_ST}) is 0.289Ω and the cut-off frequency of the LPF for the frequency split is 43.5Hz. The HESS' threshold voltage (V_{NL_ST}) is 48V and the current limit value is the maximum current supplied by the PV converter (($I_{ST\text{-}c}$ = $I_{PV\text{-}c}$ = 4.4A). Concerning the proposed scheme, the threshold voltages of the battery and SC converters, V_{NL_B} and V_{NL_SC}, are equal to V_{NL_ST} and their rated currents are equal to the maximum current supplied by the PV converter ($I_{B\text{-}c}$ = $I_{PV\text{-}c}$ = 4.4A). The droop factor of the battery converter is R_{dB} = R_{d_ST} = 0.289Ω, while that of the SC, which as discussed in Section 3 should be 20 times lower than the battery's, is R_{dSC1} = 0.0145Ω. The cut-off frequency of the HPF

for the proposed SC control loop was calculated as described in Section 3.3 for T_s = 0.22s and is equal to 43.5Hz.

Regarding the power electronic interfaces, the DC-DC converters of all elements are very similar, with the exception of the unidirectional feature of the RES. They are realized with a single three-phase DC-AC converter as shown in Figure 3. 9, for simulation studies and in the experimental set-up. The capacitor of the DC bus (nanogrid) voltage is equal to 1500µF. LC filters (100µH and 470µF) are connected between the mid-points of the three-phase inverter legs and the storage and the source elements, to create the classical class C DC-DC converters. The converters operate with PWM and a switching frequency of 20kHz.

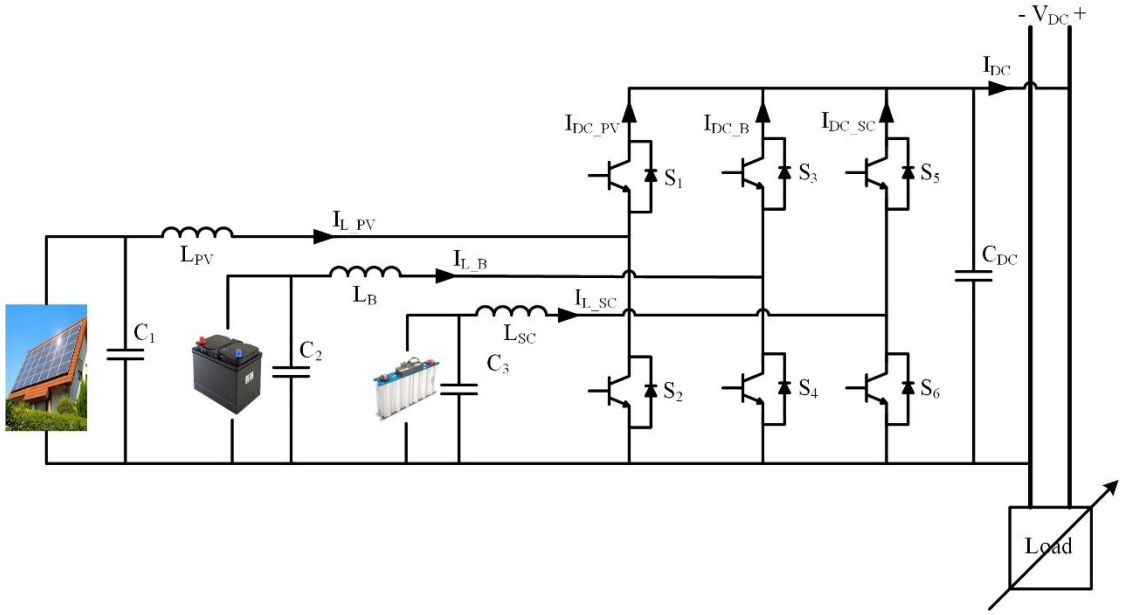

Figure 3. 9: DC nanogrid power electronics interfaces.

The same current control loop can be used for all DERs. A PI type-III controller was designed for the same equivalent plant with a transfer function shown in (3.13) [43, 60]. They were designed for a crossover frequency of f_x = 2 kHz (10% of the switching frequency) and phase margin of PM = 80°. The following plant parameters were assumed: V_{DC} = 48V, I_{DC} = 4.44A, R = 10.8Ω, L = 100µH, C = 1500µF, and D = 0.46 for V_{PV} = V_{Bat} = V_{SC} = 29V. R was selected as the maximum load that could be supplied by the RES alone. At the end, the PI controller parameters are computed as K_{PI} = 0.0114, τ = 171µs and T_P = 37µs.

$$G_{di}(s) = \frac{\tilde{\imath}_L(s)}{\tilde{d}(s)} = \frac{CV_{DC}s + 2I_{DC}}{LCs^2 + \frac{L}{R}s + (1-D)^2} \tag{3.13}$$

3.5 Simulation Results

MATLAB/Simulink is used for simulation studies. The objective is to investigate the potential benefits of an independently controlled SC unit in the dynamic regulation of the DC nanogrid voltage. Ideally, this should not affect the ability of the SC unit to mitigate the high frequency and fast changing currents in the battery. In order to test this feature, the solar converter operates in MPPT while the power demanded from the DC nanogrid varies between no-load and full-load. From t = 0s to 0.05s there is no power demanded from the DC nanogrid, and the storage unit(s) absorbs all the power provided by the RES, about 200W. Then a full-load impedance of 5.2Ω is connected to the DC nanogrid to be supplied by both the RES and storage unit(s), both at full power. This operating condition remains until 0.05s when the load is removed. This corresponds to the largest normal disturbance to be faced by the DC nanogrid and will be used to compare the performance of the proposed control scheme with the conventional one with a HESS. The parameters of the system are as stated in previous Sections. (The battery and SC were represented by ideal DC voltage sources of 24V and 28.4V, respectively.)

Figure 3. 10 shows the results of the key system waveforms for the conventional scheme. Initially at no-load, the DC nanogrid voltage (top screen) is about 49.25V. The solar converter operates in the MPPT mode with a boost inductor current (average) of around 7.35A, bottom screen. The average current absorbed (negative sign) by the battery is 8.4A while of the SC is zero, as expected. Following the load step, the SC current increases very fast reaching a peak value of 10A, while the battery's increases more slowly, as desired, until it supplies all the HESS current. The DC bus voltage reaches the steady-state value of 46.75V in 17ms. A similar behavior, in terms of current magnitudes and settling times, can be observed when the load is removed at t = 0.3s and the HESS has to, again, absorb rated power.

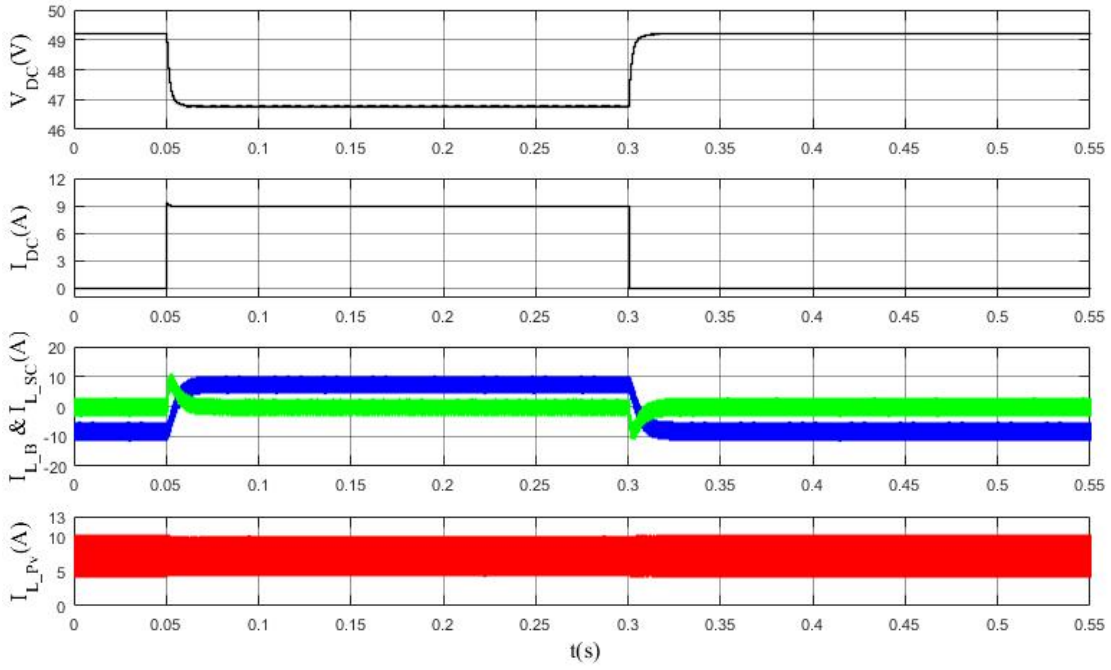

Figure 3. 10: Simulation results for the conventional approach when the load changed from no-load to 5.2Ω (full nanogrid load) and back to no-load.

Figure 3. 11 shows the performance of the system, for the same load transients, with the proposed control scheme. The values of the waveforms in the steady-state for the no-load condition are virtually the same as for the conventional HESS control scheme. Following the full-load step variation, one can see that the DC bus voltage decreases much more slowly than with the conventional HESS control approach. This is due to the way the SC converter was controlled, injecting a higher current and for a longer time to slow down the reduction in the DC bus voltage. At the same time, as expected, it slowed down the increase of the battery current. This was done indirectly, via the DC bus voltage, without any signals exchanged between the control loops of the battery and SC converters. Just before t = 0.3s, the values of the waveforms obtained with the proposed scheme are very similar to those obtained with the conventional HESS scheme. Then following a step load rejection, to no-load, the proposed scheme provides a similar improvement in the DC bus voltage variation and in the battery current variation. It is worth mentioning that besides using the proposed control scheme, one should also make sure that the SC is large enough to provide/absorb the required compensating energy without significant changes in its voltage level and that the boost inductor of the SC converter will not saturate with the increased current. Considering the relatively short action time of the proposed control scheme for the SC converter, it should not be necessary to increase the current ratings of the semiconductor switches.

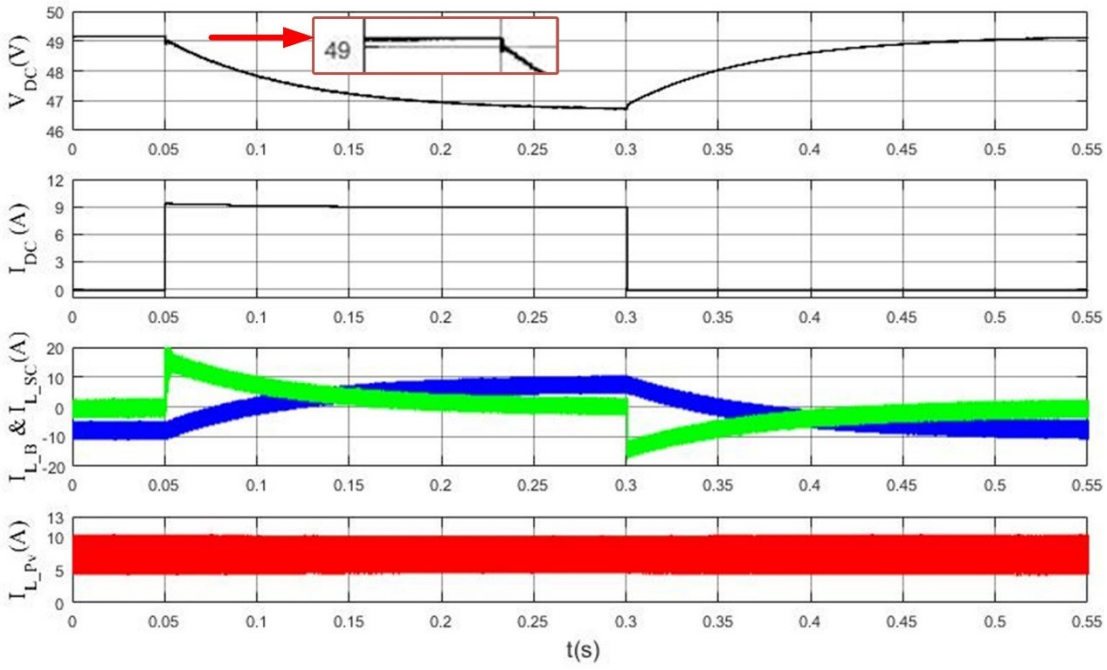

Figure 3. 11: Simulation results for the proposed approach when the load is changed from no-load to 5.2Ω (full nanogrid load) and back to no-load.

3.6 Experimental Results

A DC nanogrid with a RES, two energy storage units and a variable load was assembled in the laboratory. An Agilent Solar Array Simulator (SAS) (E4350B) was used to emulate a solar array. It was programmed to provide a maximum power of 213W with 7.35A and 29V at rated solar irradiance. Maxwell supercapacitor modules (BMOD0165 P048) of 165F with a rated voltage of 48V were employed for the energy storage units. One is used as a battery and the second is used as a SC. As in the simulation studies, the "battery voltage" was adjusted to 24V and the SC's to 28.4V. Regarding the power electronics interface, a Semikron "MiniSKiiP 8 Three-phase 1200V Power board", with a *MiniSKiiP 83 AC* power module and a *SKHI61* IGBT driver, was used in this study. The values of passive components, control parameters and so on used in the experimental set-up are those presented in Section 3.4. The control schemes are implemented with a dSPACE DS-1103 rapid prototyping system with a 20μs time step. The dSPACE code generated by Simulink C coder with extinction of Real-time interface (RTI). That converter the control diagram from MATLAB/Simulink into dSPACE code. This does not provide the fastest and the shortest code, but it is sufficient in experimentally proof-of-concepts. Eight parallel switchable 44

Ω resistors were used for realizing the full DC nanogrid load impedance. A picture of the experimental set-up is shown in Figure 3. 12.

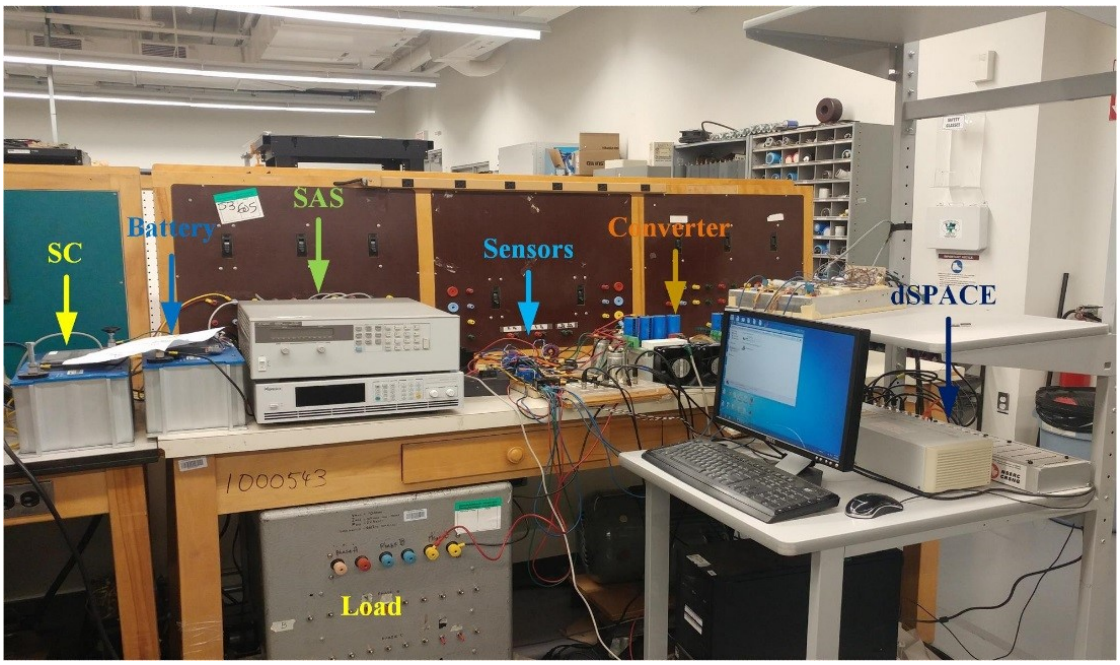

Figure 3. 12: Picture of the experimental set-up assembled in the laboratory.

Having demonstrated the improved performance of the proposed scheme over the conventional HESS control scheme by means of simulations, experimental results are provided to demonstrate the feasibility of the proposed control scheme. The focus of this Section is on the impact of different system parameters obtained using the proposed design approach.

The first case, which was also presented in the simulation studies, concerns a SC interface with a droop factor R_{dSC1} = 0.0145, 20 times lower than the battery's for providing a peak current of 20 times that of the battery for a given DC bus voltage variation. It employs a HPF with a time constant $\tau_F = 3.7\text{ms}$, computed to give a settling time of T_s = 0.22s. The key waveforms of the system are shown in Figure 3. 13 for a no-load to full-load (5.2Ω) variation and back to no-load. At no-load, the DC bus voltage is initially at 49.2V and it decreases slowly to 46.8V at full-load in the steady-state. (The screen shows 0.4V/div.) The load current increases in a step-like manner from 0A reaching 8.45A in steady-state (1.3A/div). The SC (inductor) current, initially at 0A, increases very fast following the load step reaching a peak value of about 20A. Then, it decreases exponentially reaching 0A after about 0.24s. The battery (inductor) current changes slowly from -8A, when it absorbs the full PV power at no-load, to 8A, when it provides to the DC bus the same

amount of power of the PV converter, at full-load (4A/div). The PV (inductor) current remains virtually constant at since it operates with MPPT with rated solar irradiance. The experimental waveforms match very well with the simulation ones.

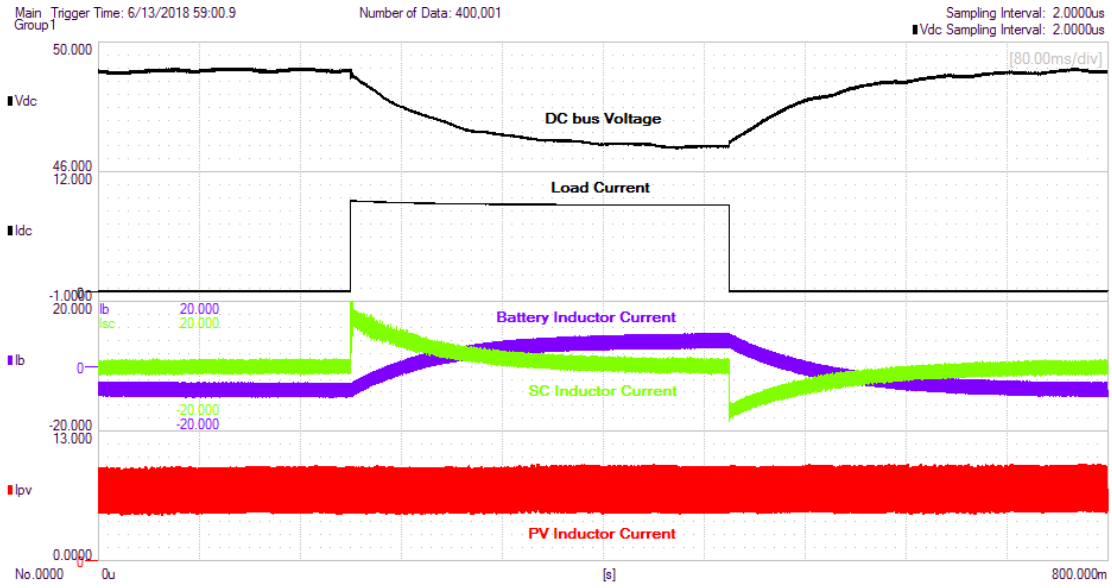

Figure 3. 13: Experimental result for the proposed control scheme with R_{dSC1} = 0.05 R_{dB} and designed for T_s = 0.22s, as the load changed from no-load to full-load (5.2Ω) and back to no-load.

In the second case, a larger droop factor (R_{dSC1} = 0.0289Ω), which is 10% of the battery's, is used. Thus, the SC converter should provide a lower contribution during transient conditions. The time constant of the HPF is calculated for the same (T_s = 0.22s) resulting in τ_F = 6.9ms. Figure 3. 14 shows the transient response of the system, with the above mentioned parameters, for the no-load to full-load and back to no-load transitions. By comparing the results with the previous ones, one sees that the DC bus voltage presented a larger step decrease, due a lower peak SC (inductor) current, but it reaches the same steady-state value at full-load with the same delay as before, because of the design specification (settling time) used in both cases. The battery (inductor) current increased a bit faster as a result of the lower DC bus voltage during the transient condition. The PV (inductor) current remains virtually the same, identical to the previous case.

The last case concerns a SC converter with a large droop factor (R_{dSC1} = 0.0289Ω = 0.1 R_{dB}), and with a HPF designed for a settling time (T_s = 0.12s) resulting in τ_F = 3.7ms. In such a case, the SC converter should present the lowest, in terms of current magnitude, and shorter contribution during the transient conditions of the three cases tested experimentally. As observed in Figure 3. 15, its impact on the dynamic DC bus voltage regulation and battery (inductor) current

waveform is obviously lower. However, this can be achieved with a lower energy required from the SC and potentially a smaller (capacitance) SC, for the same SC voltage variation.

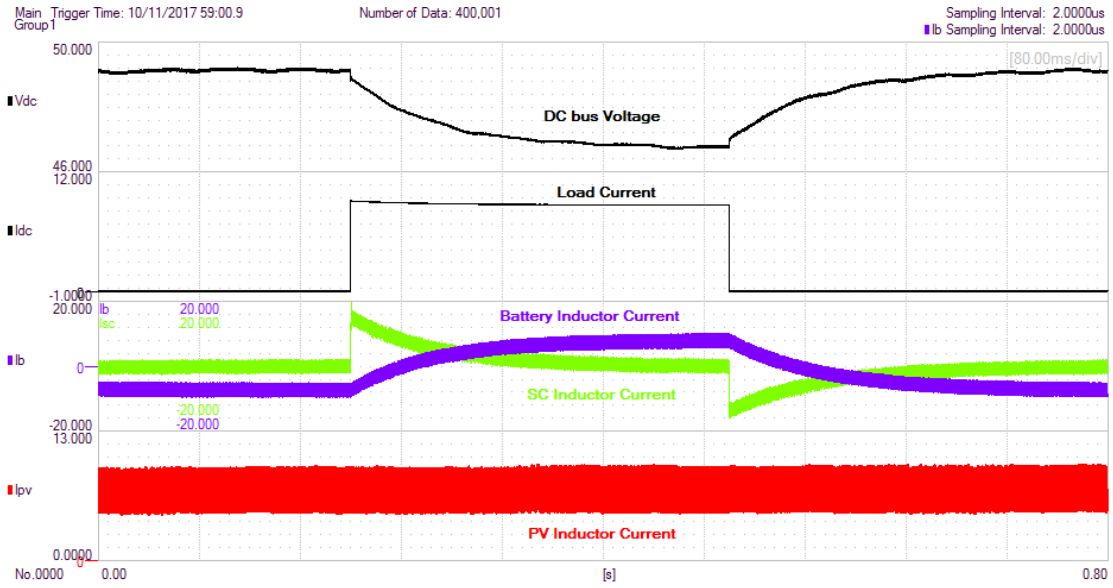

Figure 3. 14: Experimental result for the proposed control scheme with R_{dSC1} = 0.1 R_{dB} and designed for T_s = 0.22s, as the load changed from no-load to full-load (5.2Ω) and back to no-load.

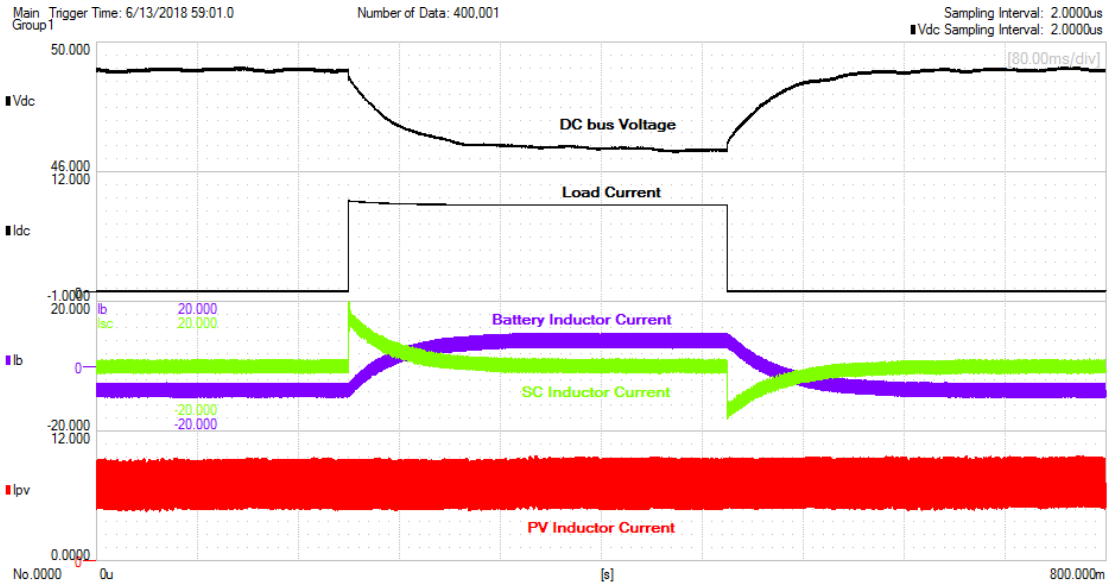

Figure 3. 15: Experimental result for the proposed control scheme with R_{dSC1} = 0.1 R_{dB} and designed for T_s = 0.12s, as the load changed from no-load to full-load (5.2Ω) and back to no-load.

3.7 Conclusions

Hybrid energy storage systems (HESSs) with battery and supercapacitors (SCs) can play an important role in autonomous DC nanogrids with stochastic renewable energy sources (RESs)

and highly variable loads. Battery and SCs are usually co-located and, in droop-controlled DC grids, controlled with a single V-I curve. The appropriate current contributions of battery, slow components, and SC, fast components, are obtained with low-pass or high-pass filters (HPFs). Since the droop slope of the HESS is determined based on steady-state conditions, it is relatively large, preventing the HESS from providing high and fast varying currents for effective dynamic DC bus voltage regulation. This chapter proposes the independent control of battery and SC units, which can be co-located or not. The battery control scheme remains focused on steady-state conditions while one assigns a small droop slope to the SC unit for it to respond strongly to minor DC bus voltage variations. In order to prevent the SC from supplying/absorbing large amounts of energy, a HPF is included in its control loop. A design approach was presented and the performance of the proposed scheme was validated by means of simulation and experimental results. It allows the SC unit to improve the dynamic voltage regulation of the DC nanogrid while, indirectly, mitigating the high and fast current variations in the battery unit.

CHAPTER FOUR: A DROOP-CONTROLLED INTER-LINK CONVERTER FOR A DUAL DC BUS NANOGRID

4.1 Introduction

The integration of renewable energy sources (RESs) at the distribution levels is a promising alternative for reducing the environmental impact of conventional fossil fuel based sources and the need for building new transmission lines to bring power from large plants located far away from consumer centers. However, the stochastic nature of RESs and their variable power generation can lead to power quality issues in the distribution system. One way around this is to associate them with energy storage units and controllable loads, which could be controlled as a cluster, or as a "microgrid." For that, one needs detailed information about the state and operating conditions to be sent timely to the grid interfaces of generation and storage units, which need to be fast acting and reliable. This is achieved with sophisticated information and communication technology (ICT) and modern power electronic converters [1-3]. In general, the study of microgrids has been focused on distribution feeders and neighborhoods with medium size power plants, 100's of kW [4]. The microgrids concept enables the distributed energy resources (DERs), that include power sources, energy storage units and controllable loads, to operate in islanding mode following a power grid failure [2, 4, 5]. This is done by dynamically decoupling the microgrids from the utility grid using a full-power bidirectional converter. This grid tie or interface converter can be used as energy control center [5]. This concept can be extended for smaller units, 10's of kW, for a residence. The future smart homes are envisioned to be net-zero energy homes (NZEH). These are homes with net zero energy consumption, meaning that the total amount of energy used by them on an annual basis is nearly equal to the amount of energy produced by them, ideally with RESs [6]. To be able to operate autonomously, at least for some time, they should present not only generation as well as storage units and controllable loads, which with a suitable control structure, can be seen as a "nanogrid." Nanogrids can be based on AC or DC distribution [5, 7].

In order to connect RESs, plug-in hybrid electric vehicles and storage units to an AC nanogrid, power electronics converters of the DC to AC type are used. For power sources such as PV and wind turbines, unidirectional power electronic converters are employed. In the case of PV, the required DC-AC converter usually consists of two stages: A step-up (boost) DC-DC converter

and a single or three-phase DC-AC converter [5]. Two stage converters, but now bidirectional, are employed to connect energy storage units, usually batteries, to an AC nanogrid [8]. In AC nanogrids, the DC-AC converter are responsible for voltage and frequency regulation of the AC bus in islanding (stand-alone) mode and grid connecting mode [9, 10]. For distributed energy sources, energy storage units and controllable loads in a nanogrid, a DC bus leads to the simplest interconnection scheme [5, 11].When compared to the AC distribution; the DC distribution does not require frequency or phase control. In addition, DC-DC interfaces have higher efficiency and higher reliability [5, 11-14]. Furthermore, DC has lower distribution losses, lower cost of conductors for the same power and does not use bulky transformers leading to cost and volume reduction [5, 11, 15]. Besides that, a DC nanogrid should employ a DC-AC converter, to serve as the interface to a conventional AC distribution feeder/neighborhood. It should offer the desirable capability of dynamically decoupling the DC nanogrid from the AC utility grid. Therefore, the future residential electrical system of a NZEH could very well be based on DC distribution [5].

One key aspect that remains unclear is the voltage level that should be adopted. According to the IEC, Extra Low Voltage (ELV) DC presents a magnitude of less than 120 V and lower risk of electrical shock. However, for supplying kW loads, relatively high currents are required, leading to high distribution losses and/or conductors. The 48V DC is a standard telecom voltage level [5, 16, 17]. The following, higher voltage, category is the Low Voltage (LV), with magnitudes between 120 V and 1500V. Higher voltages lead to lower currents, for a given power demand, but this might complicate the design of the DC protection system as well as require the use of power interfaces with large voltage gains. The 380V DC level matches with the industry-standard intermediate DC voltage [5, 18]. One option that has been considered and proposed by industry associations is the use of two voltage levels (buses). The Emerge Alliance [19, 20] advocates the use of a 24 V, mostly to comply with current LED technology for lighting, and a 380 V for other loads. However, in order to be able to supply “other small loads”, the use of a 48 V, which is also being considered for mild-hybrid vehicles, will be selected.

It should be noted that in the Emerge Alliance scheme, power sources and storage units are connected to the 380 V bus and a step-down unidirectional DC-DC converter is used to supply the 24 V lighting bus. One issue of concern is the reliability of the 24 V, which will be de-energized if either the 24V bus interface fails or the 380V bus is not operational. The dual DC bus nanogrid

considered in this research work presents power sources and energy storage units in both DC buses and a bidirectional “interlink” converter/interface to allow power flow from one bus to the other, and indirectly, from the 48V bus to the AC utility grid, assuming that a 380V DC to AC grid interface is present and operational. A simplified Dual DC buses nanogrid is shown in Figure 4. 1. There one can see that the RESs (solar energy) and electrical storage systems (batteries) are connected to both DC buses. The first can employ a unidirectional converter but the second requires a bidirectional one. The utility grid is connected to the HV DC bus via a bidirectional DC-AC converter. A bidirectional inter-link converter allows the power flow between the two DC Buses.

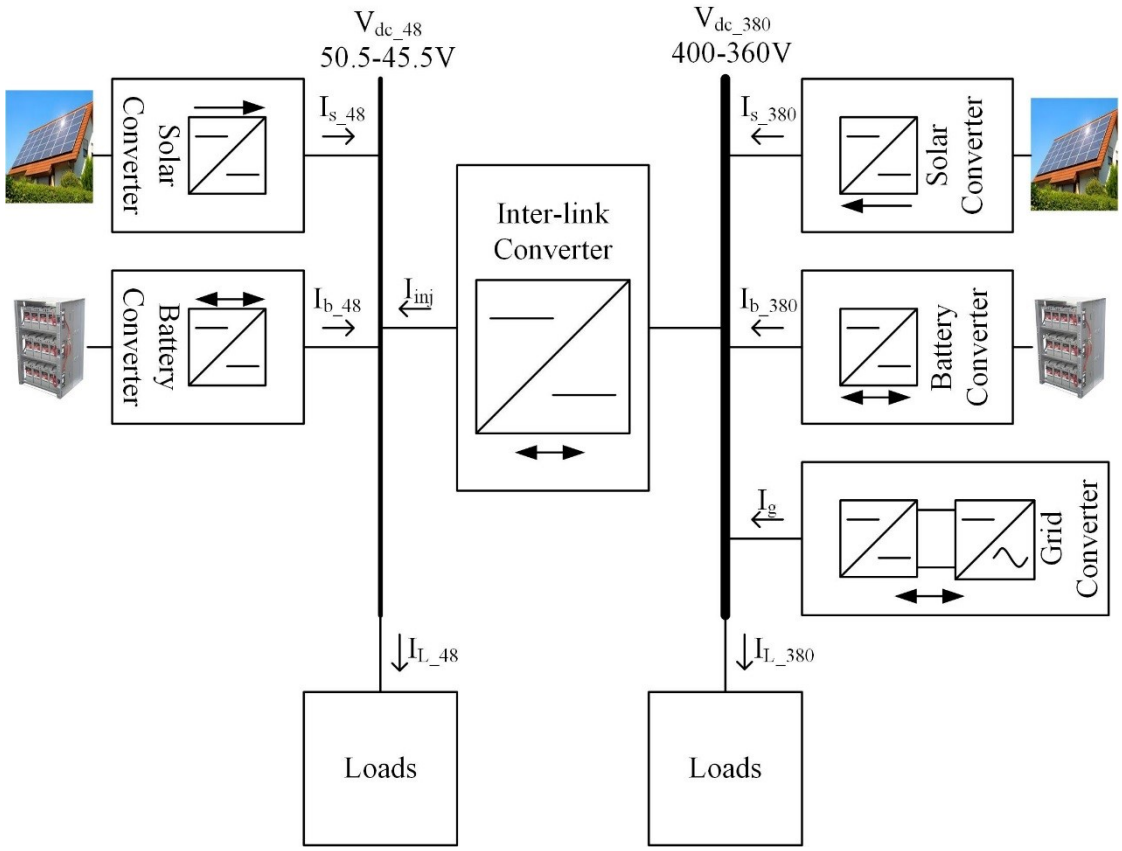

Figure 4. 1: Dual DC Bus Nanogrid.

In terms of research and development of the interlink converter, one should select a suitable power topology with rated voltages of 48V:380V, a modulation/control scheme as well as define an appropriate control strategy (V vs. I curve) for the interlink converter to operate with DC bus signaling (DBS). The latter should be done in a way not to interfere with the conventional approach

of managing power and energy in single bus DC nanogrids. It should be noted that although 48V and 380V, as stated before are ELV and LV, they would be called, “LV side” and “HV side” respectively, in this work.

4.2 Power Control and Current Sharing in a Single DC Bus Nanogrid

A conventional single-bus DC nanogrid can be controlled in a decentralized way with a hierarchical structure with DC bus signaling (DBS) and droop control used at the primary level [5, 21, 22]. The secondary and tertiary levels, which require a communication means for energy management, are not considered in this work. Thus, with fixed parameters for the primary control level, the DC bus voltage will vary in a small range around the rated voltage, as defined by the V vs. I curves of the DERs. DBS uses the DC bus voltage itself as the communication link to coordinate the operation of DERs in a decentralized way. With droop control, the current (power) injected by each DER in the DC nanogrid depends on its threshold voltage (V_{NL}), where the injected current is zero, and its droop slope/factor (R_d) as shown in (4.1). The latter determines how the injected current varies as a function of grid voltage variations.

$$I_{DC} = (V_{NL} - V_{DC})\frac{1}{R_d} \tag{4.1}$$

Where;

$$R_d = \frac{\Delta V_{DC}}{\Delta I_{DC}} \tag{4.2}$$

Figure 4.2 shows the V vs. I curves of the usual components found in a DC nanogrid with proposed set of parameters [5]. The DC-AC grid converter is discussed first. When the DC bus voltage is between 390V and 370V, the converter operates in droop mode with droop constant (slope) R_{dg}. Otherwise, it operates in current limiting mode, with the DC-AC converter absorbing rated current for $V_{DC} > 390$ V and supplying for $V_{DC} < 370$ V. Its threshold, or no-load, voltage is the rated voltage of the DC bus: 380V. That is to say that at this voltage, the current and power flowing through the converter is zero. The values of the threshold voltage and the DC bus voltage determine the power flow direction. When the DC bus voltages is higher than 380V but lower than 390V, power flows from the DC nanogrid into the AC utility grid ($I_g < 0$A). Conversely, for DC bus voltages is lower than 380V but higher than 370V, power flows to the DC nanogrid from

the AC utility grid (I_g > 0A). The threshold voltage is the main control parameter of this DC-AC converter, which can be adjusted by the secondary control level.

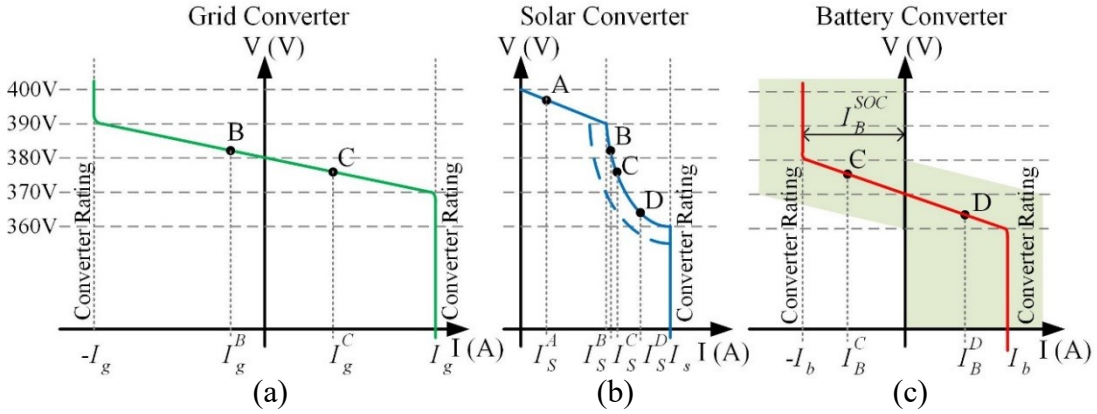

Figure 4. 2: V vs. I curves of the high voltage DC bus DERs: (a) Grid Converter, (b) Solar Converter, and (c) Battery Converter.

In the case of the RESs, such as the solar converter, the V. vs. I curve usually presents three regions: droop, constant power, and constant current as shown in Figure 4.2 (b). It operates with droop constant R_{ds} for a DC bus voltage between 400V (threshold voltage) and 390V, when the converter starts to operates in the maximum power point tracking (MPPT) mode with the maximum available power injection. In the concept of DC bus signaling, a higher threshold voltage for the solar converter, than the grid converter's, gives the RESs a higher priority to feed the DC nanogrid demand/load when operating in parallel. The actual flow of power between solar converter, grid converter, battery and variable load will be discussed in a following section. For DC bus voltages between 390V and 360V, the converter operates in the maximum power point tracking (MPPT) mode injecting virtually constant power, for constant solar irradiance (W/m^2). The dashed line in this region shows that the solar converter is reprogramed to operate in MPPT mode injecting the maximum available power, when the solar irradiance decreases from the rated value or the PV panel temperature increases [5]. When the DC bus voltage further drops below 360V, the solar converter operates at the current limiting mode.

For the electrical storage units, it operates in the droop mode, with droop constant R_{db} when the DC bus voltage is between 380V and 360V. Otherwise, it operates in the current limiting mode, absorbing rated current for V_{DC} > 380 V and supplying for V_{DC} < 360 V. The storage system usually has the third priority, after the RESs and the utility grid to feed the load. It has a threshold voltage of 370V, lower than the other system interfaces. This prevents the electrical storage system

from discharging through the utility grid. On the other hand, the electrical storage system is discharged at DC bus voltages less than 370V.

Concerning power flow control and energy management in the DC nanogrid, the actual value of the threshold voltage of the power interfaces can be adjusted, based on the instantaneous and historical price of energy, that could be drawn from or supplied to the utility grid. Long and/or short-term histories of the local renewable energy generation and the nanogrid load profiles play a role in reprograming the threshold voltage. In addition, the history of the state of charge (SoC) of the storage units should be taken into account. To achieve optimal threshold voltage preprogramming, an *optimal energy utilization algorithm* is used [5]. To implement this algorithm, historical data about the system is needed. The maximum current of charging and discharging is based on the battery manufacturer and power converter ratings. In some cases, when the SoC drops below 20%, the control will stop the discharging operation mode. On the other hand, the battery will not be charged when it has a SoC greater than 90% [23]. The current limits could be a function of the state of charge (SoC) [5, 24-26]. This produces the shaded area in the V vs. I curve in shown in Figure 4.2 (c).

Neglecting the voltage drops between the DER interfaces and the equivalent system load, the DC bus voltage (V_{DC}) of a nanogrid operating with DBS and multiple DERs can be determined from:

$$I_{Load} = \sum_{i=1}^{n} I_{DC\_i} \tag{4.3}$$

Where I_{DC_i} are computed according to the V vs. I curves of the n DERs. With the value of V_{DC}, one can then calculate the individual contributions of the DERs from their V vs. I curves.

4.3 Power Control of the Inter-Link Converter

As a conventional single-bus DC nanogrid, the dual DC buses nanogrid could be controlled in a decentralized way with a hierarchical structure based on droop control and DC bus signaling [5, 21, 22]. In principle, the V vs. I curves and parameters of the DERs in the LV DC bus and HV DC bus could be the same as in the case of a single-bus DC nanogrid. For instance, it is assumed that the values of threshold voltages, droop slopes, and current limits for the DERs in the LV bus are proportional to those of the HV side, shown in Fig. 4.2. With the addition of the inter-link

converter, an opportunity for optimizing the operation of both buses, in terms of voltage regulation and management of power flow and energy management arises. For that, a suitable strategy for controlling the power flow of the inter-link converter is needed. Ideally, it should be based on DBS, taking into consideration the voltages of both DC buses, which reflect the availability of power in those buses. Considering that the batteries are sort of the weak link in the system, since they are not supposed be over or under-charged, it is important that the control law of the interlink converter does not place unnecessary stress on them. Besides, in terms of managing the system to operate with high efficiency, having the battery of one bus charging the battery of the other, should be avoided.

Two control strategies for the inter-link converter in a dual DC bus nanogrid, average droop control and constant voltage ratio were presented in [27]. The first determines the power flow between the two buses based on the average value obtained from droop curves of the LV and HV sides. On the other hand, the second employs a PI controller to keep the per-unit voltage ratio constant between the two buses, without a V vs. I curve. Those control strategies can be used for a dual DC bus nanogrid with similar participations of RESs and storage units but it should not be use when the Dual DC nanogrid has a connection with the AC utility grid.

One alternative approach to control the interlink converter is to use, in principle, the same V vs. I curve of the grid converter of the HV bus. Recall that this is controlled based only on the voltage of the HV DC bus, neglecting the voltage of the AC bus. This is reasonable since the latter is assumed to be much stronger, with more power availability, than the former and being able to supply/absorb the matching power for/from the HV DC bus. By making the control of the interlink converter be based on the voltage of the LV bus only, one does not compromise the ability of the HV bus to operate without stressing its storage units since the grid converter is there to provide/absorb the required matching power.

Therefore, one can use the V vs. I curves shown in Figure 4.3 for the interfaces of the LV DC bus. Note that the voltage levels, in terms of pu, are comparable to those employed in the HV DC bus. The voltage range in the normal operating conditions varies by about 5% above and below the rated voltage (48V).

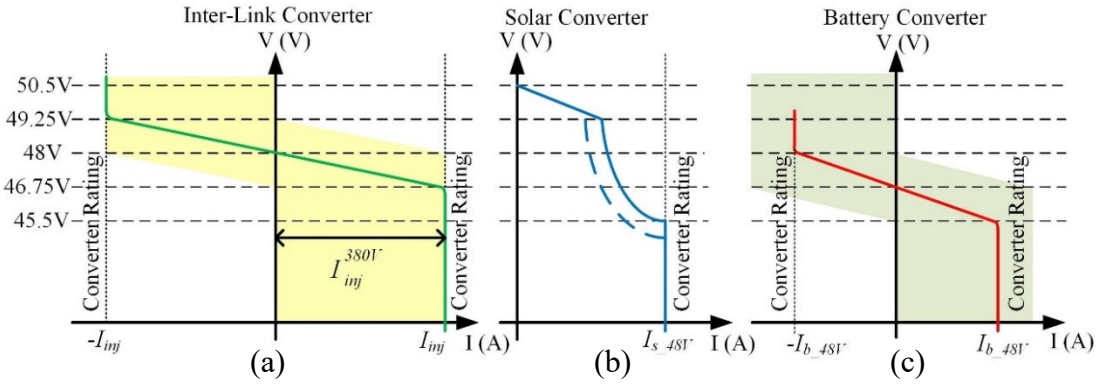

Figure 4. 3: Low voltage 48V DC bus V vs. I characteristics: (a) Inter-Link Converter, (b) Solar Converter, and (c) Battery Converter.

Based on the V vs. I curves in Figure 4. 3, one can say that the LV DC bus battery will not be discharged into the HV DC bus. The LV DC bus is discharged with DC bus voltages less than 46.75V and, at this DC bus voltage, power should flow from the HV DC bus to the LV DC bus, according to the inter-link converter V vs. I characteristic. To avoid power flowing from the LV DC bus to the HV DC bus at light load condition, or when the utility grid cannot absorb the excess power, the inter-link converter (current) limits should be reprogrammed. They are changed based on the HV DC bus voltage, as shown in Figure 4. 4. In addition, Figure 4. 4 shows that the inter-link converter (current) limits are reprogrammed to prevent the HV DC bus battery from discharging into the LV DC bus.

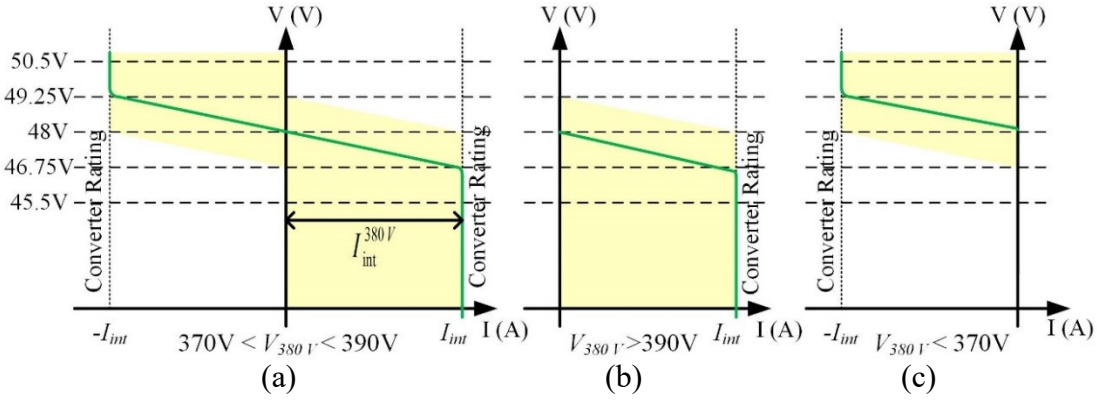

Figure 4. 4: Inter-link converter current limit reprogramed based on the HV DC bus: (a) 370V < V_{HV} < 390V, (b) V_{HV} > 390V, and (c) V_{HV} < 370V.

4.4 Inter-link Converter Modeling and Control Design in Dual DC Buses Nanogrid

Figure 4. 5 shows the schematic of a full-bridge isolated bidirectional DC-DC converter called Dual Active Bridge (DAB) [28-30]. It can provide a high voltage gain using a high frequency transformer with a small volume and weigh. Moreover, the DAB provides a galvanic isolation between the two DC buses, and there is no need for circuit breaker to isolate the buses at fault condition in one of them. There, V_{LV} and V_{HV} are the LV and HV DC bus voltages, respectively, S_1-S_4 and Q_1-Q_4 are the controllable switches, n is the turn's ratio of the transformer, and L is the equivalent leakage inductance of the transformer.

The DAB DC-DC converter is controlled with phase-shift control in this work. There are many types of phase-shift control in the literature [28-31]. However, the most common one (and suitable for this application) is the single-phase-shift (SPS) control shown in Figure 4. 6 [31]. In this control scheme, all the switches are gated with 50% duty cycle. S_1 and S_4 are switched as a pair, complementarily to S_2 and S_3 in the first full bridge. Likewise, Q_1 and Q_4 are switched complementarily to Q_2 and Q_3, in the second, HV side, bridge. That generates square waveforms, V_{AC_HV} and V_{AC_LV}, at the transformer's terminals. The direction and the magnitude of the inductor current can be adjusted by changing the phase shift between the two square waves, as in the traditional AC power transmission systems. This allows the control of the direction and magnitude of the power flow [31-33]. This is achieved with a single control parameter, the phase-shift ratio (d), for an actual phase shift (πd) between V_{AC_HV} and V_{AC_LV}.

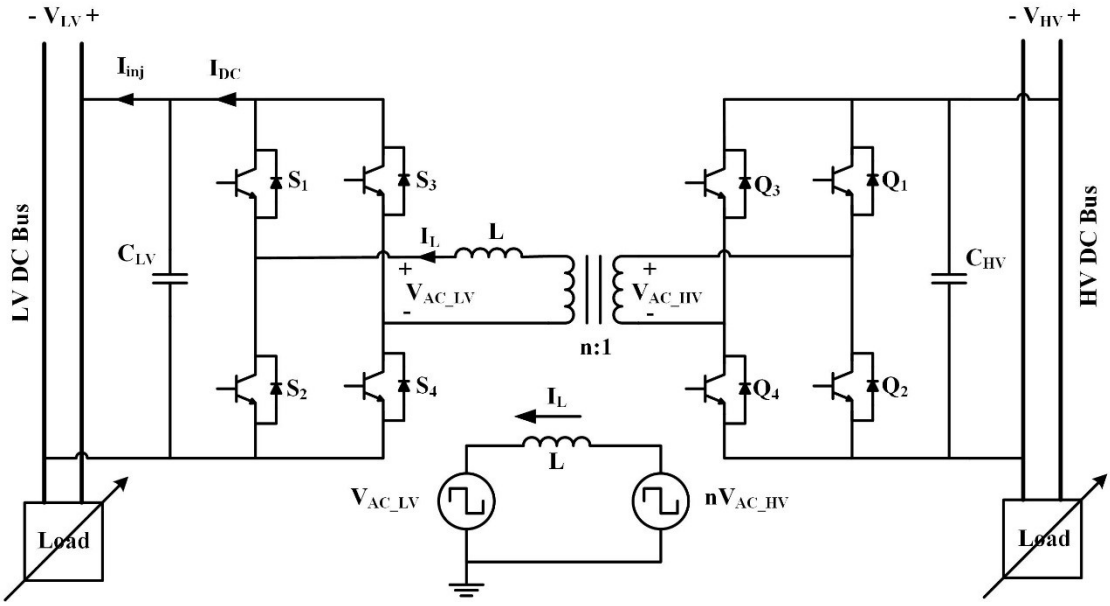

Figure 4. 5: Full-bridge isolated DC-DC converter (DAB).

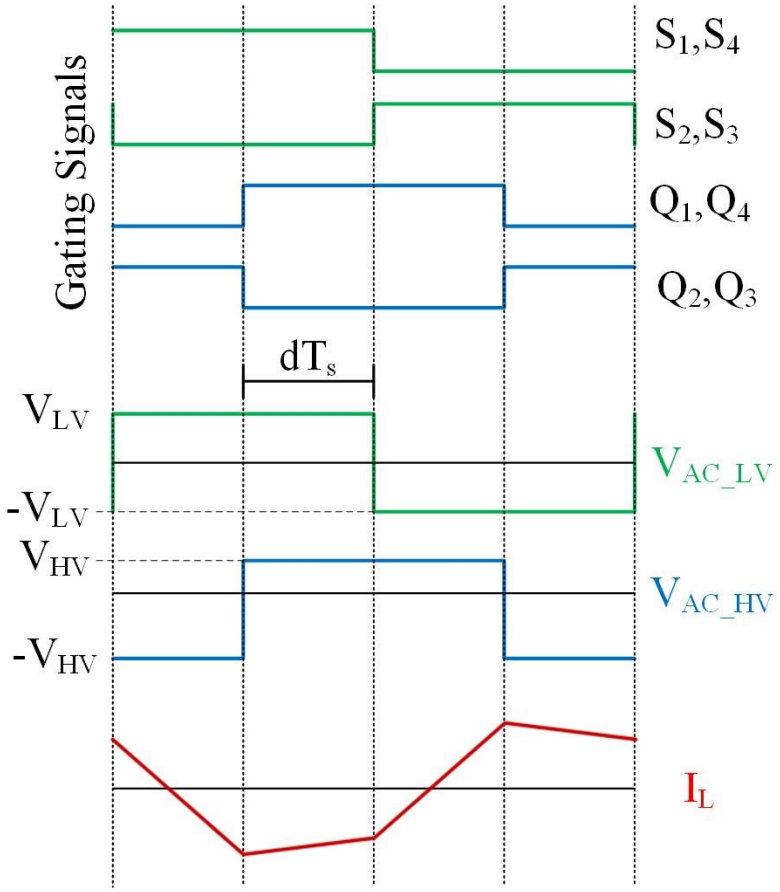

Figure 4. 6: SPS Control waveforms.

The power injected into the LV side of the DC-DC converter in Figure 4. 5 can be expressed as follows for SPS control [28, 34]:

$$P=\frac{nV_{AC\_HV}V_{AC\_LV}}{2f_sL}d(1-|d|) \tag{4.4}$$

Where f_s is the switching frequency, and V_{AC_HV} and V_{AC_LV} are the high side and low side voltages of the transformer. By ignoring the voltage loss of the power switch, V_{AC_HV} could equal V_{HV} and $-V_{HV}$ while V_{AC_LV} could equal V_{LV} and $-V_{LV}$. From equation (4.4), the power has a maximum value when the phase-shift ratio (d) is 0.5. Figure 4. 7 shows the power injected by the 48 V bus vs. the phase shift ratio (d). Power flows from the HV side to the LV side at positive phase-shifts ($0 < \pi d < \pi$) and from the LV side to the HV side at negative phase shifts ($-\pi < \pi d < 0$).

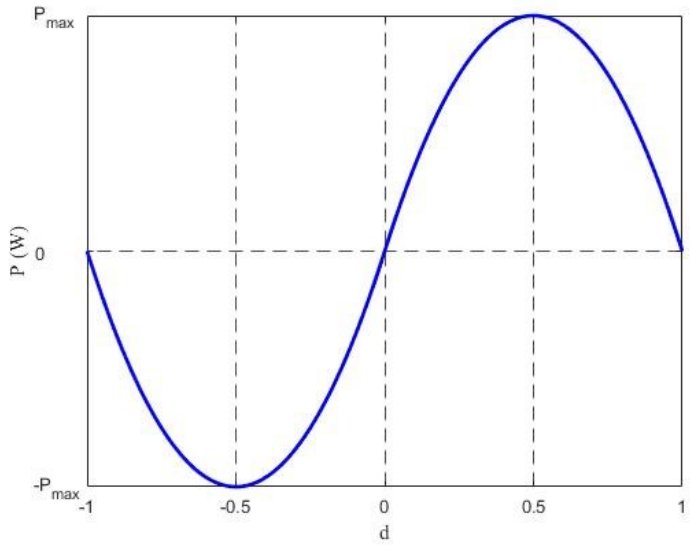

Figure 4. 7: Power injected by the LV bus vs. phase-shift ratio.

Then, the average value of the current at the LV side (I_{DC}) is [34]:

$$I_{DC}=\frac{nV_{AC\_HV}}{2f_sL}d(1-|d|) \tag{4.5}$$

Therefore, the large signal model for the DAB can be obtained by replacing the two full bridges and the HV voltage with a current source of magnitude given in (4.5) and the large signal equivalent circuit is shown in Figure 4. 8 [34]. Moreover, the LV DC bus could be modeled using Thevenin's equivalent circuit with a threshold voltage V_{NL_LV} and a droop resistance R_{dLV}. Then,

the DAB in the dual DC buses nanogrid could be modeled with respect to the LV side in the dual DC nanogrid as shown in Figure 4. 9.

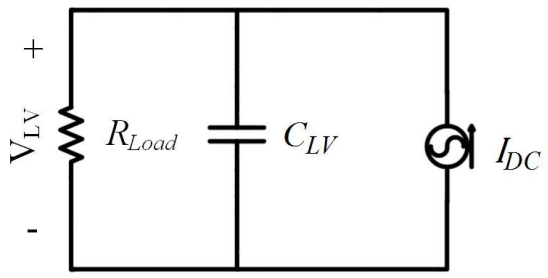

Figure 4. 8: Equivalent circuit of DAB feeding a resistive load.

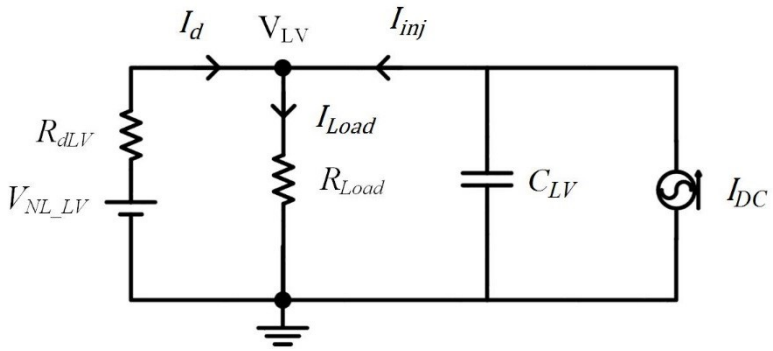

Figure 4. 9: Equivalent circuit of DAB in dual DC buses nanogrid with respect to LV side.

For the study of the dynamic response of the DAB, the expression for the average value of the current injected in the LV DC bus should be linearized around an operating point, leading to a small signal model as in (4.6) [34]. The small signal model for the DAB DC-DC converter with SPS reflected to the LV side, in the DC nanogrid, and assuming that the equivalent threshold voltage of the LV bus (V_{NL_LV}) is constant, is shown in Figure 4. 10.

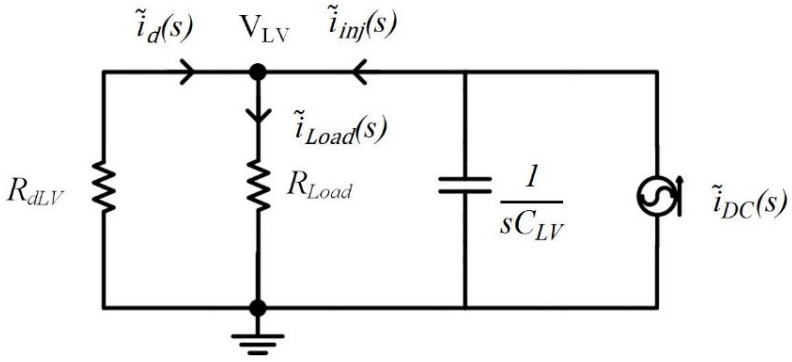

Figure 4. 10: Small signal model of DAB in dual DC buses nanogrid with respect to LV side.

$$\tilde{\imath}_{DC}(s)=\frac{nV_{AC\_HV}}{2f_sL}(1\text{-}2d)\tilde{d}(\mathrm{s}) \tag{4.6}$$

Then, one gets the following expression for the current injected by the inter-link converter into the LV DC bus ($\tilde{\imath}_{inj}(s)$) as a function of variations in the phase shift ratio ($\tilde{d}(s)$).

$$\tilde{\imath}_{inj}(s)=\frac{nV_{AC\_HV}(1\text{-}2d)(R_{dLV}+R_{Load})}{2f_sL(R_{Load}R_{dLV}C_{LV}s+R_{dLV}+R_{Load})}\tilde{d}(s) \tag{4.7}$$

The transfer function of the DAB $G_p(s)$ for the design of the current controller becomes.

$$\frac{\tilde{\imath}_{inj}(s)}{\tilde{d}(s)}=\frac{nV_{AC\_HV}(1\text{-}2d)(R_{dLV}+R_{Load})}{2f_sL(R_{Load}R_{dLV}C_{LV}s+R_{dLV}+R_{Load})} \tag{4.8}$$

4.5 Case Study

As a case study in this work, a DAB as in Figure 4. 5 is used as an inter-link converter with the following parameters: Transformer turns ratio n = 0.25, leakage inductance L=300µH, switching frequency f_s = 20kHz and HV and LV capacitors $C_{HV} = C_{LV}$ = 1500µF. The LV DC bus is modeled by a Thevenin equivalent with the DC voltage V_{NL_LV} = 49.25V and a droop constant R_{dLV} = 0.289Ω. In addition, the HV DC bus is modeled by Thevenin's with the DC voltage V_{NL_HV} = 390V and a droop constant R_{dHV} = 0.289Ω. Then, for a load resistance of 10Ω, the transfer function of the plant becomes:

$$\frac{\tilde{\imath}_{inj}(s)}{\tilde{d}(s)}=\frac{81.5}{0.004335s+10.289} \tag{4.9}$$

Then, a PI type-II compensator is designed for a cut-off frequency of 240Hz [31] and a phase margin PM = 80°. Therefore, the compensator parameters can be calculated as τ = 991µs, T_P = 443µs, and K_{PI} = 0.15. Figure 4. 11 shows the Bode plot for the plant (G), the controller (C) and the loop transfer function (CG).

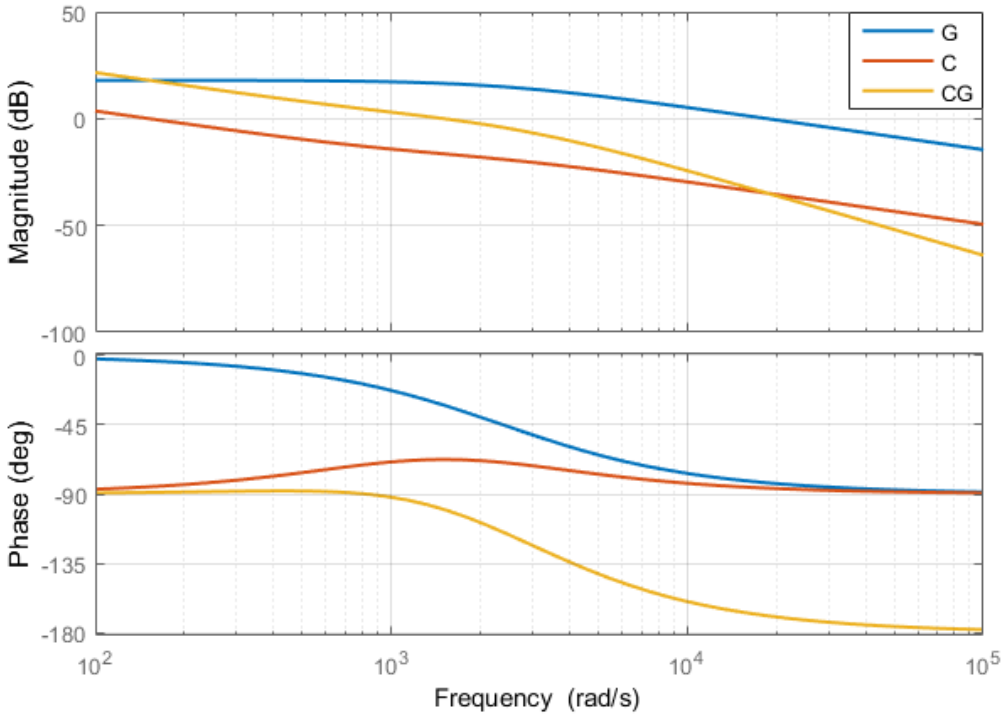

Figure 4. 11: The Bode plot of the model (G), the controller (C) and the combination (CG).

For the current or power sharing, the inter-link converter is controlled with the V vs. I curve in Figure 4. 3, with threshold voltage V_{NL_int} = 48V and R_{dint} = 0.289Ω. The injected current (I_{inj}) from DAB is given by the droop equation (4.1), in the droop mode, or constant at 4.325A in the current limiting mode. The control block diagram is shown in Figure 4. 12. The phase shift PWM control used in this work is realized as shown in Figure 4. 13. The HV side triangular waveform was shifted by 0.25 duty cycle (π/2) to allow negative delay using time delay block. The fixed duty cycle is used to be 0.499 instead of 0.5 to implement a small dead time for the switches.

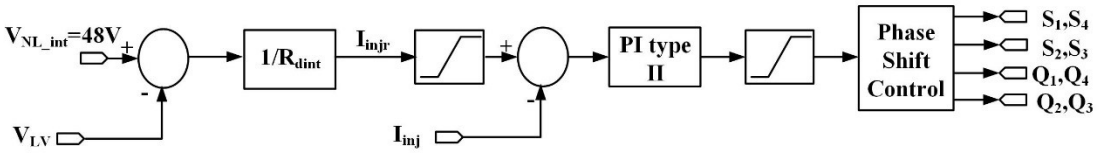

Figure 4. 12: Control block diagram.

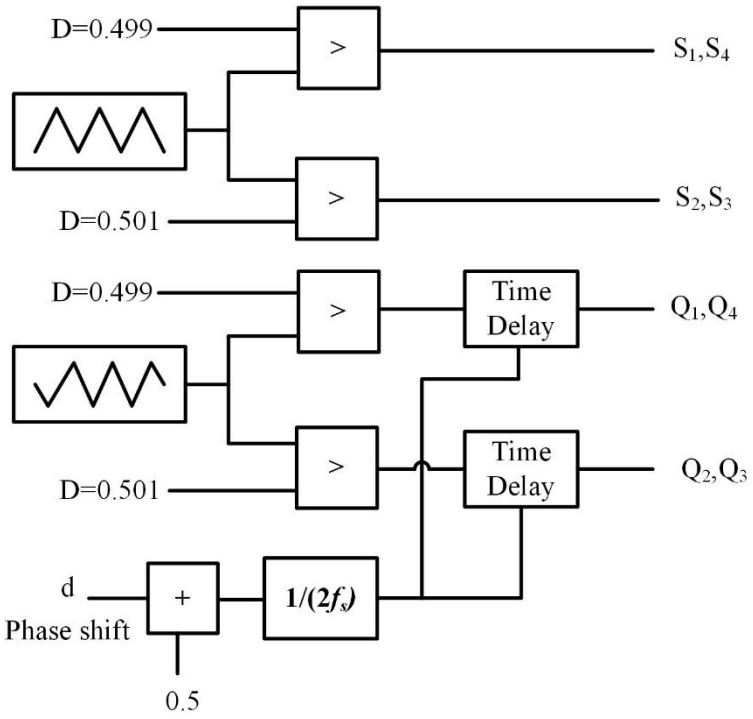

Figure 4. 13: Phase shift PWM block.

4.6 Simulation Results

Considering the dual DC buses nanogrid discussed in this chapter, two types of simulation results were obtained. The first to test the DAB as interlink converter. That can be done by verifying the SPS modulation waveforms described in Figure 4. 6. Then test the proposed model of the DAB in the DC nanogrid. Finally, test the ability of the interlink converter to direct the power between the two DC buses as described in Figure 4. 4. The second test is regarding the full dual DC bus nanogrid in Figure 4. 1 and controlling the power and the current sharing with the V vs. I curve presented in Figure 4.2 and Figure 4.3.

4.6.1 Simulation Results of DAB as Interlink Converter

MATLAB/Simulink is used to simulate the DAB in Figure 4. 5 with the case study parameter and control loop presented in section 4.4. In the first test, an open loop test to verify the SPS modulation waveforms of the DAB described in Figure 4. 6. Figure 4. 14 shows the gating signals of the LV side and HV side of DAB, the AC voltage at the LV side and HV side of the transformer and the transformer leakage inductor current at d = -0.25.

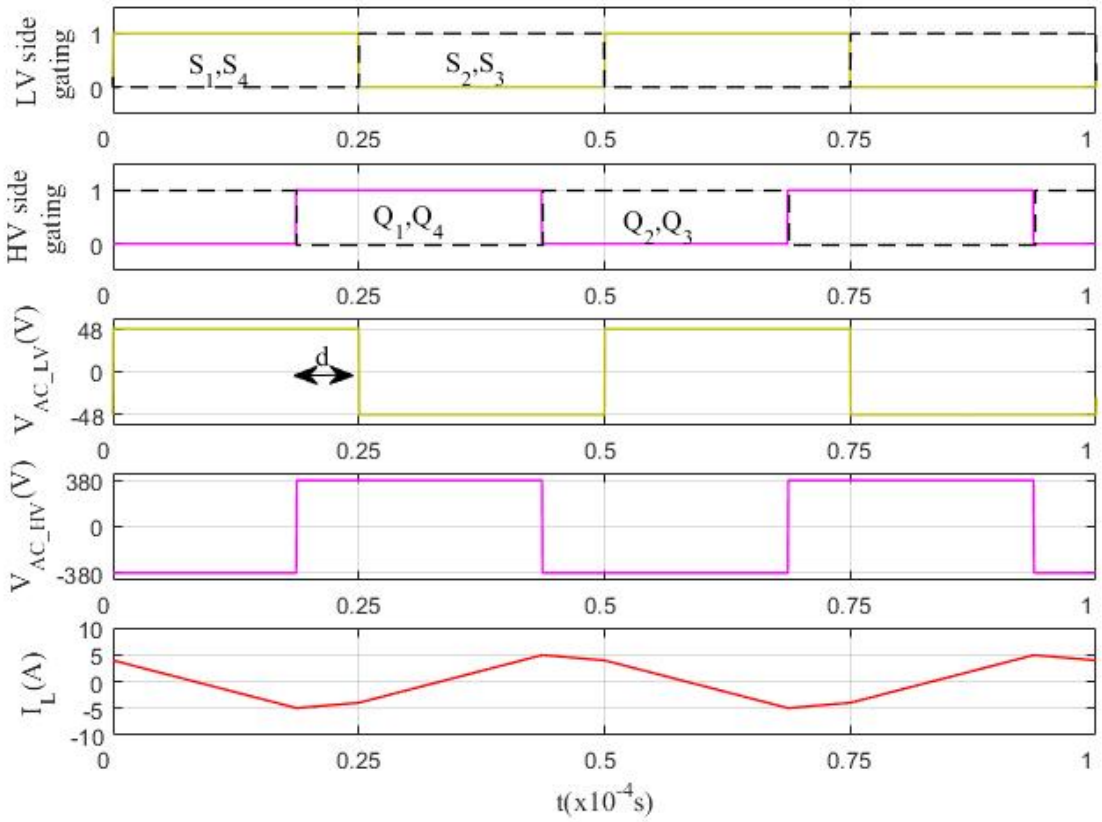

Figure 4. 14: Simulation result of SPS modulation waveforms.

The second test is to verify the performance of the control loop of the current injected into the LV bus. Again, the voltages of the LV and HV sides are set at 48V and 380V respectively. The reference current is initially at -1.5A and then it is changed in a step to 1.5A. As shown in Figure 4. 15, the injected current I_{inj} follows the reference signal very well, reaching the steady state in 0.007s with zero error. The negative injected current I_{inj} sign means that the power flow is from the LV side to the HV side, what is achieved with a negative phase shift. Conversely, a positive injected current I_{inj} means that power flows from the HV side to the LV side, requiring a positive phase shift.

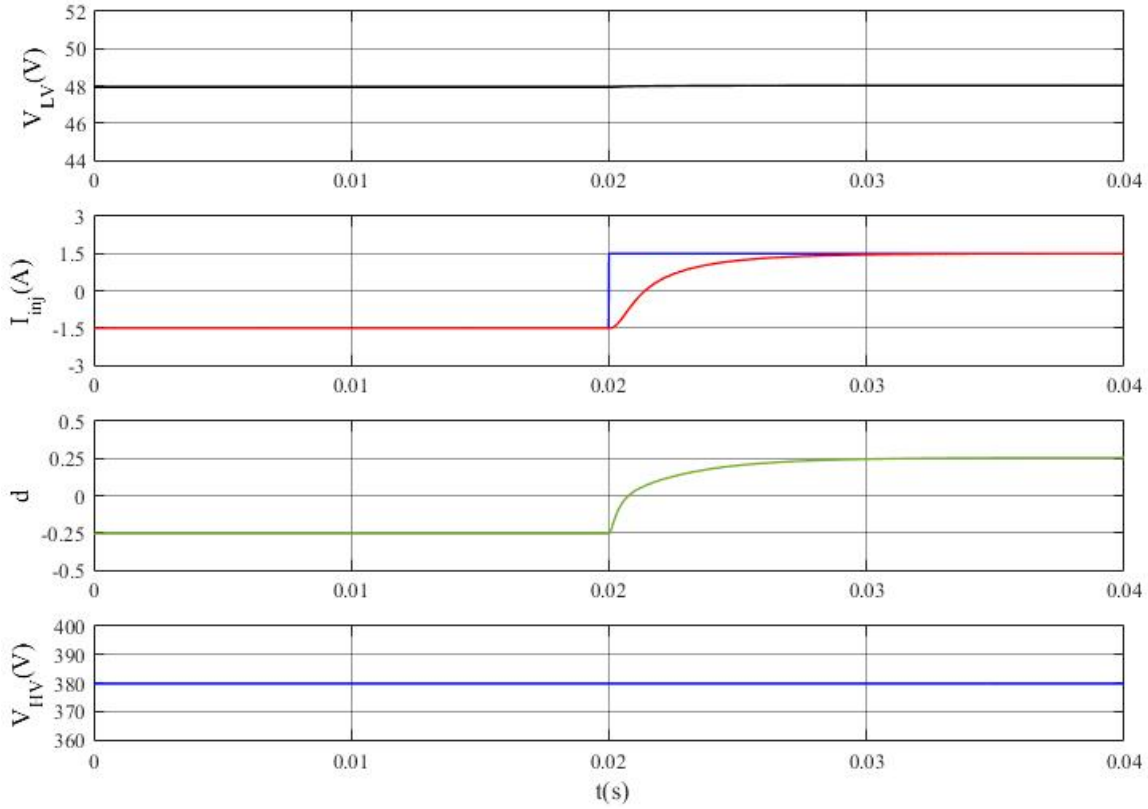

Figure 4. 15: Simulation results for a step change in the injected reference current.

In the last test, the impact of load variations in both DC buses and the power flow controlled by the interlink converter according to the proposed droop control scheme, on the voltages at the LV and HV buses, are investigated. Three cases are considered: First with 370 V< V_{HV} <390 V, then with V_{HV} < 370 V and finally with V_{HV} > 390 V. As discussed before, the interlink converter is droop-controlled based on the magnitude of the voltage at the LV bus, but for low and high at the HV bus, it should be reprogrammed to prevent worsening the problem of excess surplus or shortage of power in that bus.

The LV DC bus and HV DC bus were modeled by threshold voltages and droop resistances. For the LV DC bus V_{NL_LV} = 49.25V and R_{dLV} = 0.289Ω while for the HV DC bus V_{NL_HV} = 390V and R_{dHV} = 0.289Ω. In this case, the LV DC bus voltage can be calculated by (4.11) through the droop equation (4.1) with an equivalent threshold voltage of V_{NL_eq} = 48.625V, obtained considering the threshold voltages of the LV DC bus and interlink converter, and a droop constant R_{deq} = 0.1445Ω, the parallel combination of R_{dLV} and R_{dint}. For a given current injected by the DAB into the LV side, the current drawn from the HV side will be much smaller due to the

turns ratio of the transformer. The HV DC bus voltage can be calculated by (4.10) through the droop equation (4.1) with a threshold of V_{NL_HV} and a droop constant of R_{dHV}.

The simulation results are shown in Figure 4. 16. Initially, both DC buses are connected to 80Ω loads, presenting voltages V_{LV} = 48.54V and V_{HV} = 388.6V. The value of the current injected into the LV bus (I_{inj}) is -1.87A, determined by the V vs. I droop characteristic of the interlink converter. With V_{LV} = 48.54V higher than V_{NL_int} = 48V, power shown be drawn from the LV bus and sent to the HV bus. At t = 0.02s, an additional 40Ω is connected to the LV side, resulting in a decrease in the voltage at that bus, V_{LV} = 48.36V, and in the current the interlink converter draws from the LV bus, I_{inj} = -1.26A.The change, a reduction, in V_{HV} is very small due to the small value of the LV side current reflected to the HV side current and transformer turns ratio. At t = 0.04s, an additional 40Ω is connected to the HV side, and since the reference value for the current of the inter-link is a function of the LV DC bus only, the injected current does not change, the HV DC bus voltage becomes V_{HV} = 385.8V, lower than before. At t = 0.06s, an additional 20Ω is connected to the LV side, reducing the voltage in the LV bus to V_{LV} = 48V what makes $I_{inj} \approx 0$A. At t = 0.08s an additional 20Ω is connected to the HV side, again it does not affect the power sharing and the HV DC bus voltage drops to V_{HV} = 380.4V. At t = 0.1s an additional 40Ω is connected to the LV side, reducing the voltage at this DC bus below 48 V V_{LV} = 47.85V, and the power starts to flow from the HV DC bus to the LV DC bus with injected current: I_{inj} = 0.52A. At t = 0.12s an additional 40Ω is connected to the HV side, and again it does not affect the power sharing and the HV DC bus voltage drops to V_{HV} = 377.7V. At t = 0.14s an additional 20Ω is connected to the LV side, so the injected current increases I_{inj} = 1.73A and this mean more power flow from the HV side to the LV side with more drop in the LV DC bus V_{LV} = 47.5V. Finally, at t = 0.16s an additional 20Ω is connected to the HV side, and it does not affect the power sharing and the HV DC bus voltage drops to V_{HV} = 372.5V.

$$V_{DC} = \frac{R_{Load} V_{NL}}{R_d + R_{Load}} \tag{4.7}$$

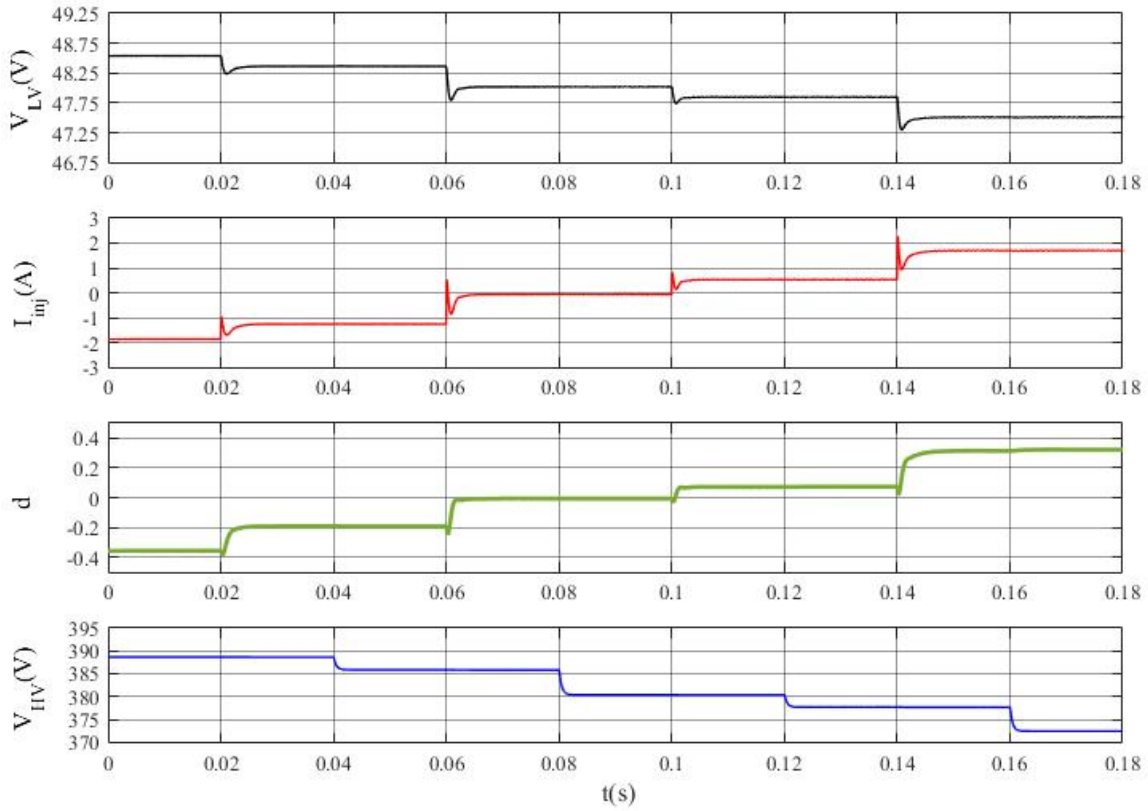

Figure 4. 16: Simulation results considering that 370V < V_{HV} < 390V throughout the simulation time.

Figure 4. 17 shows simulation results for a case with V_{NL_HV} = 395 V, where the voltage at the HV bus is higher than 390V, from t = 0s to 0.6 s. In such a case, the proposed control law for the interlink converter should prevent any power flow to the HV bus, which already has a surplus of power. Initially, both DC buses are connected to 80Ω loads, presenting voltages V_{LV} = 49.32V and V_{HV} = 393.6V. At t = 0.02s, an additional 40Ω load is connected to the HV DC bus, V_{HV} decreases to 390.8V and there is no power flow from the LV to the HV DC bus. At t = 0.04s, an additional 40Ω load is connected to the LV DC bus, V_{LV} = 48.72V, still higher than 48V, and there is no power flow from the LV to the HV DC bus because of the voltage at the HV bus. At t = 0.06s, an additional 40Ω load is connected to the HV DC bus, V_{HV} drops to 385.26V, below 390 V, and power starts to flow from the LV to the HV DC bus. Because of that, V_{LV} drops to 48.36V with I_{inj} = -1.25 A as the V vs. I curve in Figure 4. 4 (a). At t = 0.08s, an additional 40Ω load is connected to the LV DC bus, $V_{LV} \approx$ 48V what makes $I_{inj} \approx$ 0A. In this case, there is no power flow from the LV DC to the HV DC but now it is due to $V_{LV} \approx$ 48V= V_{NL_int}. After that, power flow from the HV to the LV DC bus increases at t = 0.12s and t = 0.16s when loads are added to the LV bus, but not at t = 0.14s when there is a load increase in the HV DC bus.

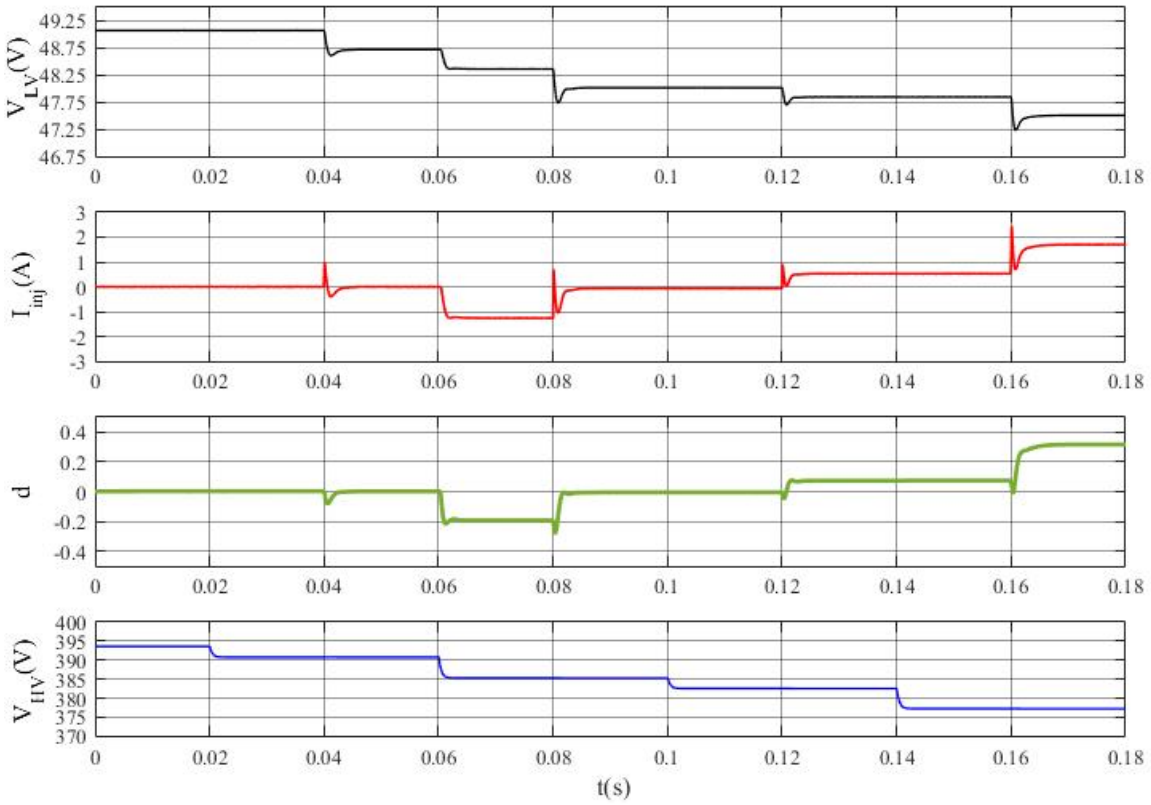

Figure 4. 17: Simulation results for the case where $V_{HV} > 390$V for a certain time interval.

Figure 4. 18 shows simulation results for a case with $V_{NL\_HV} = 380$ V, were the HV DC bus is lower than 370V, from $t = 0.1$s to 0.18s. In such case, the proposed control logic of the inter-link converter prevents the power flow from the HV DC bus to LV DC bus. This is achieved by reprograming the current limit as in Figure 4. 4 (c), $I_{inj} = 0$. This prevents the HV DC bus battery's from discharge through the LV DC bus. Initially, both DC buses are connected to 80Ω loads, presenting voltages $V_{LV} = 48.54$V and $V_{HV} = 378.63$V with $I_{inj} = -1.87$A, meaning that power flows from the LV to the HV side. At $t = 0.02$s, an additional 40Ω load is connected to the HV DC bus, V_{HV} decreases to 375.9V without changes in the current of the interlink converter. At $t = 0.04$s, an additional 40Ω load is connected to the LV DC bus, V_{LV} decreases to 48.36V, indicating a reduction of the surplus of power in the LV side, what makes I_{inj} reduce to -1.26A. At $t = 0.06$s, an additional 40Ω load is connected to the HV DC bus, V_{HV} drops to 370.63V. At $t = 0.08$s, an additional 40Ω load is connected to the LV DC bus, $V_{LV} \approx 48$V what makes $I_{inj} \approx 0$A. In this case, there is no power flow from the LV DC to the HV DC, since $V_{LV} \approx 48\text{V} = V_{NL\_int}$. At $t = 0.1$s an additional 40Ω load is connected to the HV DC bus, V_{HV} drops to 368.05V, below 370V, and the interlink should prevent the power flow from the HV DC bus to the LV DC bus as described in Figure 4. 4 (c).

Therefore, at t = 0.12s, when an additional 40Ω is connected to LV DC, I_{inj} = 0 indicating that power does not flow from the HV DC bus to the LV DC bus even though V_{LV} = 47.7V, < V_{NL_int} = 48V as discussed in Figure 4. 4 (a). After that, power flow from the HV to the LV DC bus is still prevented, at t = 0.14 s and t = 0.16 s when loads are added to the HV bus and LV bus respectively.

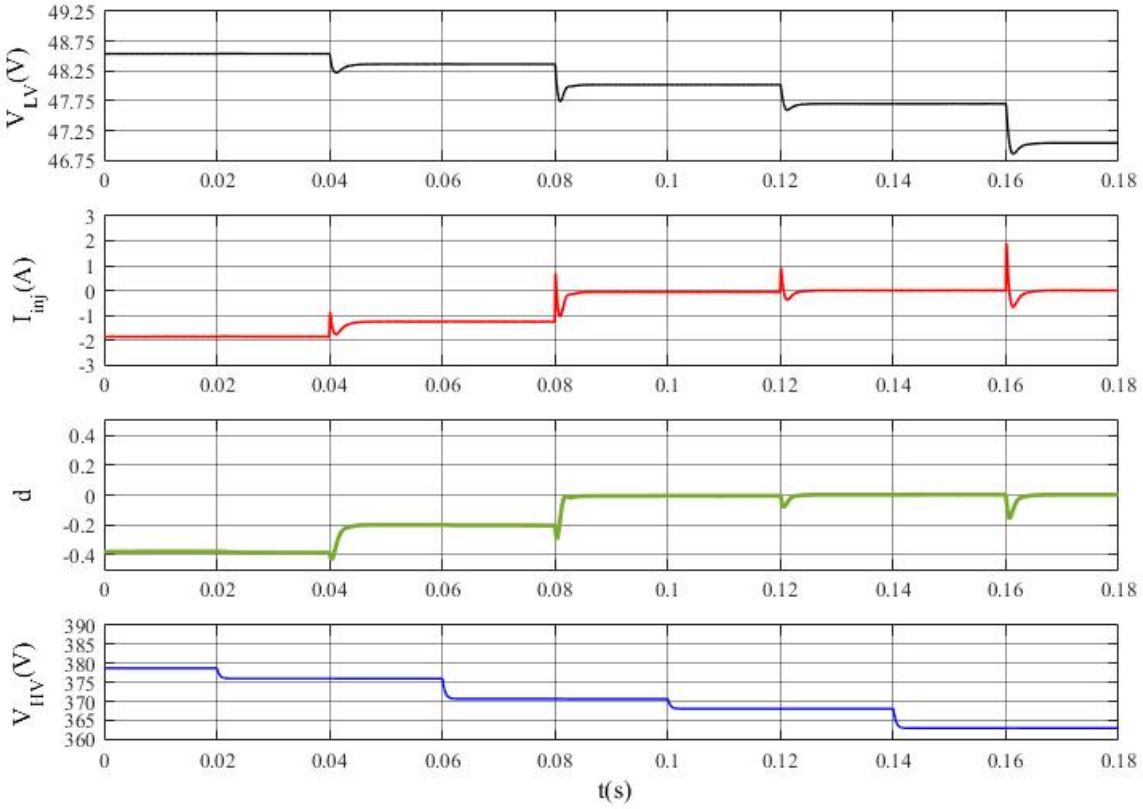

Figure 4. 18: Simulation results for the case where V_{HV} < 370V for a certain time interval.

4.6.2 Simulation Results of Dual DC Buses Nanogrid

MATLAB/Simulink is used to simulate the dual DC buses nanogrid in Figure 4. 1 under different operation conditions. A class C DC-DC converter as in Figure 4.19 is used as the main power electronics interface of the DERs: Solar panels and batteries. A class C DC-DC converter is also used along with a DC-AC converter as the two-stage AC grid interface.

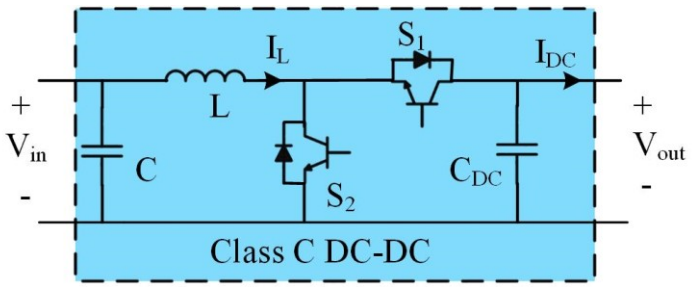

Figure 4. 19: Class C DC-DC converter.

Regarding the power and the current sharing the V vs. I in Figure 4.2 and Figure 4.3 were used. For the HV DC bus DERs, 5 kW PV panel and battery were considered with a droop constant $R_{dS\_380} = R_{dB\_380} = 0.763\Omega$, and 10 kW grid connection was considered with a droop constant $R_{dG} = 0.3815\Omega$. Resulting in 14.2A, 13.11A and 26.22A as current limits for the solar, battery and grid converters respectively. For the LV DC bus DERs, 2 kW PV panel, battery and interlink were considered with a droop constant $R_{dS\_48} = R_{dB\_48} = R_{dint} = 0.0289\Omega$. Resulting in 44A current limit for the solar converter and 43.25A current limit for the battery and interlink converters. The supercapacitors (SC) were controlled to support the dynamics of the batteries current by splitting the storage inductor current into low frequencies for the battery and high frequencies for the SC using a low-pass-filter (LPF) with a 30Hz cut-off frequency.

The same current control loop parameters can be used for all DERs at the same DC bus. A PI type-III controller was designed for the same equivalent plant with a transfer function shown in (4.8) [43, 60]. They were designed for a crossover frequency of $f_x = 2$ kHz (10% of the switching frequency) and phase margin of $PM = 80°$ for both DC buses. For the LV DC bus converters, the following plant parameters were used: $V_{out} = V_{DC} = 48V$, $I_{DC} = 41.67A$, $R = 1.152\Omega$, $L = 300\mu H$, $C = 1500\mu F$, and $D = 0.46$ for $V_{PV} = V_B = V_{SC} = 29V$. R was selected as the maximum load that could be supplied by the RES alone. At the end, the PI controller parameters are computed as $K_{PI} = 0.0117$, $\tau = 175\mu s$ and $T_P = 36\mu s$. For the HV DC bus converters, the following plant parameters were used: $V_{out} = V_{DC} = 380V$, $I_{DC} = 13.16A$, $R = 27.94\Omega$, $L = 3000\mu H$, $C = 1500\mu F$, and $D = 0.39$ for $V_{PV} = V_{Bat} = V_{SC} = 232V$. R was selected as the maximum load that could be supplied by the RES alone. At the end, the PI controller parameters are computed as $K_{PI} = 0.0015$, $\tau = 171\mu s$ and $T_P = 37\mu s$. The inter-link converter with the following parameters: Transformer turns ratio n = 0.25, leakage inductance L=10.7µH, switching frequency $f_s = 20kHz$ and HV and LV capacitors $C_{HV} = C_{LV} = 1500\mu F$. Then, a PI type-III compensator is designed for a cut-off frequency of 240Hz

[31] and a phase margin $PM = 80^{o}$. Therefore, the compensator parameters can be calculated as τ = 1.4ms, T_P = 318µs, and K_{PI} = 0.049 at a load resistance of 1.15Ω.

$$G_{di}(s) = \frac{\tilde{\imath}_L(s)}{\tilde{d}(s)} = \frac{CV_{out}s + 2I_{DC}}{LCs^2 + \frac{L}{R}s + (1-D)^2} \tag{4.8}$$

The first test of the dual DC buses nanogrid is with grid connection and the batteries are not fully charged. The indication of the load variations in the system with the respective times as well as the numerical values of the voltage and current waveforms shown in Figure 4.20 and Figure 4.21 are summarized in Table 4.1 and Table 4.2 for the HV DC bus and the LV DC bus, respectively. Based on these results the nanogrid operates according to the V vs. I curves presented in Figure 4.2 and Figure 4.3 for HV DC bus and LV DC bus respectively. The RESs operate at maximum power. At the HV DC bus, the battery and the grid converter operate with droop control, the battery in charging mode and the grid support the nanogrid by supplying power. At the LV DC bus, the battery and the interlink converter operate with droop control, the battery in charging mode and the interlink supporting the LV DC bus.

Table 4. 1: Numerical results of the HV DC bus from Figure 4.20.

Time (s)	*Load (Ω)*	$V_{HV}(V)$	$I_{PV\_380}(A)$	$I_G(A)$	$I_{B\_380}(A)$	$I_{Load\_380}(A)$
Initially	305	379.3	13.2	1.8	-12.2	1.2
t = 0.2	63.4	378	13.2	5.2	-10.5	6
t = 0.4	35.4	376.7	13.25	8.6	-8.8	10.7
t = 0.6	24.5	375.3	13.3	12.3	-7	15.3
t = 0.8	18.8	374	13.3	15.6	-5.3	20

Table 4. 2: Numerical results of the LV DC bus from Figure 4.21.

Time (s)	*Load (Ω)*	$V_{LV}(V)$	$I_{PV\_48}(A)$	$I_{int}(A)$	$I_{B\_48}(A)$	$I_{Load\_48}(A)$
Initially	40	47.94	41.7	2	-42	1.2
t = 0.1	7	47.86	41.7	4.8	-40	6.8
t = 0.3	3	47.75	41.7	8.7	-35	16
t = 0.5	1.95	47.62	42	13	-30	24.4
t = 0.7	1.64	47.56	42	15.2	-28	29
t = 0.9	1.27	47.45	42	19	-24	37.5

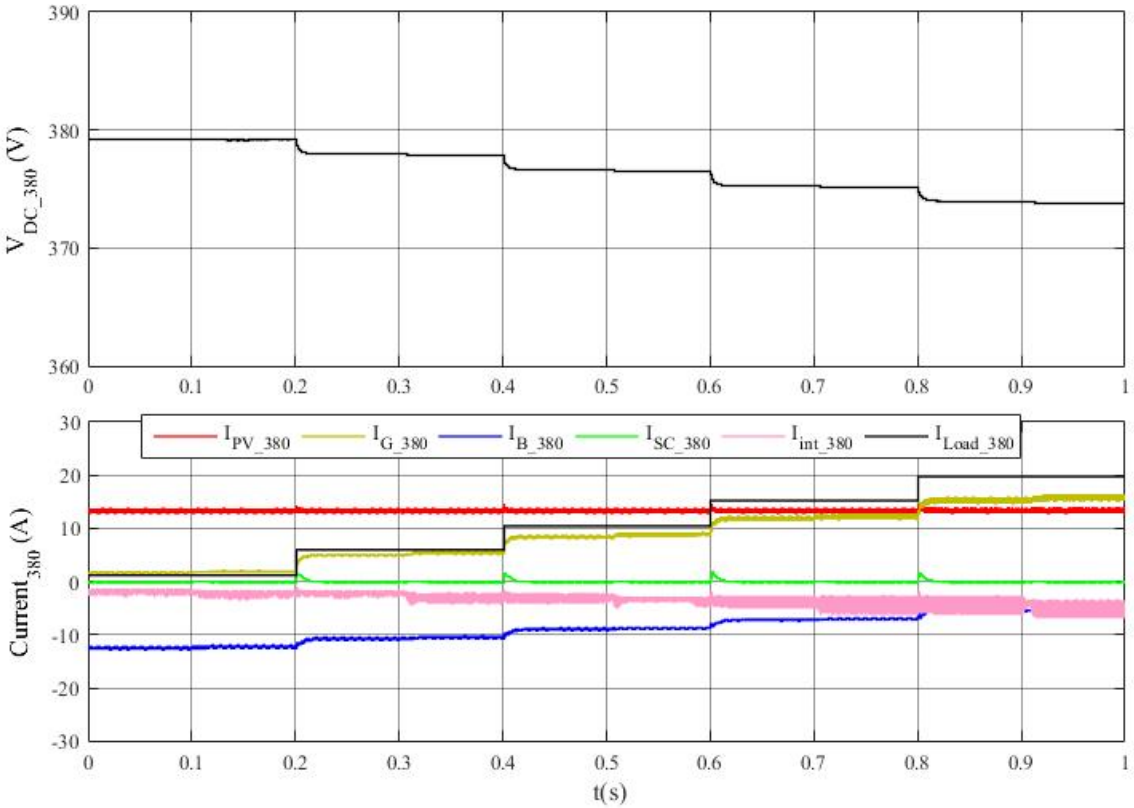

Figure 4. 20: Simulation results of the dual DC buses nanogrid with grid connection. Waveforms of the HV DC bus.

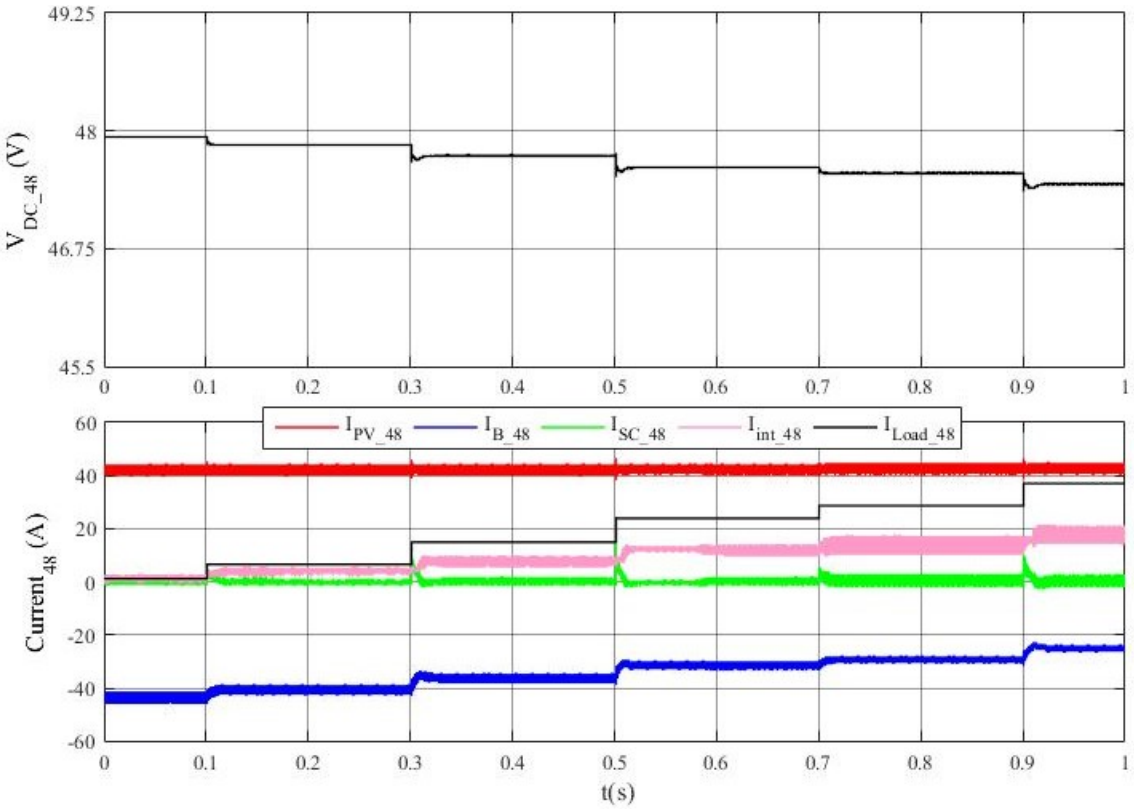

Figure 4. 21: Simulation results of the dual DC buses nanogrid with grid connection. Waveforms of the LV DC bus.

The second test of the dual DC buses nanogrid is without grid connection and with the batteries not fully charged. The indication of the load variations in the system with the respective times as well as the numerical values of the voltage and current waveforms shown in Figure 4.20 and Figure 4.21 are summarized in Table 4.1 and Table 4.2 for the HV DC bus and the LV DC bus, respectively. Based on these results the nanogrid operates as V vs I presented in V vs. I in Figure 4.2 and Figure 4.3 for HV DC bus and LV DC bus respectively. By comparing the cases above, one can say that the grid connection gives the DC nanogrid more power availability, missing this support leads to a higher voltage drop in the DC buses, especially at the HV DC bus. Moreover, the battery starts to discharge at t = 0.6s, while it was in the charging mode with the grid connection. Regarding the LV DC bus the effect of missing the grid connection is less once the HV DC bus is higher than 370V due to the power and current sharing V vs I is based on the LV DC bus. Therefore, there is no change in the LV DC bus before t = 0.5s according to Table 4.4 as compared with Table 4.2. At t = 0.6 s the HV DC load was increased to 24.5Ω and the HV DC bus drops below 370 V, the HV battery operates in discharging mode, the interlink converter prevents the power flow from the HV DC to the LV DC bus (I_{int} = 0) so the HV DC bus battery will not discharge through the LV DC bus. After t = 0.6 s the LV DC bus misses the support from the HV DC bus. Therefore, the voltage drops in the LV DC bus in Table 4.4 increases compared with the case with grid connection in Table 4.2 at the same load level. The RESs operate at maximum power at all periods.

Table 4. 3: Numerical results of the HV DC bus from Figure 4.22.

Time (s)	*Load (Ω)*	$V_{HV}(V)$	$I_{PV\_380}(A)$	$I_G(A)$	$I_{B\_380}(A)$	$I_{Load\_380}(A)$
Initially	305	378	13.2	0	-10.5	1.2
t = 0.2	63.4	374.3	13.25	0	-5.6	5.9
t = 0.4	35.4	370.5	13.4	0	-0.5	10.5
t = 0.5	No change	370	13.5	0	0	10.5
t = 0.6	24.5	368	13.5	0	2.5	15
t = 0.8	18.8	364.7	13.6	0	7	19.5

Table 4. 4: Numerical results of the LV DC bus from Figure 4.23.

Time (s)	*Load (Ω)*	$V_{LV}(V)$	$I_{PV\_48}(A)$	$I_{int}(A)$	$I_{B\_48}(A)$	$I_{Load\_48}(A)$
Initially	40	47.94	41.7	2	-42	1.2
$t = 0.1$	7	47.86	41.7	4.8	-40	6.8
$t = 0.3$	3	47.75	41.7	8.7	-35	16
$t = 0.5$	1.95	47.62	42	13	-30	24.4
$t = 0.6$	No change	47.28	42	0	-18	24.2
$t = 0.7$	1.64	47.16	42	0	-14	28.8
$t = 0.9$	1.27	46.93	42	0	-6	37

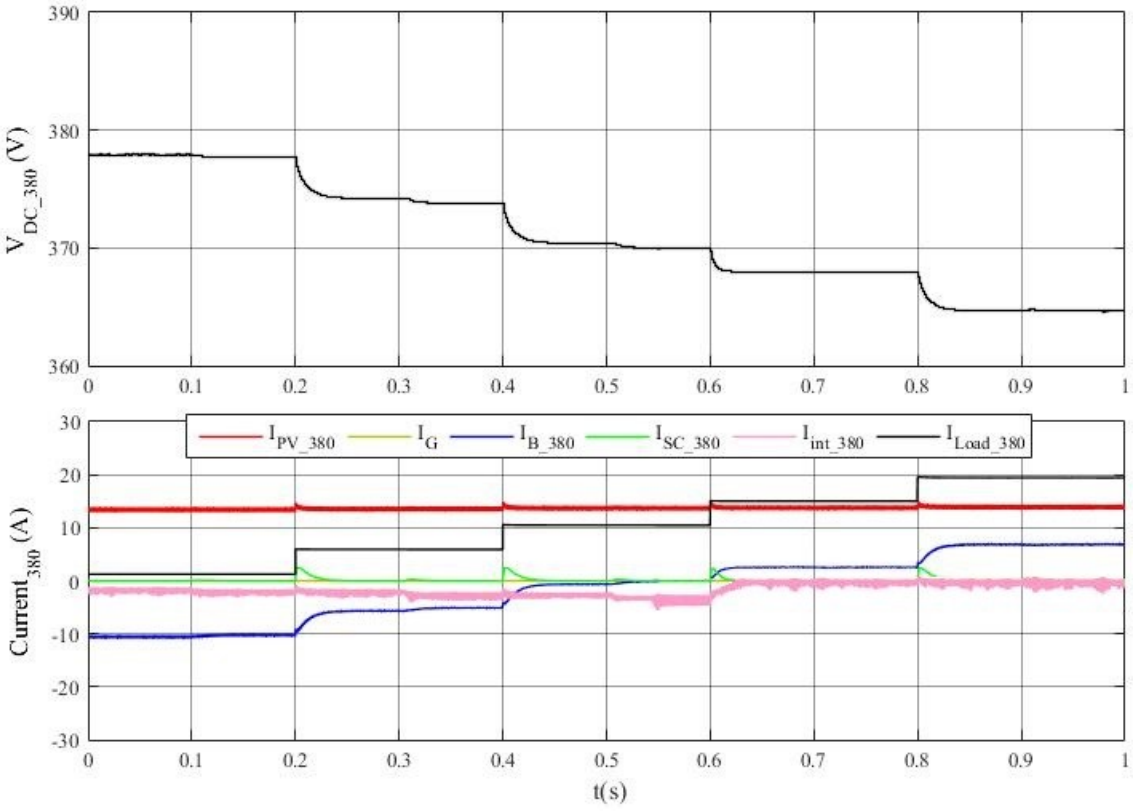

Figure 4. 22: Simulation results of the dual DC buses nanogrid without grid connection. Waveforms of the HV DC bus.

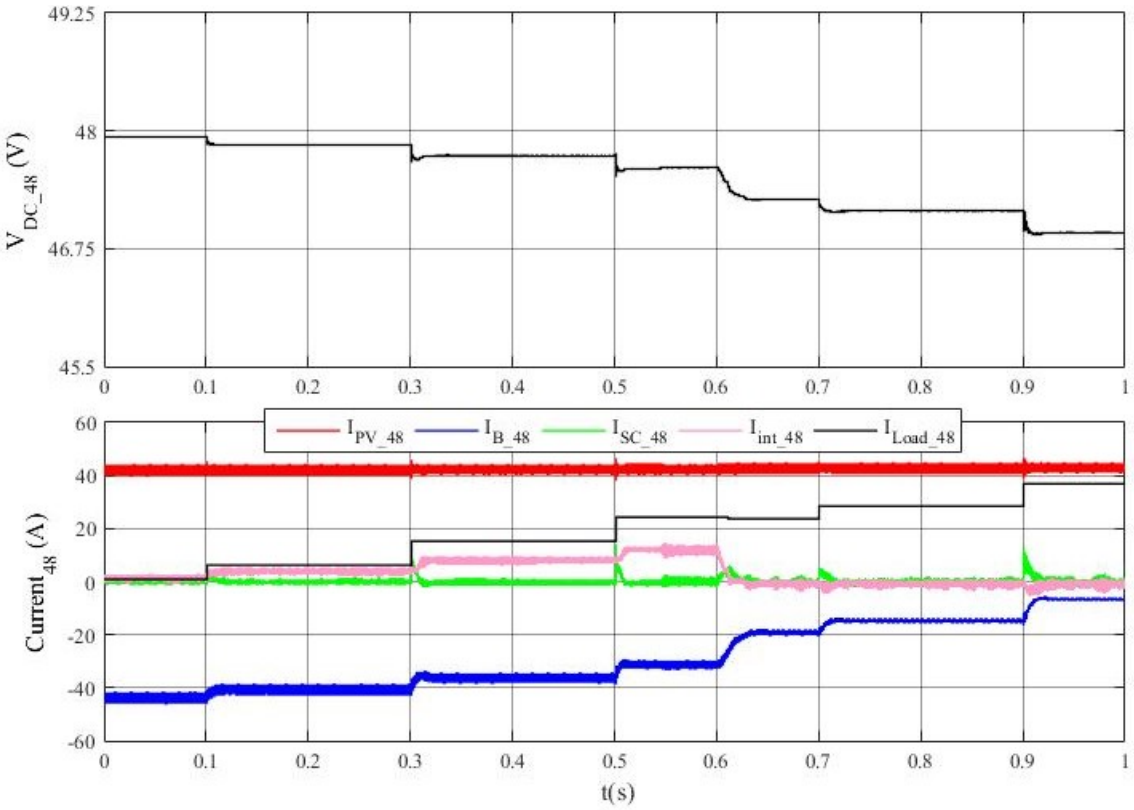

Figure 4. 23: Simulation results of the dual DC buses nanogrid without grid connection. Waveforms of the LV DC bus.

4.7 Conclusions

This chapter discusses a bidirectional inter-link converter to control the power flow between the HV and LV buses of a dual DC bus nanogrid. A control strategy based on DC bus signaling (DBS), so that its impact on the DC buses with other DBS-controlled DERs can be easily determines, is proposed. Since the HV bus is typically stronger than the LV one, the voltage at the LV side is the one that determines the power flow between DC buses. This is equivalent to the V vs I curve of an AC grid converter of a single DC bus nanogrid. However, if the HV bus presents a significant surplus or shortage of power, what can be determined by its bus voltage, V_{HV}, the interlink converter is prevented from making these conditions worse. This is an important feature for dual DC bus systems operating permanently or momentarily disconnected from the AC utility grid. A suitable topology for this power converter, bidirectional with high gain and galvanic isolation, called DAB is selected. A dynamic model for the interlink converter operating with a single phase-shift (SPS) modulation scheme in a droop controlled environment is presented. Then, a closed loop controller for the current injected into the LV DC bus, as a function of the LV DC

bus voltage, is designed. Various aspects of the performance of the droop controlled interlink converter in a dual DC bus nanogrid are verified by means of simulations with MATLAB-Simulink.

CHAPTER FIVE: CONCLUSIONS AND FUTURE WORK

The concept of nanogrids seems very promising for the realization of net-zero energy homes (NZEHs). It should allow the integration of green, but stochastic, renewable energy sources (RESs) and also electric vehicles (EVs) at the user's side of the power meter, in a way that will mitigate the variations of power demanded from and supplied to the utility grid. This should benefit the consumer as well as improve the power quality at the AC utility grid even with conventional voltage regulation equipment and practice. The use of DC nanogrids should lead to a system of increased efficiency, with respect to the conventional residential AC systems, since most of the RESs and storage units present DC characteristics and DC-DC converters offer a higher efficiency than their DC-AC counterparts. Besides, there should be not major concerns regarding the utilization of modern home appliances, because most of them are electronically controlled and present an intermediate DC bus that can be supplied directly from the DC bus.

This research work considered a DC nanogrid with dual DC buses: HV (380V) DC bus and LV (48V) DC bus. The LV bus is safer and appropriate to power loads of up to 1 kW. The HV bus allows the supply of larger loads, with lower currents and losses than what occur for the LV bus. The HV DC bus should allow an easy interconnection to a single-phase three-wire AC utility system. Besides, it can provide a solid platform for interfacing in DC with EVs, what can be done for charging only or for vehicle-to-home (V2H) operation, where the storage system of the EV can also be employed for power balancing and further optimization of the DC NZEH. With several components in the system, it is essential to provide a means for coordinating their operation. The hierarchical control scheme with a primary control level based on DC bus signaling (DBS), which has been considered in a number of reference publications, is adopted in this work. It is evident that there are many challenges to make such a system economically viable and reliable. Some of them were investigated in this Thesis.

In terms of RES, solar photovoltaic (PV) is one that is commonly found in NZEHs. For operation with DBS, the solar converter typically presents a V vs. I curve with three regions: Droop control, MPPT and current limiting. The operation of the converter in steady-state in any of these regions is well understood. However, as the solar irradiance and the load demand in the DC bus vary, the region of operation of the solar converter can change very fast leading to potentially high

variations in the power it injects into the DC bus resulting in sudden variations in the DC bus voltage and decrease in the power quality. In this work, an alternative control scheme for smooth transitions from one mode to another and suitable for operation of solar interfaces with a single stage was presented. Unlike in the dual stage converters, which present a certain decoupling between the input and output powers, the use of conventional MPPT schemes, that rely in continuous variation of the power drawn from the PV converter could not be used. Instead, a less-known MPPT scheme which is based on prior knowledge of the characteristics of the PV panel was employed. Then, a logic for determining the reference current/power of the PV converter based on the DC bus voltage and the conditions of the PV panel by comparing the magnitudes of the reference currents in the three regions and selecting the appropriate, was devised. The performance of the proposed scheme was verified by means of simulations and experimental results.

This thesis also focused on energy storage units, which are essential for balancing power demand and supply in a DC nanogrid with stochastic RESs and variable loads. Usually, hybrid energy storage systems (HESSs) with supercapacitors providing the fast and high currents that are detrimental for the life span of batteries are used. The HESS is controlled with a single V vs. I curve within the DBS concept, what prevents the supercapacitor from also supporting the DC bus voltage in cases of sudden power unbalances. An approach based on an independent control of batteries and supercapacitors was proposed. A V vs. I curve with a droop factor much smaller than that of the battery inverter was selected so that the supercapacitor provides/absorbs large currents for power balancing and voltage regulation. In order to avoid the supercapacitor, which has low energy capacities compared to a battery, a high pass filter (HPF) was used in the path of the reference current. An approach for selecting the droop factor of the supercapacitor interface and the frequency of the HPF was proposed. The performance of the proposed scheme was verified by means of simulations and experimental results.

Another aspect investigated in this thesis concerns the operation of a dual DC bus nanogrid with RES and storage units deployed in both the HV and LV DC buses. In the conventional schemes, all power consumed in the LV DC bus comes from either the RES and storage units of the HV bus or from the AC bus through a utility grid AC-DC converter. In such a case, the converter between the HV and LV is unidirectional in power and if it fails, the LV bus is de-

energized. With RES and storage units placed in both buses, a bidirectional DC-DC converter must be used to avoid wasting of energy in one bus or the other. An isolated dual active bridge (DAB) converter with a single phase-shift (SPS) modulation scheme was considered for this application. In terms of V vs. I curve for the interlink converter, it should be such that it would not conflict with those of the other elements present in either buses. Considering that the LV bus tends to be weaker than the HV bus, which can be or not, AC grid connected, the current of the interlink converter is dictated mostly by the voltage in the LV DC bus. However, if the voltage in the HV DC bus shows a significant surplus or shortage of power, an action of the interlink converter that could worsen this condition is prevented. The performance of the proposed scheme was verified by means of simulations.

Future Work

- Conduct additional tests on the dual DC bus nanogrid, considering higher impact phenomena such as the connection and disconnection of RESs, energy storage units and AC utility grid interface.
- Introduce a low bandwidth communication link realizing the functions of the secondary and tertiary control levels of the hierarchical control strategy considered for the DC nanogrid. This would allow the reprograming of the V vs. I curves so as to keep the DC bus voltage closer to the rated values while better managing the state-of-charge (SoC) of the batteries. Besides in the case of high SoC, the battery could have a priority in feeding the load over the utility grid, thus reduces the power consumption from the utility grid.
- Develop an *optimal energy utilization algorithm* based on long and/or short-term histories of the local renewable energy generation. This should also take into consideration the nanogrid load profiles as well as the history of the state of charge (SoC).

REFERENCES

[1] S. Alepuz, S. Busquets-Monge, J. Bordonau, J. Gago, D. Gonzalez and J. Balcells, "Interfacing Renewable Energy Sources to the Utility Grid Using a Three-Level Inverter," IEEE Transactions on Industrial Electronics, vol. 53, pp. 1504-1511, 2006.

[2] V.C. Güngör, D. Sahin, T. Kocak, S. Ergüt, C. Buccella, C. Cecati and G.P. Hancke, "Smart grid technologies: communication technologies and standards," Industrial Informatics, IEEE Transactions On, vol. 7, pp. 529-539, 2011.

[3] J. Bryan, R. Duke and S. Round, "Distributed generation–nanogrid transmission and control options," in International Power Engineering Conference, pp. 341-346, 2003.

[4] C. Rubio and A. Siddiqui, "Shape of the microgrid [C]," in 2001 IEEE Power Engineering Society Winter Meeting. Columbus: IEEE, pp. 150-153, 2001.

[5] D. Boroyevich, I. Cvetković, D. Dong, R. Burgos, F. Wang and F. Lee, "Future electronic power distribution systems a contemplative view," in Optimization of Electrical and Electronic Equipment (OPTIM), 2010 12th International Conference on, pp. 1369-1380, 2010.

[6] I. Sartori, A. Napolitano and K. Voss, "Net zero energy buildings: A consistent definition framework," Energy Build., vol. 48, pp. 220-232, 5. 2012.

[7] D. J. Hammerstrom, "AC Versus DC Distribution SystemsDid We Get it Right?" in Power Engineering Society General Meeting, 2007. IEEE, pp. 1-5, 2007.

[8] ISC Committee, "IEEE standard for interconnecting distributed resources with electric power systems," New York, NY: Institute of Electrical and Electronics Engineers, 2003.

[9] D. Dong, T. Thacker, R. Burgos, D. Boroyevich, F. Wang and B. Giewont, "Control design and experimental verification of a multi-function single-phase bidirectional PWM converter for renewable energy systems," in Power Electronics and Applications, 2009. EPE'09. 13th European Conference on, pp. 1-10, 2009.

[10] T. Thacker, R. Burgos, F. Wang and D. Boroyevich, "Single-phase islanding detection based on phase-locked loop stability," in Energy Conversion Congress and Exposition, 2009. ECCE 2009. IEEE, pp. 3371-3377, 2009.

[11] L. Roggia, L. Schuch, J. E. Baggio, C. Rech and J. R. Pinheiro, "Integrated Full-Bridge-Forward DC–DC Converter for a Residential Microgrid Application," IEEE Transactions on Power Electronics, vol. 28, pp. 1728-1740, 2013.

[12] R. S. Balog and P. T. Krein, "Bus Selection in Multibus DC Microgrids," IEEE Transactions on Power Electronics, vol. 26, pp. 860-867, 2011.

[13] J. Chen, J. Chen, R. Chen, X. Zhang and C. Gong, "Decoupling control of the non-grid-connected wind power system with the droop strategy based on a DC micro-grid," in 2009 World Non-Grid-Connected Wind Power and Energy Conference, pp. 1-6, 2009.

[14] F. Blaabjerg, A. Consoli, J. A. Ferreira and J. D. van Wyk, "The future of electronic power processing and conversion," IEEE Transactions on Industry Applications, vol. 41, pp. 3-8, 2005.

[15] F.A. Farret and M.G. Simões, Integration of alternative sources of energy, John Wiley & Sons, 2006, .

[16] P. Biczel, "Power Electronic Converters in DC Microgrid," in 2007 Compatibility in Power Electronics, pp. 1-6, 2007.

[17] K. Sun, L. Zhang, Y. Xing and J. M. Guerrero, "A Distributed Control Strategy Based on DC Bus Signaling for Modular Photovoltaic Generation Systems With Battery Energy Storage," IEEE Transactions on Power Electronics, vol. 26, pp. 3032-3045, 2011.

[18] L. Xu and D. Chen, "Control and Operation of a DC Microgrid With Variable Generation and Energy Storage," IEEE Transactions on Power Delivery, vol. 26, pp. 2513-2522, 2011.

[19] H. Kakigano, Y. Miura, T. Ise and R. Uchida, "DC micro-grid for super high quality distribution—System configuration and control of distributed generations and energy storage devices—," in Power Electronics Specialists Conference, 2006. PESC'06. 37th IEEE, pp. 1-7, 2006.

[20] A. Kwasinski, "Quantitative Evaluation of DC Microgrids Availability: Effects of System Architecture and Converter Topology Design Choices," IEEE Transactions on Power Electronics, vol. 26, pp. 835-851, 2011.

[21] C. Liu, K. T. Chau, Chenxi Diao, J. Zhong, X. Zhang, Shuang Gao and Diyun Wu, "A new DC micro-grid system using renewable energy and electric vehicles for smart energy delivery," in 2010 IEEE Vehicle Power and Propulsion Conference, pp. 1-6, 2010.

[22] J. Lago and M. L. Heldwein, "Operation and Control-Oriented Modeling of a Power Converter for Current Balancing and Stability Improvement of DC Active Distribution Networks," IEEE Transactions on Power Electronics, vol. 26, pp. 877-885, 2011.

[23] J. M. Guerrero, J. C. Vasquez, J. Matas, L. G. de Vicuna and M. Castilla, "Hierarchical Control of Droop-Controlled AC and DC Microgrids—A General Approach Toward Standardization," IEEE Transactions on Industrial Electronics, vol. 58, pp. 158-172, 2011.

[24] R. Noroozian, M. Abedi, G.B. Gharehpetian and S.H. Hosseini, "Combined operation of DC isolated distribution and PV systems for supplying unbalanced AC loads," Renewable Energy, vol. 34, pp. 899-908, 3. 2009.

[25] J.J. Justo, F. Mwasilu, J. Lee and J. Jung, "AC-microgrids versus DC-microgrids with distributed energy resources: A review," Renewable and Sustainable Energy Reviews, vol. 24, pp. 387-405, 8. 2013.

[26] H. Kakigano, A. Nishino, T. Ise, "Distribution voltage control for DC microgrid with fuzzy control and gain-scheduling control," in Power Electronics and ECCE Asia (ICPE & ECCE), 2011 IEEE 8th International Conference on, pp. 256-263, 2011.

[27] S.R. R. Chedid, "Unit sizing and control of hybrid wind-solar power systems," Energy Conversion, IEEE Transactions On, vol. 12, pp. 79-85, 1997.

[28] W. Dalbon, M. Roscia and D. Zaninelli, "Hybrid photovoltaic system control for enhancing sustainable energy," in IEEE Power Engineering Society Summer Meeting, pp. 134-139, 2002.

[29] A. G. Tsikalakis and N. D. Hatziargyriou, "Centralized control for optimizing microgrids operation," in 2011 IEEE Power and Energy Society General Meeting, pp. 1-8, 2011.

[30] S. N. Bhaskara and B. H. Chowdhury, "Microgrids — A review of modeling, control, protection, simulation and future potential," in 2012 IEEE Power and Energy Society General Meeting, pp. 1-7, 2012.

[31] W. Zhang, F. C. Lee and P. Y. Huang, "Energy management system control and experiment for future home," in 2014 IEEE Energy Conversion Congress and Exposition (ECCE), pp. 3317-3324, 2014.

[32] P. Karlsson and J. Svensson, "DC bus voltage control for a distributed power system," IEEE Transactions on Power Electronics, vol. 18, pp. 1405-1412, 2003.

[33] Jung-Won Kim, Hang-Seok Choi and Bo Hyung Cho, "A novel droop method for converter parallel operation," IEEE Transactions on Power Electronics, vol. 17, pp. 25-32, 2002.

[34] K. Kurohane, T. Senjyu, A. Yona, N. Urasaki, E. B. Muhando and T. Funabashi, "A high quality power supply system with DC smart grid," in IEEE PES T&D 2010, pp. 1-6, 2010.

[35] A. Bidram and A. Davoudi, "Hierarchical Structure of Microgrids Control System," IEEE Transactions on Smart Grid, vol. 3, pp. 1963-1976, 2012.

[36] J. Schönberger, R. Duke and S.D. Round, "DC-bus signaling: A distributed control strategy for a hybrid renewable nanogrid," Industrial Electronics, IEEE Transactions On, vol. 53, pp. 1453-1460, 2006.

[37] Xiaofeng Sun, Zhizhen Lian, Baocheng Wang and Xin Li, "A Hybrid renewable DC microgrid voltage control," in Power Electronics and Motion Control Conference, 2009. IPEMC '09. IEEE 6th International, pp. 725-729, 2009.

[38] T. Dragicevic, J. M. Guerrero, J. C. Vasquez and D. Škrlec, "Supervisory Control of an Adaptive-Droop Regulated DC Microgrid With Battery Management Capability," IEEE Transactions on Power Electronics, vol. 29, pp. 695-706, 2014.

[39] A. M. S. S. Andrade, R. C. Beltrame, L. Schuch and M. L. d. S. Martins, "PV module-integrated single-switch DC/DC converter for PV energy harvest with battery charge capability," in 2014 11th IEEE/IAS International Conference on Industry Applications, pp. 1-8, 2014.

[40] Z. Wei, J. Zhao, D. Ji and K.J. Tseng, "A multi-timescale estimator for battery state of charge and capacity dual estimation based on an online identified model," Appl.Energy, vol. 204, pp. 1264-1274, 2017.

[41] Z. Wei, S. Meng, B. Xiong, D. Ji and K.J. Tseng, "Enhanced online model identification and state of charge estimation for lithium-ion battery with a FBCRLS based observer," Appl.Energy, vol. 181, pp. 332-341, 2016.

[42] U. Manandhar, N. R. Tummuru, S. K. Kollimalla, A. Ukil, G. H. Beng and K. Chaudhari, "Validation of Faster Joint Control Strategy for Battery- and Supercapacitor-Based Energy Storage System," IEEE Transactions on Industrial Electronics, vol. 65, pp. 3286-3295, 2018.

[43] S. K. Kollimalla, M. K. Mishra and N. L. Narasamma, "Design and Analysis of Novel Control Strategy for Battery and Supercapacitor Storage System," IEEE Transactions on Sustainable Energy, vol. 5, pp. 1137-1144, 2014.

[44] J. Pegueroles-Queralt, F. D. Bianchi and O. Gomis-Bellmunt, "A Power Smoothing System Based on Supercapacitors for Renewable Distributed Generation," IEEE Transactions on Industrial Electronics, vol. 62, pp. 343-350, 2015.

[45] C. Abbey, W. Li and G. Joos, "An Online Control Algorithm for Application of a Hybrid ESS to a Wind–Diesel System," IEEE Transactions on Industrial Electronics, vol. 57, pp. 3896-3904, 2010.

[46] N. Mendis, K. M. Muttaqi and S. Perera, "Management of Battery-Supercapacitor Hybrid Energy Storage and Synchronous Condenser for Isolated Operation of PMSG Based Variable-Speed Wind Turbine Generating Systems," IEEE Transactions on Smart Grid, vol. 5, pp. 944-953, 2014.

[47] B. Hredzak, V. G. Agelidis and M. Jang, "A Model Predictive Control System for a Hybrid Battery-Ultracapacitor Power Source," IEEE Transactions on Power Electronics, vol. 29, pp. 1469-1479, 2014.

[48] J. Shen and A. Khaligh, "A Supervisory Energy Management Control Strategy in a Battery/Ultracapacitor Hybrid Energy Storage System," IEEE Transactions on Transportation Electrification, vol. 1, pp. 223-231, 2015.

[49] N. R. Tummuru, M. K. Mishra and S. Srinivas, "Dynamic Energy Management of Renewable Grid Integrated Hybrid Energy Storage System," IEEE Transactions on Industrial Electronics, vol. 62, pp. 7728-7737, 2015.

[50] Y. Gu, W. Li and X. He, "Frequency-Coordinating Virtual Impedance for Autonomous Power Management of DC Microgrid," IEEE Transactions on Power Electronics, vol. 30, pp. 2328-2337, 2015.

[51] D. Nilsson and A. Sannino, "Efficiency analysis of low- and medium- voltage DC distribution systems," in Power Engineering Society General Meeting, 2004. IEEE, pp. 2315-2321 Vol.2, 2004.

[52] D. Salomonsson and A. Sannino, "Low-Voltage DC Distribution System for Commercial Power Systems With Sensitive Electronic Loads," IEEE Transactions on Power Delivery, vol. 22, pp. 1620-1627, 2007.

[53] B. Liu, S. Duan and T. Cai, "Photovoltaic DC-Building-Module-Based BIPV System—Concept and Design Considerations," IEEE Transactions on Power Electronics, vol. 26, pp. 1418-1429, 2011.

[54] E. Alliance, "Public Overview of the EMerge Alliance Occupied Space Standard," 2015.

[55] E. Alliance, "Public Overview of the EMerge Alliance Data," Telecom Center Standard Version, vol. 1, pp. 1-10, 2014.

[56] W. Zhang, D. Dong, I. Cvetkovic, F.C. Lee and D. Boroyevich, "Lithium-based energy storage management for DC distributed renewable energy system," in Energy Conversion Congress and Exposition (ECCE), 2011 IEEE, pp. 3270-3277, 2011.

[57] A.S. Morais and L.A. Lopes, "Interlink Converters in DC nanogrids and its effect in power sharing using distributed control," in Power Electronics for Distributed Generation Systems (PEDG), 2016 IEEE 7th International Symposium on, pp. 1-7, 2016.

[58] T. Dragičević, X. Lu, J.C. Vasquez and J.M. Guerrero, "DC microgrids—Part I: A review of control strategies and stabilization techniques," IEEE Transactions on Power Electronics, vol. 31, pp. 4876-4891, 2016.

[59] Z. Shuai, J. Fang, F. Ning and Z.J. Shen, "Hierarchical structure and bus voltage control of DC microgrid," Renewable and Sustainable Energy Reviews, 2017.

[60] S. Kolluri and N. L. Narasamma, "Analysis, modeling, design and implementation of average current mode control for interleaved boost converter," in 2013 IEEE 10th International Conference on Power Electronics and Drive Systems (PEDS), pp. 280-285, 2013.

[61] N. Mutoh and T. Inoue, "A Control Method to Charge Series-Connected Ultraelectric Double-Layer Capacitors Suitable for Photovoltaic Generation Systems Combining MPPT Control Method," IEEE Transactions on Industrial Electronics, vol. 54, pp. 374-383, 2007.

[62] N. Mutoh, M. Ohno and T. Inoue, "A Method for MPPT Control While Searching for Parameters Corresponding to Weather Conditions for PV Generation Systems," IEEE Transactions on Industrial Electronics, vol. 53, pp. 1055-1065, 2006.

[63] W. Jing, C.H. Lai, W.S.H. Wong, M.L.D. Wong, "A comprehensive study of battery-supercapacitor hybrid energy storage system for standalone PV power system in rural electrification," Applied Energy, vol. 224, pp. 340-356, 15 August 2018. 2018.

[64] M. Rodriguez, G. Stahl, L. Corradini, "Smart DC power management system based on software-configurable power modules," IEEE Transactions on Power Electronics, vol. 28, pp. 1571-1586, 2013.

[65] H. Bai, Z. Nie and C.C. Mi, "Experimental comparison of traditional phase-shift, dual-phase-shift, and model-based control of isolated bidirectional DC–DC converters," IEEE Transactions on Power Electronics, vol. 25, pp. 1444-1449, 2010.

[66] S. Inoue and H. Akagi, "A bi-directional isolated DC/DC converter as a core circuit for 3.3-kV/6.6-kV power conversion systems in the next generation," IEEJ Transactions on Industry Applications, vol. 126, pp. 211-217, 2006.

[67] Z. Haihua and A.M. Khambadkone, "Hybrid modulation for dual active bridge bi-directional converter with extended power range for ultracapacitor application," in Industry Applications Society Annual Meeting, 2008. IAS'08. IEEE, pp. 1-8, 2008.

[68] B. Zhao, Q. Song, W. Liu and Y. Sun, "Overview of dual-active-bridge isolated bidirectional DC–DC converter for high-frequency-link power-conversion system," IEEE Transactions on Power Electronics, vol. 29, pp. 4091-4106, 2014.

[69] C. Mi, H. Bai, C. Wang and S. Gargies, "Operation, design and control of dual H-bridge-based isolated bidirectional DC–DC converter," IET Power Electronics, vol. 1, pp. 507-517, 2008.

[70] A.R. Alonso, J. Sebastian, D.G. Lamar, M.M. Hernando and A. Vazquez, "An overall study of a Dual Active Bridge for bidirectional DC/DC conversion," in Energy Conversion Congress and Exposition (ECCE), 2010 IEEE, pp. 1129-1135, 2010.

[71] H.K. Krishnamurthy and R. Ayyanar, "Building block converter module for universal (ac-dc, dc-ac, dc-dc) fully modular power conversion architecture," in Power Electronics Specialists Conference, 2007. PESC 2007. IEEE, pp. 483-489, 2007.